Characterization and Enhancement of Transorbital Endoscopy

By

Michael Paul DeLisi

Dissertation

Submitted to the Faculty of the

Graduate School of Vanderbilt University

in partial fulfillment of the requirements

for the degree of

DOCTOR OF PHILOSOPHY

in

Biomedical Engineering

May, 2014

Nashville, Tennessee

Approved:

Robert L. Galloway, Ph.D.

Michael I. Miga, Ph.D.

Louise A. Mawn, M.D.

Eva M. Harth, Ph.D.

Bennett A. Landman, Ph.D.

ACKNOWLEDGMENTS

I would like to thank my advisor and mentor Dr. Robert Galloway for his continued guidance and support. He has been my role-model in many respects, and has taught me many valuable lessons about being a scientist. My research would not be possible without the efforts of Dr. Louise Mawn, who contributed significantly in both conceptual and practical terms. Thanks also go to my committee members, Dr. Michael Miga, Dr. Eva Harth, and Dr. Bennett Landman, for their guidance and advice.

Throughout my time at Vanderbilt, I have spent a lot of time with the various other graduate students and post-docs under Dr. Galloway and Dr. Miga, particularly Tom Pheiffer, David Kwartowitz, Nkiruka Atuegwu, Rowena Ong, Courtenay Glisson, Ishita Garg, Yifei Wu, Rebekah Conley, Janet Ondrake, and Amber Simpson. In addition to their friendship, they have been precious resources in my academic endeavors. A special thanks goes to the Vanderbilt University Medical Center staff in the CT room and surgical sciences department, namely Dhal Irvine, Amy Nunnally, Jamie Yates, and Phil Williams.

My interest in science and technology started when a close family friend, Bill Patton, gave our family an old 286 computer and taught me the basics of DOS. This passion was nurtured expertly by the various instructors I have had over the years, through grade school, high school, college at the Cooper Union, and graduate school here at Vanderbilt. Any success I have is a result of their efforts, and the constant support and encouragement of my family.

This work was supported in part by the Research to Prevent Blindness Physician Scientist Award, the Unrestricted Grant from Research to Prevent Blindness to the Vanderbilt Eye Institute, and the National Institutes of Health under Grant R21 RR025806.

TABLE OF CONTENTS

Page

LIST OF FIGURES

Figure Page

LIST OF TABLES

Table Page

CHAPTER I

INTRODUCTION

Image-guided surgical solutions have become increasingly prevalent in modern medicine. Utilizing scientific advances in spatial localization, medical image acquisition, image processing and registration, computer displays and visualization, and endoscopy, these minimally-invasive procedures are capable of performing precise surgical tasks in sensitive environments with lower risk to the patient when compared to a traditional open approach. Furthermore, image-guided procedures allow access to certain anatomical regions that would otherwise be impossible or extremely impractical to reach with standard methods. This capability fundamentally changes the paradigm of therapy for a variety of pathological scenarios, with an abundance of unorthodox but theoretically effective treatment plans now realistic possibilities.

One such instance of a challenging anatomical environment is the orbit, also known as the eye socket. The orbital space is bounded on almost all sides by the bones of the skull, with the primary exception being the frontal face in which the globe, or eyeball, is situated. The interior of the orbit behind the globe, known as the retrobulbar space, contains various soft tissue structures, most notably the optic nerve. Attempts at medical intervention in this space are inherently difficult because the globe limits direct access, often necessitating the temporary removal of surrounding bone.

Optic neuropathies are a subset of diseases characterized by damage to the optic nerve, typically resulting in vision loss. The most common optic neuropathy is glaucoma, a degenerative condition characterized but not inherently caused by increased intraocular pressure.

Conventional therapy only focuses on managing intraocular pressure and has necessitated the development of neuroprotective pharmacological agents that are designed to halt the progression of the disease and preserve existing functional neurons. Unfortunately, these drugs have seen limited use due to ineffective delivery systems.

The fundamental purpose of this research is to enable minimally-invasive transorbital therapy, particularly in the form of direct delivery of neuroprotective drugs to the optic nerve, using image-guided surgical techniques. The goals outlined in this document represent the next steps in an ongoing collaborative effort to change the paradigm of treatment for optic neuropathies, and intraorbital therapeutic challenges in general. This effort has previously resulted in the development of an image-guided transorbital endoscopic system, which will be referenced extensively.

Background

Glaucoma is a neurodegenerative condition of the eye, determined by the World Health Organization to be the second cause of visual impairment worldwide [1]. The most common form, primary open angle glaucoma (POAG), is a chronic condition that progressively damages the optic nerve, resulting in irreversible vision loss and eventual blindness. Glaucoma has become increasingly prevalent in developed countries due to aging populations, as the elderly are more susceptible to the disease.

Standard management of glaucoma consists of topical medication to reduce intraocular pressure, which is a common aggravating factor. However, this therapy is limited in its effectiveness since it does not treat the disease at the fundamental neuron level. If the progression of open angle glaucoma is to be stopped, a more direct approach is required.

Neuroprotective drugs are pharmacological agents designed to prevent neural cell death and halt degeneration. Application of these drugs directly to the optic nerve presents a series of challenges due to the highly sensitive anatomy of the region and the low persistence of the medication at the site of application. Furthermore, the relevant orbital biological structures are quite small and any intervention requires exceptionally precise therapeutic tools. It is proposed that an image-guided transorbital endoscopic system be used to deliver time-released neuroprotective agents to the optic nerve for the treatment of open angle glaucoma and any other relevant optic neuropathies. This document will investigate the necessary components of this system, with regards to their design, efficacy, limitations, and implementation for use in transorbital therapy. It will also detail experimental protocols for system validation and performance assessment. However, it is first necessary to be familiar with the relevant anatomy and pathology associated with the optic nerve.

Human Vision

Ocular anatomy

The human orbit is a mostly enclosed, roughly conical space containing the eye and its associated structures. The interior borders of the orbit are well defined by bone, enclosing an average volume of 24 cm^3 in a healthy adult, though with soft tissue volume in excess of 30 cm^3 due to protrusion out of the orbital cavity [2]. There is typically a minimal difference between the left and right orbital volume in the same subject [2]. The eyeball itself, or the globe, is fixed in the center of the orbital space amidst fat tissue with a series of attached muscles to control its movement. The optical nerve provides a transmission channel for light sensations in the retina to

the brain. It is formed at the optic disc as a bundled extension of retinal neurons in the back of the eye, traverses the retrobulbar space in a relatively straight path through surrounding fat tissue, and exits the orbit at its apex via the optic canal. One of the bilaterally paired cranial nerves, the optic nerves from each eye are partially crossed at the optic chiasm and then continue on as the optic tracts into the lateral geniculate nucleus of the thallamus. The general anatomy of the orbit are shown in Figure 1.

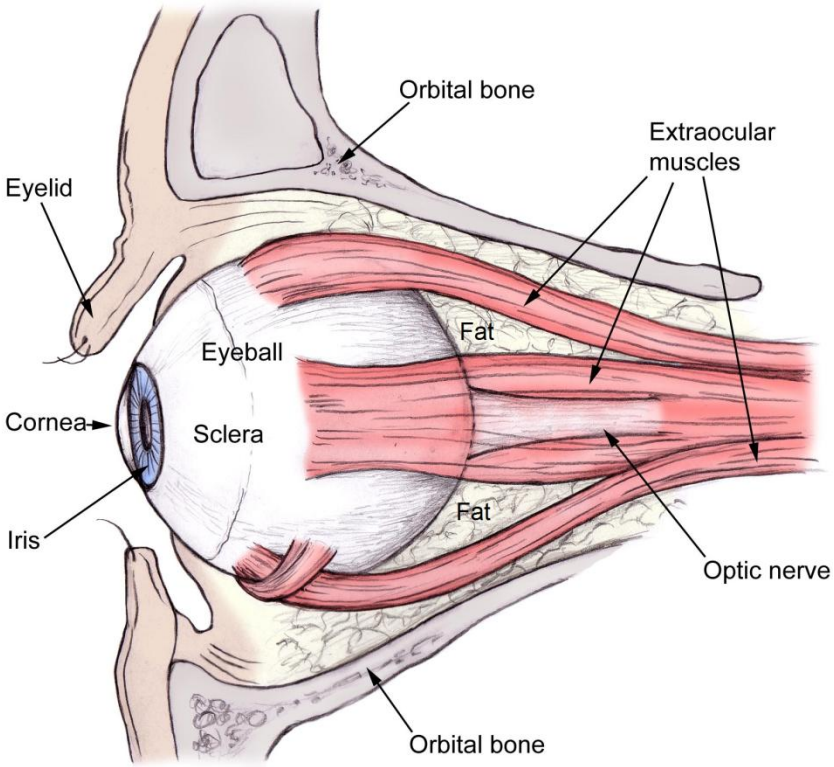

Figure 1. Orbital anatomy
[http://www.emedicinehealth.com/anatomy_of_the_eye]

The optic nerve consists primarily of retinal ganglion cell axons which are myelinated beyond the retina. As an extension of the central nervous system, the entire nerve fiber bundle along with the central retinal artery is sheathed by cerebrospinal fluid and the meninges for protection. The configuration of the optic nerve and its encasement is illustrated in Figure 2. The

meninges is composed of three tissue layers. The dura mater is the outermost layer and densest of the three. The arachnoid mater, characterized by its web-like appearance, is substantially more delicate, while the pia mater is the innermost layer, closely adhering to the neural tissue surface [3]. The subarachnoid space lies between the arachnoid mater and the pia mater and contains the cerebrospinal fluid. The average thickness of the intraorbital segment of the optic nerve in an adult human is 3.5 mm [4].

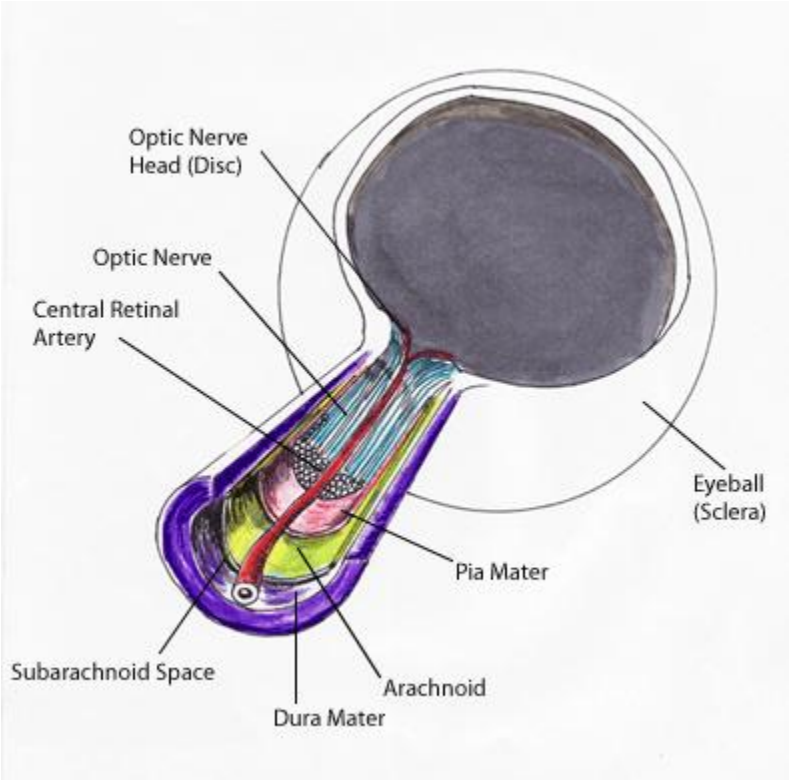

Figure 2. Optic nerve and meninges
[http://www.ihrfoundation.org]

Optic neuropathy

Optic neuropathies are conditions that damage the optic nerve and cause retinal ganglion cell death, resulting in the loss of vision [4]. The onset of vision loss can be rapid or progressive,

depending on the disorder. There are several forms of optic neuropathy, including ischemic, inflammatory, compressive/infiltrative, traumatic, toxic/deficiency, and hereditary [5].

- Ischemic optic neuropathy results from inadequate blood flow to the optic nerve, with the onset of vision loss typically occurring rapidly.
- Optic neuritis is the inflammation of the optic nerve usually characterized by swelling and the degradation of the myelin sheath. Individuals with demyelination disorders are at particularly high risk of developing optic neuritis, with an evidence rate of up to 70% in multiple sclerosis cases [6].
- Compressive optic neuropathies are caused by the compression of the optic nerve due to some harmful process within the orbit, while infiltrative optic neuropathies occur when a harmful process actually permeates into the optic nerve and causes damage. These processes can be metastatic cancerous tumors, bacterial or viral infections, or inflammatory disorders such as sarcoidosis.
- Traumatic optic neuropathy refers to optic nerve damage as a result of an injury, such as direct invasive contact with a foreign object or indirect force absorption due to a blunt impact. Poor nutrition, namely severe vitamin B12 deficiency, and exposure to various toxins, such as methanol ingestion, can also result in optic neuropathy.
- Additionally, there are several hereditary conditions of the optic nerve that cause vision loss, such as Leber's hereditary optic neuropathy.

Glaucoma

Glaucoma has traditionally be defined as a disease of elevated intraocular pressure, with the increased pressure eventually damaging retinal nerve fibers at the optic disk [6]. It the

leading cause of blindness in developed nations, and the second leading cause worldwide, trailing cataracts [1]. There are approximately 60 million people worldwide suffering from glaucoma in 2010 and an expected 80 million in 2020 [7].

Primary glaucoma, where there are no other ocular disorders at work, is subdivided into three groups: open-angle, angle-closure, and congenital. In angle-closure glaucoma, the aqueous humor cannot drain out of the eye due to a blockage of the trabecular meshwork by the iris, and immediate surgical intervention is necessary to create a new fluid pathway. Congenital glaucoma is similar in that there is a developmental inhibition of proper aqueous humor drainage that requires a surgical solution. Open-angle glaucoma is unique in that the iridocorneal angle is unobstructed and the loss of vision may or may not be accompanied by elevated intraocular pressure [8]. Open-angle glaucoma is the most prevalent form of the condition, accounting for an estimated 74% of glaucoma cases worldwide and 89% of cases in developed nations [7].

The standard treatment for primary open-angle glaucoma is the regular administration of topical medications to reduce intraocular pressure, which has been demonstrated to slow the progression of the disease [9]. Unfortunately, there are significant issues with patient compliance to the necessary daily topical treatment regimes, with high rates of skipped applications and eventual total discontinuation [10, 11]. Perhaps of more physiological relevance, these medications have extremely poor penetrative ability and persistence, with less than a 5% estimated permeation of the cornea due to lacrimal drainage and thus minimal impact on the relevant intraocular tissues and the posterior of the eye in general [12, 13]. More localized drug therapy with intravitreal implants or injections results in a substantially higher rate of drug delivery to posterior of the eye, but these procedures carry a variety of high risks such as vitreous hemorrhage, retinal detachment, or endophthalmitis infection [13, 14, 15]. Along with their

obvious discomfort to the patient, regular intravitreal injections are also known to raise intraocular pressure for a period of time, which is counterproductive to the medication [15].

The inadequacy of standard intraocular pressure reduction treatments to completely halt primary open-angle glaucoma progression along with the fact that elevated pressure is not present in all cases has led to many to reconsider the mechanism of the disease [16]. Recent consensus is that the fundamental cause of primary open-angle glaucoma is retinal ganglion cell apoptosis, with increased intraocular pressure as an aggravating but not intrinsic component [16, 17, 18, 19, 20]. Apoptosis is thought to be precipitated by a variety of factors such glial cell activation and compromised neighboring tissues [17], changes in blood flood and endothelial dysfunction [18], and neurotrophin deprivation [19], though the exact underlying mechanism is not thoroughly understood [19, 20, 21]. Furthermore, the myelinated retinal ganglion cell axons of the retrobulbar optic nerve are now also being considering as a primary site of injury, as opposed to just the cell bodies and unmyelinated axons at the optic disk [4, 16].

Neuroprotection

The paradigm shift concerning the underlying mechanism of primary open-angle glaucoma has necessitated a different approach to treatment, beyond the traditional concern with simply reducing intraocular pressure and towards the prevention of retinal ganglion cell apoptosis [16, 21, 22, 23, 24, 25, 26]. Levin defines neuroprotection of the optic nerve as "a therapeutic strategy directed at keeping retinal ganglion cells alive and functional" [23]. While neuroprotection for optic neuropathy has been suggested for over a decade [22] and has proven to work in various animal models, there has been substantial difficulty in developing pharmacological agents with a significant rate of success in humans [24]. Levin and Peeples

attribute this to poor animal models of the human disease, disease variability, developmental differences, varying degrees of axonal and neuronal damage, and lack of drug efficacy [24]. Studies are still underway to optimize neuroprotective effects in the optic nerve [25, 26].

Neuroprotective agents

Among the most promising neuroprotective agents are memantine and brimonidine. Memantine is an NMDA receptor antagonist approved for human use in Alzheimer's patients [24], but phase III clinical trials did not demonstrate substantial efficacy in glaucoma [27]. Brimonidine tartrate is an alpha2-adrenergic agonist that has demonstrated substantial neuroprotective effects in animals [28, 29], but statistically insignificant effects in human trials for non-arteritic ischemic optic neuropathy [30, 31] and Leber's hereditary optic neuropathy [32]. However, a recent trial by the Low-Pressure Glaucoma Study group reported substantially less visual loss in glaucoma patients who were administered brimonidine as opposed those given timolol, a standard glaucoma topical drug that reduces aqueous humor production, despite very similar levels of intraocular pressure for all patients throughout the study [33]. The superior vision preservation of brimonidine regardless of intraocular pressure levels indicates a neuroprotective process at work.

It should be noted that all of these cited studies regarding human clinical trials of potential neuroprotective agents have utilized a topical drop delivery system, and thus poor interaction with the posterior segment due to lacrimal drainage can be expected. Furthermore, the therapy is essentially limited to treatment of the optic disk, with little if any perfusion past the retinal ganglion cell bodies into the axons, which may be a primary site of injury. If neuroprotective agents like brimonidine are to be utilized to their full intended effect, it must be

possible to deliver them in a more direct, transmeningeal fashion to both the optic disk and the axons of the optic nerve.

Nanoparticle encapsulation

As with current intraocular pressure reduction medications, neuroprotective therapy is not a curative process, and therefore must be performed at regular intervals indefinitely to ensure that there is no further cell death. Since direct drug application to the retrobulbar space requires some form of invasive procedure, it is desirable to minimize the frequency of interventions. Fewer treatments would require larger doses, though excessively high amounts would result in steep concentration gradients between the retrobulbar space and the vasculature. Maximal persistence in live tissue would ideally sustain a lower concentration gradient over a longer period of time, ensuring effectively superior doping of neural tissue. Additionally, it is desirable to avoid particularly high concentration drug injections as there are potentially toxic repercussions [34, 35]. These concerns can be accommodated by the encapsulation of a neuroprotective agent such as brimonidine in a time-released format such as the nanoparticle developed by van der Ende *et al.* [36]. These discrete, functionalized particles can be injected in close proximity to the optic nerve and release their neuroprotective payloads at a known rate, resulting in a substantially longer period of dosage. The remaining polyester shell is neutral to the surrounding tissue. Passage of nanoparticle-encapsulated brimonidine through harvested pig and human meninges tissue has been confirmed by Grove *et al*. [37].

Despite prolonging the persistence of neuroprotective agents once administered, the therapy must still be repeated. Regular access to the retrobulbar space cannot be accomplished with a standard surgical intervention due to the tight spatial constraints of the orbit, the risk of

damaging the nerve and surrounding delicate ocular structures, and the speed of recovery. A minimally-invasive approach is required in order for transmeningeal drug delivery to become a practical reality.

Minimally Invasive Procedures

Incentives

A minimally invasive procedure is a medical solution designed to address an internal medical condition, but performed by disturbing the patient's body as little as possible, without compromising the original treatment objective. In the case of a surgical intervention, this often translates to using a few small incisions to insert tools and diagnostic equipment. It provides an alternative to the traditional approach of open surgery, where there is substantial excavation of the region of interest in order to provide the necessary visual and spatial access to the surgeon. Minimally invasive surgeries maintain a superior sterile environment since there is much less exposure of the internal organs to the outside environment, thus significantly reducing the chance of infection. Furthermore, these procedures involve far less bleeding and tissue trauma, minimizing intra-operative complications, post-operative pain, recovery time, and external scarring.

The orbit presents a unique surgical environment, as it is relatively small and contains many delicate structures. Any surgical intervention into the orbit with the aim of preserving vision must be essentially a very low trauma procedure since the globe, extraocular muscles, and optic nerve must remain intact and functional. Therefore the definition of minimally invasive surgery for transorbital applications is more narrow. There are several techniques to access the

retrobulbar space, typically varying based on entry point and surgical plane; however, most still follow the traditional surgical model of cutting a large opening incision, exposing a broad spatial window with retractors, and performing the intervention by hand [38]. Furthermore, few of these techniques allow adequately safe access to the intraconal space, the conical subset of the retrobulbar space containing the optic nerve and roughly bordered by the extraocular muscles [39, 40]. In order to establish a practical, repeatable therapeutic drug delivery regime, the entry point must be even smaller to allow for faster recovery, and the relevant tools must be intelligently guided and more versatile.

Visualization forms

There are several distinct challenges to the minimally invasive approach. The most significant is that the surgeon often does not have direct visual access to the region of interest. As such, alternative means of visualization are necessary components of minimally invasive systems. Endoscopes are instruments that can be inserted into the body through a small entry point in order to provide visual access to a target area when direct line of sight is occluded or insufficient. Endoscopes come in many different forms, such as rigid or flexible, and are often designed for a specific anatomical application. Modern endoscopes are typically equipped with a real-time video system composed of a series of lenses at the tip and ending with a camera at the base. They also often feature a general access working channel for the insertion of various medical devices.

Volumetric medical imaging techniques such as computed tomography (CT) and magnetic resonance imaging (MRI) are known for their widespread use in pathological diagnosis and pre-operative planning, but they are of equal importance in the minimally invasive context

by providing a visual reference for guidance of surgical tools. These tools can be spatially tracked in real time using a variety of systems, giving their positions and orientations within the operating room. By collecting the spatial data points of fixed landmarks on the patient, marking their equivalents on a pre-operative image volume, and applying the principles of image registration, it is possible to unify the three-dimensional coordinate systems of the operating room and the image volume. With an appropriate graphical user interface, the surgeon can indirectly visualize the movement of the tracked tools in relation to the surrounding tissue during a procedure. The use of pre-operative medical imaging techniques for surgical navigation is also categorized as image-guided surgery.

Both endoscopy and registration-enabled image guidance have key applications for transorbital interventions. Neuroprotective drug delivery should occur in close proximity to the optic nerve, so the instrument of deposition must navigate from an external orbital entry point into the orbital fat of the retrobulbar space, past the extraocular muscles to the intraconal space, and up against the optic nerve without touching it. It is desirable for this instrument to stay within the confines of the orbital fat since it is easily penetrable and not vascularized. A thin flexible endoscope is an ideal tool for this task since it allows for visual access to the anatomy behind the eye along with a working channel for drug delivery. Image guidance of a tracked scope provides the necessary spatial orientation for precision navigation, as ocular structures such as the globe, muscles, fat, and nerve are all very distinguishable on pre-operative image volumes.

Image Guidance

The advent of non-invasive three-dimensional medical imaging marked a revolutionary change in the approach to surgical procedures. Previously, the surgeon's spatial awareness was limited to two-dimensional x-ray projections and atlas-based estimations of anatomical structure positions [41]. Volumetric imaging offered the ability to know the location of a pathological condition with a vastly superior degree of accuracy. Image guidance and surgical navigation is achieved by acquiring a suitable image volume, characterizing the working space of the operative room, mathematically unifying the two coordinate systems through the process of registration, and then displaying the result. This process is represented by the diagram in Figure 3. These components are discussed in the following sections.

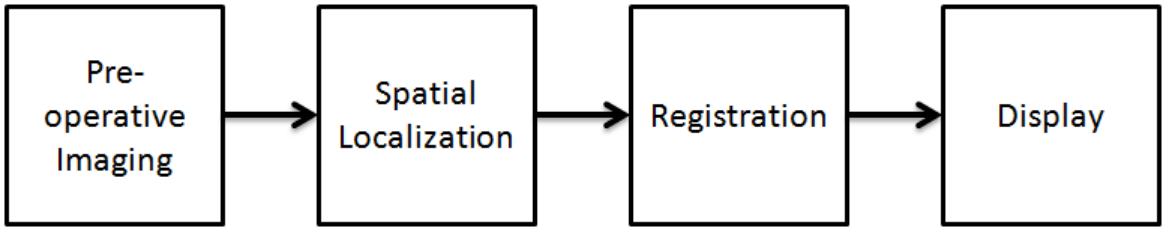

Figure 3. Image guidance components.

Imaging modalities

The two main forms of three-dimensional medical imaging are computed tomography and magnetic resonance imaging. Computed tomography involves the detection and digital reconstruction of x-ray beams passing through the target region from multiple angles, with the degree of tissue attenuation determining image contrast. Magnetic resonance imaging utilizes powerful magnetic fields to align the nuclei of atoms within the body and radio frequency pulses

to disturb them, with the resulting realignment being detectable and dependent on the nature of the tissue.

Each modality has its strength and weakness for using in surgical guidance. Modern CT scanners are very fast, can provide extremely high spatial resolution, though each scan doses the patient with some degree of harmful radiation. In the context of the human orbit, CT images clearly show the bone boundaries and identify fat tissue, but they cannot distinguish between muscle and nerve since their x-ray attenuation factor is essentially the same. MRI provides superior soft tissue contrast and is harmless to the patient, while also being much more expensive. At the moment, CT is the modality of choice for most orbital surgical procedures due to its low cost and high spatial resolution, though it is feasible to anticipate that regular transorbital drug therapy will result in an unacceptable net radiation dose to the patient if a CT scan is administered at each session. Radiation dosage can be minimized by taking fewer CT slices or referencing a previous volume and assuming a negligible degree of internal shift of the globe, extraocular muscles, and optic nerve between sessions. MRI may be the long-term preferred option if monetary expense is not an issue.

Spatial localization

Real-time spatial localization information can be obtained in a variety of ways. Early neurosurgical systems and current surgical robots use geometric localizers such as articulated arms to characterize three-dimensional space [41], but these methods are too awkward and rigid to be of use in the orbit. There are several triangulation-based optical tracking systems capable of localizing rigid objects affixed with active LEDs or passive retroreflective spheres in a known

pattern. The Northern Digital Optotrak and Polaris models are examples of optical tracking systems. The Polaris system is shown in Figure 4.

Figure 4. Northern Digital Polaris Spectra (far left) and Vicra (mid left) detectors, Polaris active emitter (mid right) and passive reflective sphere (far right) probes [http://www.ndigital.com/medical/polarisfamily.php]

Optical systems are highly accurate and robust with large working volumes, becoming the standard localization modality in clinical practice [41], but they have two major limitations based on the nature of optical detection. The first is the requirement for the active or passive optical trackers to be in line of sight of the detector. The second is that optical systems can only track rigid configurations of emitters or reflective spheres. Therefore it is not possible to localize the tip of a non-rigid flexible endoscope within the orbital space.

Electromagnetic tracking devices operate by observing the motion of small sensors through a static electromagnetic field of a known size. The Northern Digital Aurora system generates three orthogonal dipole magnetic fields that induce voltage through a small coil probe proportional to the flux at that point [41], resulting in position and orientation information. This system is shown in Figure 5. Since directional flux is value being measured, multiple coils configured together in one probe are needed to capture all degrees of orientation. Electromagnetic tracking systems are advantageous because they do not require line of sight

between the field emitter and the tracked coil probe. The probe itself is also small enough to fit down the working channel of a flexible endoscope. Flexible endoscopes also contain little to no metal at their distal ends, so electromagnetic field interference is minimal.

Figure 5. Northern Digital Aurora electromagnetic tracking system [http://www.ndigital.com/medical/aurora.php]

The working volume of electromagnetic tracking systems are much smaller than their optical counterparts due to the high rate of field power loss, but the size is appropriate for localization within the orbital space. Atuegwu and Galloway [42] characterized the working volume of the Aurora system with a 22.6 cm by 22.6 cm rigid square phantom containing an 11 by 11 grid of equally spaced divots, taking measurements throughout a height of 19.2 cm at 5 discrete levels. For multiple positions of the field generator, the spatial locations at the divots were recorded with both a 5 and 6 degree of freedom (DOF) probe and compared to their known coordinates. They observe an average spatial localization error of 0.7 mm for the 6DOF probe and 1.3 mm for the 5DOF probe, with a clear tendency for the error to increase as the distance

between the electromagnetic field generator and the probe increases. The generator also has a "sweet spot," as there is minimal error between 48.0 mm and 86.4 mm from its base. They determine that this degree of accuracy is acceptable for transorbital procedures, particularly if the Aurora field generator is positioned close to the orbit.

Image registration

Registration is the mapping of corresponding coordinates from one space to another that preserves the configuration of features and structures. Rigid registration refers to the scenario where objects in the two spaces are assumed to maintain their shape, position, and orientation relative to each other. The assumption of rigidity is not always valid in the context of surgery since the organs may move in the time between the imaging scan and the procedure, and there are several instances, such as abdominal and brain surgery, where the organs deform and shift due to the changes in pressure associated with puncturing the body [41]. Non-rigid registration techniques and mathematical models can somewhat account for these cases, though they add a significant degree of computation. Fortunately the orbital anatomy is relatively enclosed and compact, so it is expected that rigid registration will suffice.

In point-based registration, corresponding points between image space and patient space are referred to as fiducial points. The coordinates of fiducial points are usually recorded with a probe in patient space by the localization system and manually denoted in the medical image volume. Recognizable anatomical landmarks can be used as intrinsic fiducials for correspondence, but these structures are variably defined regions and not true points [43]. Extrinsic fiducial markers are objects attached to the patient that are clearly visible in both spaces. There are two main types of extrinsic fiducials used in head surgeries. Bone markers are

implanted by drilling a small hole in the outer layer of the skull and screwing in a stem. Containers of image contrast are attached to the stem during imaging while a dimpled cap matched to the tracked probe tip size is attached for localization, allowing for the coordinates of the point in both spaces to be known [44]. Skin markers are typically dimpled disks containing contrast material with an adhesive end and can be stuck onto the patient [45]. Unfortunately, the flesh of a patient's face is not immobile, so the localization error of skin markers is noticeably greater than that of bone markers. However, skin markers are non-invasive and thus more suitable to repetitious therapeutic procedures.

In three dimensional space, the mathematical process of point-based rigid registration is essentially the rotation and translation that optimally aligns two images. This optimization is the minimization of the root mean squared distance between corresponding fiducial points in both spaces, or the fiducial registration error (FRE):

$$\mathrm{FRE}^2 = \frac{1}{N}\sum_{i=1}^{N} |\mathrm{Rx_i} + \mathrm{t} - \mathrm{y_i}|^2$$

where $\mathbf{x}_i$ and $\mathbf{y}_i$ are the two corresponding sets of N points, **R** is the 3D rotation, and **t** is the 3D translation [46]. Fitzpatrick *et al*. goes on to demonstrate that the registration accuracy, or target registration error (TRE), is not necessarily minimized in the presence of a low FRE, but rather by using a high number of fiducial points that are well localized.

Following registration between image and patient space, the locations of tracked objects such as surgical tools can be overlaid on the image volume for guidance purposes. A typical navigation system will display the coronal, sagittal, and transverse slices of the image volume that intersect a tracked tool of interest. Image guided surgery in this form has become the

standard of care in intracranial neurosurgery and otolargyngological surgery due to the particular need for precise visualization within the skull, while spinal, orthopedic, and abdominal applications are also well developed [47]. However, relying purely on registered pre-operative image volumes for guidance can be limiting, especially if the instrument entry path is contorted and updated anatomical information is desired. Image guided endoscopy offers an additional visualization field.

Endoscopy

Conventional endoscopic devices are usually inserted into the body to provide a real-time video stream of the target structures that could only be visually accessible with traumatic open surgery. Unlike reference image volumes, the endoscopic video stream will convey the present state of the region of interest as opposed to how it appeared pre-operatively without perturbation. Endoscopic surgery presents a series of distinct problems to be overcome and limitations that must be remembered.

Challenges

Since an endoscope is typically inserted through a very narrow orifice, there is minimal light penetration and thus the output video feed will be dark. For this reason, most endoscopes are equipped with a light source channel. An unfortunate side effect of using high powered light sources is that there is often direct reflection of light off of the smooth wet surfaces of the internal organs and back into the camera, distorting color and texture information that may be necessary for tissue identification purposes. This issue of glare in turn be addressed with various

intensity based image processing techniques such as those described by Abel *et al.* [48], which work in real time and provide statistically significant improvements over the unaltered video frames.

The tightly compressed nature of the internal organs of the human body also serves to obscure the video output of an endoscope. Upon insertion, the tip of the endoscope is often immediately pressed up against tissue, often resulting in an indistinguishable blur of color. If the procedure requires navigation through a tissue medium, namely orbital fat, the visual impediment would remain the case throughout. This matter can somewhat resolved through the practice of insufflation through the working channel of the endoscope, where inert gases or fluids are pumped into site in order to expand the workspace and allow for improved spatial awareness. The most common gas used for insufflation is carbon dioxide. However, insufflation is not without its own drawbacks. The pumping of gas into a body cavity must be regulated such that the internal pressure increase is not harmful to the surrounding tissue. Gottlieb *et al.* report the incidence of symptoms associated with increased carbon dioxide absorption, such as supraventricular tachycardia, massive subcutaneous emphysema, hypercarbia, and acidosis [49]. Marshall *et al.* present rises in mean arterial pressure, central venous pressure, and heart rate during peritoneal carbon dioxide insufflation [50]. Yau *et al*. investigate using helium gas as an alternative in pigs, but find that the negative cardiorespiratory effects are only amplified when compared to carbon dioxide [51]. The toxicity implications of prolonged carbon dioxide insufflation in the human orbit are currently not well understood, although Shah *et al*. analyzed arterial blood gases throughout an endoscopic optic nerve sheath fenestration procedure utilizing CO_2 insufflation and noted no statistically significant changes [52].

Additionally, contact with tissue tends to leave residue, such as blood, on the lens of the scope, further distorting if not entirely compromising the visual field. Slow scope insertion with light insufflation down the working channel should prevent lens obfuscation to some degree. Water can be used to clean the lens and suction can be applied to remove the water, but this requires multiple working channels or inserted instruments, which is not practical in the case of transorbital procedures. Fortunately, orbital fat is not particularly adhesive or vascularized, so residual tissue or environmental blood should be manageable.

Finally, video capture is essentially a 2D process, compressing all 3D features in a conical line of sight into one displayed frame. This results in difficulty when trying to quantitatively evaluate depth or 3D structure of surrounding tissue. Stereoscopic cameras can provide a degree of depth perception, but they are often very large and impractical in small environments such as the orbit. The lack of depth perception for transorbital drug delivery may come into play when positioning the scope near the optic nerve.

Implementations and impact

Minimally invasive endoscopy surgery has become the preferred course of action for a wide variety of procedures. The field of urology has perhaps been the most impacted, where it is used in everything from bladder stone removal, tumor resection, and full nephrectomies [53, 54]. Mack [53] also reports a high prominence in cholecystectomies, adhesiolysis procedures, myomectomies, adrenalectomies, and soft tissue biopsies.

Endoscopy visualization is not limited to spectral video as its information medium. Endoscopic ultrasound probes have been used for diagnosis of hepatic and upper gastrointensital tract tumors [55, 56]. The insertion of these probes into the abdominal cavity reduces the

thickness of tissue necessary for the ultrasound to traverse, allowing for superior quality images. The real-time ultrasound stream allowed for therapeutic guidance, such as in the case of ablation of hepatic tumors [57].

Examples of more advances in the field include Kynor *et. al* [58] and Rauth *et. al* [59], who demonstrate the feasibility of using an endoscopic laser range scanner to generate a registered surface characterization in image-guided liver surgery. Vasilyev *et. al* describes a stereoscopic endoscope system in combination with three-dimensional echocardiography for intracardiac beating heart surgery [60].

Flexible endoscopes

Endoscopes are designed with features that are desirable for a particular anatomical application, such as length, thickness, video resolution, size and number of working channels, and rigidity. The base of the endoscope is often distinct and houses the video camera, while the telescopic portion enters the body and contains the lens system and working channels. Flexible and rigid endoscopes are shown in Figure 6. Rigid endoscopes are regularly used in abdominal surgery, while flexible scopes are necessary for procedures with a non-linear entry path, such as interventional and diagnostic colonoscopy and bronchoscopy. As can be expected, smaller sized scopes have lower quality video output and fewer, thinner working channels if any at all. The path from an external orbital entry point and the optic nerve is not necessarily linear. Furthermore, there is not much space between the globe and the orbital ridge, or adjacent extraocular muscles. Navigation to the retrobulbar space requires a slender flexible scope, with a working channel for drug delivery.

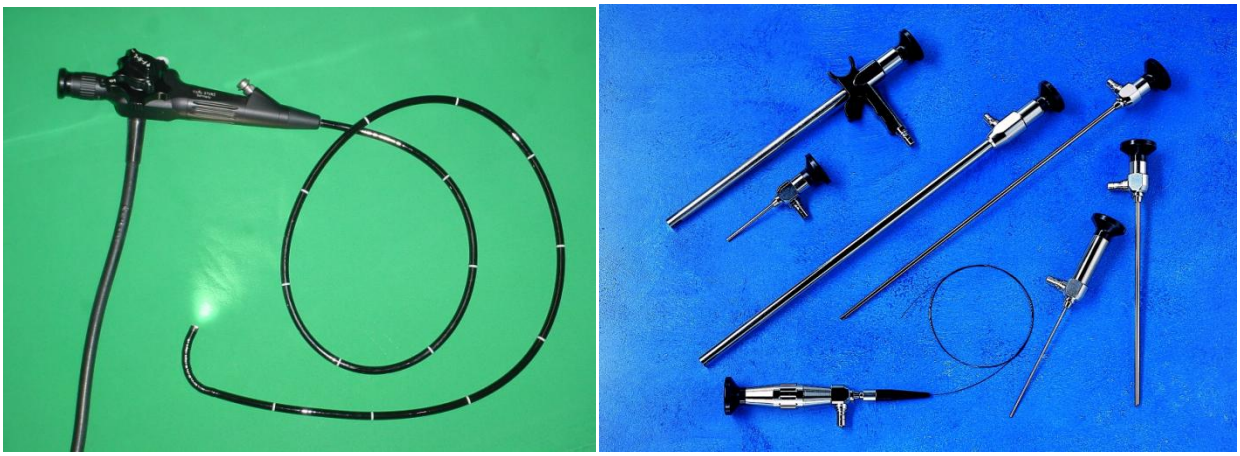

Figure 6. Flexible (left) and rigid (right) endoscopes
[http://en.wikipedia.org/wiki/Endoscope and http://www.medcatalog.com/D_E/endoscop.htm]

Mawn *et al.* explore the feasibility of employing an endoscope for optic nerve sheath fenestration with a free electron laser [61]. An Olympus HYF type P flexible hysterofibroscope was used to navigate to the optic nerve in pig and human cadavers, with a wave guide probe for free electron laser delivery being inserted through the one working channel. The procedure was initially varied across subjects, using both inferior medial and inferior lateral surgical approaches and altering the insufflation medium between saline, hyaluronic acid, and carbon dioxide. They declare no preference for surgical approach, but note that visualization was much superior when using carbon dioxide insufflation despite significant gas leakage from the entry wound. Additionally, they note the difficulty in distinguishing between the optic nerve and the surrounding fat tissue due to the similarity of tissue color, necessitating a careful approach and thorough confirmation prior to fenestration. They also report that while the procedure was initially very tedious and time consuming, the time between endoscope insertion and localization of the optic nerve continually and significantly decreased as the investigator grew more accustomed to using the endoscope. It is determined that endoscopy with a sufficiently thin and

flexible instrument along with an insufflated environment is a valid means of transorbital intervention.

Integrative Transorbital Therapy

Atuegwu *et al.* [62] expand on the idea proposed by Mawn *et al*. [61] by incorporating full image guidance. They use computed tomography scans as the reference image volumes, the Aurora electromagnetic tracking system for localization, and point-based rigid registration with skin fiducial markers. A small electromagnetic sensor with five degrees of freedom is inserted along the length of the working channel of the endoscope such that it is representative of the tip position. The computer visualization is provided by the Operating Room Image-Oriented navigation (ORION) system developed by Stefansic *et al.* [63], which provides four windows for graphical display, a modular design, and a shared information pipeline. This enables an investigator to coordinate tracking information from external localization hardware with custom registration and image processing algorithms. In their particular implementation, Atuegwu *et al.* display the coronal, sagittal, and transverse image planes along with the endoscopic video stream in the four windows, with each image plane intersecting the current registered position of the tracked endoscope tip. This position is updated at a fast rate and clearly marked on the screens at all times to provide the surgeon with spatial awareness of the endoscope position within the orbit.

Atuegwu and Galloway go on to determine that skin fiducial placement around the orbit has an effect on registration accuracy [64]. They calculate the registration error of the target retrobulbar zone for a variety of fiducial positions, modeling skin motion and facial morphology to find the optimal configuration. It is found that the expected target registration error can be

reduced by 50% in an optimal fiducial placement when compared to an unoptimized configuration.

Research and development of an image-guided flexible endoscopic system for transorbital drug delivery is ongoing. This system allows navigation of the endoscope around the globe and through the orbit with the goal of getting within 2-3 mm of the optic nerve for drug delivery. There are several areas of interest that warrant investigation.

Pre-operative planning

Despite the small size of the orbit and relative predictability of the anatomy, interventions with the flexible endoscope take time due to disorientation [61]. Even with the current image guided system described by Atuegwu *et al.* [62], it is necessary to progress very slowly in order to avoid contact with sensitive ocular structures. Orthogonal multiplanar views assist in knowing the current position of the endoscope tip, but are limited in revealing the future path towards the target. Furthermore, endoscopic video can reveal little structural information while the tip is progressing through fat tissue, even with carbon dioxide insufflation.

Pre-operative path planning is accomplished by reviewing the imaging volumes before surgery and marking an interventional path from entry point to target. This information could then be incorporated into the real-time guidance display system and provide the surgeon with a greater sense of directionality. Pre-operative image segmentation can be used to annotate the relevant structures in the orbit and generate three dimensional models. However, both pre-operative planning and image segmentation can take a substantial amount of time if they are done manually by the surgeon. Implementations of these concepts must be extremely user-friendly, semi-, or fully automatic in order for them to be useful. In the case of segmentation, the

relevant organs of the orbit are distinguishable on CT scans; however, both shape and intensity must be taken into account since the extraocular muscles and the optic nerve appear within the same intensity range [65]. Automatic optic nerve segmentation has been demonstrated with high voxel identification accuracy by Noble and Dawant using tubular identification techniques [66], and more recently by Asman *et al*. [67] using a robust Non-Local Simultaneous Truth and Performance Level Estimation (STAPLE) algorithm.

Intra-operative augmented reality

Any pre-operative paths and segmented structure models must be presented to the surgeon in real-time to be of use. The aforementioned segmentation models in combination with a model of the flexible endoscope distal end can be displayed in a unified, windowed three dimensional environment that minimizes the overwhelming visual information of multiplanar views. A pre-operative path displayed as an overlay on existing visual methods would also improve the surgeon's spatial awareness and improve the quality of the procedure. Such supplemental techniques can be categorized as endoscopic augmented reality.

It is of particular interest to overlay the direction of a surgical path or position of surrounding segmented structures within the endoscopic video stream since it provides a unidirectional projection along the current interventional axis and is simpler to reference during guidance [68]. This process would require a registration between the three dimensional space of the pre-operative image volume and the two dimensional projection space of the endoscope. Stefansic *et al.* accomplished this utilizing an optically tracked rigid laparoscope for liver surgery [69]. The mathematical basis of the 2D/3D registration is the direct linear transform, described by Adbel-Aziz and Karada [70]. The same technique can be applied to an electromagnetically

tracked flexible endoscope, but it would require a tracked sensor with six degrees of freedom in order for the endoscope to be mobile [69]. Successful implementation of an augmented reality display could drastically simplify the process of navigating the endoscope tip from the entry incision to the optic nerve.

Procedure impact assessment

Assuming the completed development of an optimized image-guided endoscopic system, it is still necessary to determine the effect that transorbital endoscopic interventions have on the orbital soft tissue structures, specifically the optic nerve. As the aim of direct drug therapy to the nerve is to halt vision loss, it is imperative to minimize causing additional damage during the drug delivery procedure. Any such damage would likely be the result of a traumatic impact between the inserted endoscope and the optic nerve, highlighting the need for the surgeon to constantly maintain awareness of the proximity between the two objects. The development of a method for measuring the forces inflicted upon the optic nerve during transorbital endoscopic procedures would serve as a valuable training tool, while also allowing for assessment of possible injury using biomechanical properties of neural tissue.

Contributions

Research questions

The ultimate goal of this research is to enable image-guided transorbital endoscopic procedures, specifically repeatable drug delivery for the purposes of glaucoma therapy. The conceptual and technical framework for this new technique have been explored by Mawn *et al*. [62] and Atuegwu *et al*. [63], establishing the use of a thin flexible endoscope, a magnetic

tracker inserted down the working channel of the endoscope, and image-guidance visualization in the ORION software platform. Atuegwu *et al*. extensively investigates the characteristics of the magnetic tracking system and establishes that the accuracy is sufficient for transorbital applications [43, 65]. While past work has confirmed that image-guided transorbital endoscopy is technically feasible, a series of issues must be addressed before it can be demonstrated that the system is suitable for human application.

Living tissue presents a number of conditions that are difficult to anticipate or model. Interventions directed at a target point or region in the orbit may seem simple in theory due to its inherently small volume. However, navigation can be compromised by the obstructive presence of the globe and extraocular muscles, while endoscope vision is impaired due to surrounding orbital fat. It remains to be seen if these challenges can be overcome during a objective, task-oriented procedure, such as transorbital target identification.

While a given intervention may be deemed a success due to the completion of a specific objective, such as correct target identification, this does not necessarily imply that the procedure is acceptable for human application. Procedure quality must be assessed, with efforts made to improve upon it if necessary. Procedure time provides an indication of the quality of system guidance. As the distance between the endoscope insertion point and the target is only a few centimeters, excessively long procedure times are the result of substantial surgeon disorientation and an unclear navigation path from insertion point to the target. These long times increase the probability of surgical complications and make the system unattractive as a repeatable therapeutic option. Therefore, optimization of the system with respect to minimizing procedure time must be investigated, with any enhancements for optimization purposes being robustly analyzed in comparison with the standard system to determine effectiveness.

If transorbital endoscopy is to be utilized for glaucoma therapy, interventions must not impair patient health and lifestyle significantly, particularly by maintaining vision quality. While minimization of procedure time contributes to this goal, it is still unknown what direct effect transorbital endoscopy has on the optic nerve. Before human application can be suggested, it is necessary to characterize the disruptive forces on the optic nerve involved in transorbital endoscopy, assess possible consequences with respect to vision, and investigate possible system enhancements to minimize optic nerve contact.

Continuing with the notion of patient safety, ideal surgical technique when implementing transorbital endoscopy has not been explored. Endoscope approach routes to certain regions may be more prone to optic nerve injury than others, as continual insertion results in displaced tissue, increased intraorbital pressure, and possible increased risk of optic nerve contact. The significance of anatomical target location with respect to procedure safety must be determined. Knowledge of this relationship will affect surgical planning if the system is implemented for humans.

Additionally, it is desirable to include additional operators when possible to more completely characterize system performance. This system has been developed primarily under the oversight of one surgeon. While this surgeon's experience is useful in determining system potential, it could potentially bias characterization parameters.

Research accomplishments

This dissertation presents a series of experiments designed to satisfy the aforementioned imperatives. These experiments are discussed extensively in Chapters II-IV of this document.

A series of pig experiments are performed utilizing the system for target localization in the orbit. While all targets were correctly identified, procedures took an average of 24 minutes. These times were deemed to be excessive, signifying a limitation in the guidance system to indicate a clear navigation pathway.

With the aim of minimizing procedure time, the system was enhanced with augmented video, displaying registered 3D target location onto the 2D video stream. All targets were still indentified correctly while average procedure time was significantly reduced to 3 minutes. This experiment demonstrated that task-oriented image guided transorbital endoscopy was possible in live tissue despite the anatomical challenges, while also making an initial effort to improve procedure quality by incorporating video augmentation.

This effort was expanded upon in a series of orbital phantom experiments completed by a total of 16 surgeons from different areas of expertise, with each surgeon performing 8 targeted interventions with alternating use of video augmentation. The results robustly demonstrated that procedure quality, as represented by procedure time, was significantly improved upon by using video augmentation, regardless of surgeon expertise. As such, video augmentation is established as a critical tool in transorbital endoscopy.

With system target localization capabilities and procedure time optimization being demonstrated, it remained to make an assessment of procedure safety by characterizing the physical forces experienced by the optic nerve during an endoscopic intervention. An orbital phantom with the capacity to measure forces along the primary axis of an optic nerve substitute was developed, with target positions set on the nerve at various orbital depths and coronal sides. Endoscopic navigation to each target was performed by an experienced and inexperienced surgeon, with alternating employment of a nerve proximity visualization enhancement.

This experiment revealed that the average applied forces over time were significantly greater for the inexperienced surgeon, confirming the need for system training and establishing parameters for measuring improvement in expertise. It was also demonstrated that anatomical target location with respect to imparted force is significant, with navigations to posterior regions deeper into the orbit resulting in higher average forces. This result directs future implementations of transorbital endoscopy to restrict therapeutic regions to the anterior nerve segment, thus reducing the chance of inadvertant optic nerve trauma. Employment of additional nerve proximity visualization had no effect on measured forces and should not be considered a critical system enhancement.

Maximum observed forces and their associated strains were compared to vision impairment injury thresholds determined from the literature, which were never violated in the experiments. Additionally, the phantom model did not account for the protective effect of orbital fat or the presence of intraorbital optic nerve slack, implying an overestimation of force and strain. As orbital fat and nerve slack are particularly relevant factors in nerve injury, these worst-case scenario results indicate that transorbital endoscopy is reasonably safe.

These contributions have advanced the case for application of image guided transorbital endoscopy to humans. Targeted navigation has been successfully demonstrated in live tissue, procedure quality has been optimized using video augmentation, potentially injury-prone target regions have been isolated, the need for surgeon experience has been confirmed, and a general assessment of procedure safety has been presented under worst case scenario conditions. The only foreseeable remaining obstacle to implementation in human trials is a comprehensive series of animal experiments involving visual function analysis.

CHAPTER II

TRANSORBITAL TARGET LOCALIZATION IN THE PORCINE MODEL WITH ENHANCED ENDOSCOPY

The work described in this chapter is in review as a research article to the International Journal of Computer Assisted Radiology and Surgery (IJCARS).

Abstract

Access to the space behind the eyeball is limited by the position of the globe anteriorly, the neurovascular structures embedded in fat posteriorly, and the tight bony confine of the orbit. These anatomical relationships have impeded application of minimally invasive procedures to the region. We have developed an image-guided system that utilizes a magnetically tracked flexible endoscope to navigate behind the eye to the retrobulbar space. This guided endoscopic approach could allow for minimally invasive foreign body removal, tumor biopsy, or the administration of medical therapy directly to the optic nerve. We demonstrate the capabilities of this system with a series of targeted surgical interventions in the orbits of live pigs. Target objects consisted of microspherical bulbs containing water or gadolinium-based contrast, and were prepared with either the presence or absence of visible coloring agent. Six pigs were placed under general anesthesia and two microspheres of differing color and contrast content were blindly implanted in the fat tissue of each orbit. T1-weighted MRI volumes were obtained and registered and the microsphere containing contrast was designated as the target. After studying the MRI, the surgeon was required to navigate the endoscope to the target and identify it by

color. For three pigs, 3D/2D registration was performed such that the target's image volume coordinates were used to display its location on real-time enhanced endoscope video. The surgeon was able to consistently correctly identify the target by color, with average intervention time of 24.2 minutes without enhancement and 3.2 minutes with enhancement. This difference is statistically significant.

Introduction

Most anatomic sites have benefited from minimally invasive endoscopic approaches. The anatomic constraints of the orbit (eye socket) with the globe anteriorly and the vulnerable neurovascular structures embedded in fat have proven a formidable obstacle to translation of image guided endoscopic surgery to many orbital conditions. One such poorly treated eye disease is glaucoma, the leading cause of irreversible blindness worldwide [7]. Glaucoma is typically characterized by gradual vision deterioration and elevated intraocular pressure. The mainstay of treatment for glaucoma is topical application of medication to reduce intraocular pressure, but vision loss often continues in spite of compliant application. However, recent research has determined that the fundamental mechanism of glaucomatous vision loss is neural degeneration, which current therapies do not address [16]. The need to treat the disease at an axonal level has promoted interest in neuroprotective pharmacological strategies [24]. Several promising neuroprotective agents such as brimonidine have been developed, but there has been limited success in clinical trials that have utilized topical eye drop delivery methods [33].

Levin and Peeples postulate that the performance of neuroprotective therapy has not been fully explored due to consistently poor technique in most trials [24]. Topical eye drops have very limited penetrative ability and persistence as they are subjected to lacrimal drainage, and thus

their potency is severely diluted by the time the drug payload reaches the posterior of the eye and optic nerve [12]. Furthermore, this therapy only targets intraocular pressure, the retina, and optic nerve head, and not the axon.

Direct drug delivery to the optic nerve can be accomplished by inserting an instrument into the orbital cavity, navigating through the orbital fat to a position close to the optic nerve, and depositing an appropriate drug payload. The small working space within the orbit necessitates this procedure to be entirely minimally-invasive, while the delicate nature of the optic nerve requires navigation with a high degree of precision and caution. Balakrishnan et al. report over 100 successful transorbital endoscopic procedures and demonstrate that such procedures are safe, though they emphasize the importance of maintaining awareness of the optic nerve position and avoiding it when possible [71]. However, the vast majority of their cases were for orbital fracture repairs near the borders of the region, removed from the more sensitive orbital anatomy, and involved several instrument insertion ports. These conditions would not be feasible in context of repeatable therapeutic intervention to the retrobulbar space that directly targeted the optic nerve.

Mawn *et al.* utilized a thin, flexible endoscope to reach the retrobulbar space and perform optic nerve fenestration in a porcine animal model with a free electron laser, but noted the tedious nature of the procedure due to difficulty in distinguishing between the optic nerve and the surrounding fat tissue [61]. Atuegwu *et al.* developed an image-guidance system with this endoscope to improve visualization and orientation for the surgeon [62]. This system incorporates magnetic tracking to localize the tip of the endoscope, surface fiducial markers, and point-based rigid registration for orthogonal tomographic display within the Operating Room Image-Oriented Navigation (ORION) software framework [63].

Previous work has validated the performance of the system using a phantom model [72]. This model consisted of a plastic skull with correct sized orbits, within which were globe and optic nerve substitutes. The remaining space was filled with small white cloth stellate balls in order to mimic traversable fat tissue. Furthermore, four differently colored balls were attached within the orbit, one of which was soaked in barium so as to appear distinctive on a CT scan. This ball was considered the target, while the others were distractors. The surgeon was allowed to study the CT images prior to performing the intervention. A group of 28 surgeons with a wide range of endoscopic expertise were required to navigate the flexible endoscope to the target and declare its color. This task was done for each orbit of two skull phantoms, with randomization to either the use of the image-guided system versus only the raw endoscopic video as the first trial, with the second trial using the alternative technique. Reported target identification accuracy was 84.6% using image guidance compared to 78.6% using just the endoscope. While this work demonstrates an improvement using image guidance, *in-vivo* experiments are required to characterize performance under more realistic conditions. Furthermore, due to the sensitive nature of the orbital anatomy, additional development of the system to improve target identification and navigation capability is desirable.

A challenge in endoscopic navigation is maintaining a sense of orientation within the working environment. Sielhorst *et al*. argue for the value of integrating three-dimensional structural information with endoscopic video frames to provide anatomical context due to the constantly changing point of view and horizon of the instrument [68]. This technique is often referred to as augmented reality. A fundamental component of endoscopic video augmentation is performing a registration between 2D video space and 3D image space. Assuming an existing registration between image space and the physical space in which the endoscope is tracked, this

transformation can be calibrated by establishing corresponding sets of points with simultaneously known coordinates in an endoscopic video frame and physical space. Several systems utilizing this concept have been developed, including applications in endoscopic ENT surgery [73], endonasal pituitary surgery [74], and hepatic surgery [69]. More recently, Lapeer *et al.* described a system for endoscopic sinus surgery and assessed calibration, registration, and optical tracking accuracy [75], while Liu *et al.* incorporated video augmentation for image-guided skull base surgery [76]. All of these systems are based on large rigid endoscopes, and most utilize optical tracking.

In this experiment, we measure the targeting accuracy of our flexible endoscope system in live animal models. We also describe the incorporation of a simple real-time endoscopic video enhancement with 3D guidance information and demonstrate its usefulness in a surgical context.

Methods

Equipment

The endoscopic system consisted of a Karl Storz Telecam DX II 20233020 camera system with a Telecam-C 20212134 NTSC single chip camera head and a Karl Storz 11264BBU1 flexible hysteroscope (Karl Storz, Tuttlingen, Germany). Spatial localization was achieved with the Northern Digital Aurora electromagnetic tracking system (Northern Digital Inc., Waterloo, Ontario, Canada). The Aurora planar field generator was mounted on an adjustable articulated arm to facilitate the positioning of the porcine orbit within the ideal working volume described by Atuegwu *et al.* [42]. The hysteroscope contains a 1.3 mm working channel through which an Aurora sensor with 6 degrees of freedom (DOF) was inserted, resting at the tip of the scope with its length secured by a plastic clasp at the entry end. The endoscope

with the inserted sensor can be seen in Figure 7, with the tip shown in Figure 8. The endoscope was also attached to a Karl Storz 615 Xenon light source and a carbon dioxide insufflation pump to augment visualization *in vivo*. Video processing and display was performed by an Intel Core2 Duo machine running Windows 7 and equipped with a Euresys Piccolo frame grabber card. The ORION software system [63] was used to facilitate image guidance.

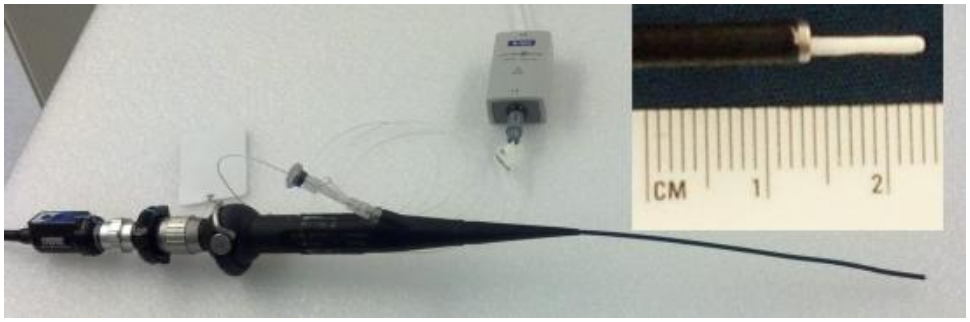

Figure 7. Flexible endoscope with magnetic sensor inserted down the working channel. The box in the upper right corner shows the sensor protruding slightly from the scope.

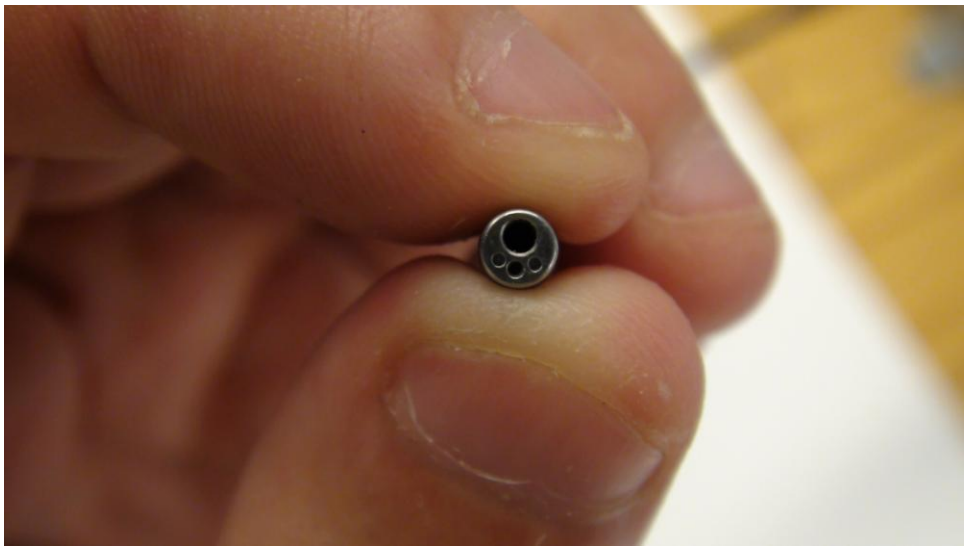

Figure 8. Endoscope tip. The large opening is the working channel, while the smaller ones are the camera (center) and light sources (sides).

NMR microspherical bulbs (Wilmad LabGlass, Kingsport, TN) with a volume of 18 µL and a diameter of approximately 4mm were used as targets. The stems of the bulbs were

substantially clipped, though some length was preserved to facilitate stoppage. Four types of solution were prepared for insertion into the bulbs: pure water, water with red dye, MRI contrast, and MRI contrast with red dye. The MRI contrast solution used consisted of Magnevist diluted 15 times with water. Magnevist is a clear gadolinium-based contrast agent that appears bright on a T1-weighted MRI scan (Bayer Schering Pharma, Berlin, Germany). Bulbs were then filled with solution and divided into differently colored pairs such that one contained Magnevist while the other contained water. For example, bulbs containing pure water were paired with bulbs containing Magnevist and red dye, while bulbs containing water and dye were paired with bulbs containing Magnevist. The result is that each pair would be visually distinctive on both the MRI scan and endoscopic video, but without one color necessitating the presence or absence of MRI contrast. A set of prepared microspheres can be seen in Figure 9.

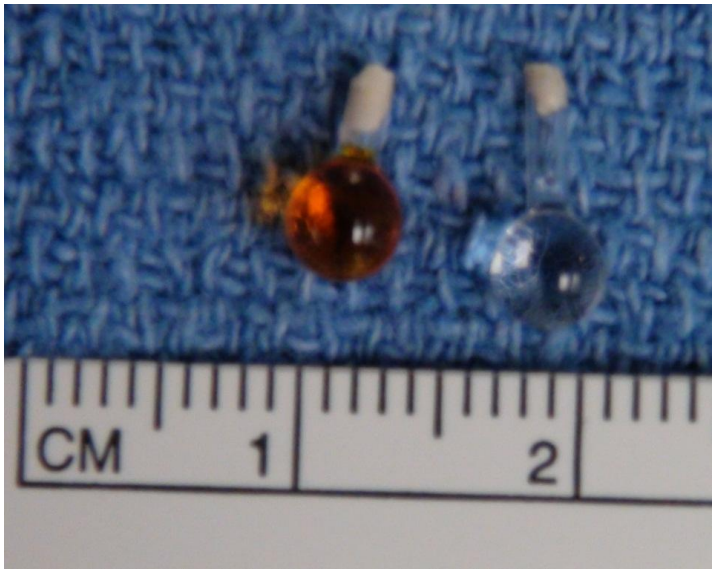

Figure 9. Microspherical bulbs filled with dyed and clear solution.

Experimental procedure

In an Institutional Animal Care and Use Committee (IACUC) approved study, a total of 6 pigs were prepared for surgery and placed under general anesthesia. Each pair of microspheres was assigned to an orbit, and each microsphere was separately inserted into the retrobulbar space. The position and identity, namely the visible color and MR contrast content, of each microsphere was recorded but remained blind to the surgeon. Multimodality radiographic markers (IZI Medical Products, Owings Mills, MD), or surface fiducials, were placed around each orbit. Each pig was then imaged with T1-weighted MRI at 1x1x1 mm voxel resolution centered at the orbits. Subsequent manual image processing consisted of cropped and reforming image volumes for optimal ORION compatibility and annotating the voxel locations of each surface fiducial marker.

Following imaging, each pig was positioned prone on the operating table with the Aurora planar field generator oriented such that the orbit of interest was within the optimal working volume [42]. The surface fiducials surrounding the orbit were localized with an Aurora probe and point-based rigid registration was performed with the corresponding points previously marked on the MR image volume. The ORION screen was divided into quadrants and configured to display the three orthogonal MR image planes containing the position of the tracked endoscope tip as well as the real-time endoscopic video stream. The position of the tracked endoscope tip was noted in each plane with a small colored box.

Prior to intervention, the surgeon inspected the medical image volumes and identified the location of the target microsphere containing Magnevist, which appeared bright in the T1-weighted images. The surgeon was then required to insert the scope into the orbit from a new entry point, navigate to the target microsphere containing Magnevist using the guidance system,

and declare its color as it appeared on the endoscopic video. Following surgery, each pig was euthanized according to IACUC protocol.

Video augmentation

For the last three pigs, the endoscopic video display module within the ORION system was modified to display the location of the target as calculated by a registration from 3D space to 2D space. This registration was accomplished using the Direct Linear Transform (DLT) method [70], a mapping operation that provides the ability to accurately correlate points from the three-dimensional physical space of an operating room to pixels in the two-dimensional image space of the endoscopic video stream. It is desirable to include all points within the conical projection volume in the range of this transformation since structures of interest may be out of direct line of sight of the camera due to the presence of intermediary objects. Using notation similar to Stefansic *et al*. [69], the DLT is represented by the following equation:

$$\begin{bmatrix} w \cdot u \\ w \cdot v \\ w \end{bmatrix} = \begin{bmatrix} a_{11} & a_{12} & a_{13} & a_{14} \\ a_{21} & a_{22} & a_{23} & a_{24} \\ a_{31} & a_{32} & a_{33} & a_{34} \end{bmatrix} \begin{bmatrix} x \\ y \\ z \\ 1 \end{bmatrix} \quad (1)$$

where (x, y, z) is the three-dimensional point in physical space, (u, v) is the resulting point in two-dimensional space, w is a scaling factor, and A is the homogeneous transformation matrix (HTM). The equation uses homogeneous coordinates since it deals with projective space calculations, therefore the HTM has 11 independent elements and a_{34} is set equal to 1. The other parameters in the HTM represent the 11 degrees of freedom (DOF) involved in the transformation from 3D space to 2D space, namely three translations, three rotations, source-to-

image distance, the intersection point of the imaging plane and optical axis, and scaling factors in the *u* and *v* directions [69].

An appropriate HTM for a projection from 3D physical space into a particular 2D image space must be calculated using a known set of corresponding points, specifically:

$$(x, y, z)_n \rightarrow (u, v)_n$$

where *n* is the size of the set of points. It should be noted that in this instance the correspondence is only assumed to be one-way. The first step in the calculation process is rewriting the DLT in equation form. Matrix multiplication yields the following expression for the constant *w*:

$$w = a_{31} \cdot x + a_{32} \cdot y + a_{33} \cdot z + 1 \tag{2}$$

Substituting for *w*, *u* and *v* can be expressed as:

$$u = a_{11} \cdot x + a_{12} \cdot y + a_{13} \cdot z + a_{14} - a_{31} \cdot x \cdot u - a_{32} \cdot y \cdot u - a_{33} \cdot z \cdot u \tag{3}$$

$$v = a_{21} \cdot x + a_{22} \cdot y + a_{23} \cdot z + a_{24} - a_{31} \cdot x \cdot v - a_{32} \cdot y \cdot v - a_{33} \cdot z \cdot v \tag{4}$$

The presence of *u* and *v* on both sides of these equations is not an issue since it is assumed that these values are known. Combining (3) and (4) and taking the size of the known calibration point set into account yields (5).

$$\begin{bmatrix} u_1 \\ v_1 \\ u_2 \\ v_2 \\ \vdots \\ u_n \\ v_n \end{bmatrix} = \begin{bmatrix} x_1 & y_1 & z_1 & 1 & 0 & 0 & 0 & 0 & -x_1 \cdot u_1 & -y_1 \cdot u_1 & -z_1 \cdot u_1 \\ 0 & 0 & 0 & 0 & x_1 & y_1 & z_1 & 1 & -x_1 \cdot v_1 & -y_1 \cdot v_1 & -z_1 \cdot v_1 \\ x_2 & y_2 & z_2 & 1 & 0 & 0 & 0 & 0 & -x_2 \cdot u_2 & -y_2 \cdot u_2 & -z_2 \cdot u_2 \\ 0 & 0 & 0 & 0 & x_2 & y_2 & z_2 & 1 & -x_2 \cdot v_2 & -y_2 \cdot v_2 & -z_2 \cdot v_2 \\ \vdots & \vdots & \vdots & \vdots & \vdots & \vdots & \vdots & \vdots & \vdots & \vdots & \vdots \\ x_n & y_n & z_n & 1 & 0 & 0 & 0 & 0 & -x_n \cdot u_n & -y_n \cdot u_n & -z_n \cdot u_n \\ 0 & 0 & 0 & 0 & x_n & y_n & z_n & 1 & -x_n \cdot v_n & -y_n \cdot v_n & -z_n \cdot v_n \end{bmatrix} \begin{bmatrix} a_{11} \\ a_{12} \\ a_{13} \\ a_{14} \\ a_{21} \\ a_{22} \\ a_{23} \\ a_{24} \\ a_{31} \\ a_{32} \\ a_{33} \end{bmatrix} \quad (5)$$

Stefansic *et al*. [69] note that (5) is of the form $a = Qb$, where a is the $2n$ x 1 vector of control points, Q is the $2n$ x 11 matrix, and b is the 11 x 1 vector of HTM parameters. Vector b can be solved by the multiplication of vector a with the pseudo-inverse of matrix Q. This solution requires Q to be overdetermined such that $n \geq 6$. The resulting static HTM, when used in (1), will theoretically transform any 3D spatial coordinate to a 2D image pixel according to the projective relationship described by the control point set, with negligible computational complexity in a real-time implementation.

A homogeneous transformation matrix was calibrated beforehand using 31 distributed points localized in both endoscopic video space and physical space. These points were gathered from the immobile, rigid plastic grid shown in Figure 10. Small notches were drilled into this grid to minimize probe movement during 3D point magnetic localization, with each notch colored black to appear clearly on the endoscopic video. The grid of 13 points was mounted and set at three different depth intervals of approximately 10, 15, and 20 mm away from the endoscope tip. The points were spatially localized with a magnetically tracked probe and recorded with respect to the tracked endoscope tip, such that the tip was considered to be the origin. This was done to facilitate movement of the endoscope or Aurora field generator during a procedure without compromising the 3D/2D registration. A video frame capture was taken at

each calibration depth interval and the points were manually annotated in 2D. At the calibration depth closest to the endoscope, only the central 5 points were used since the entire grid did not appear within the endoscope's viewing angle. The images used for calibration are also shown in Figure 10.

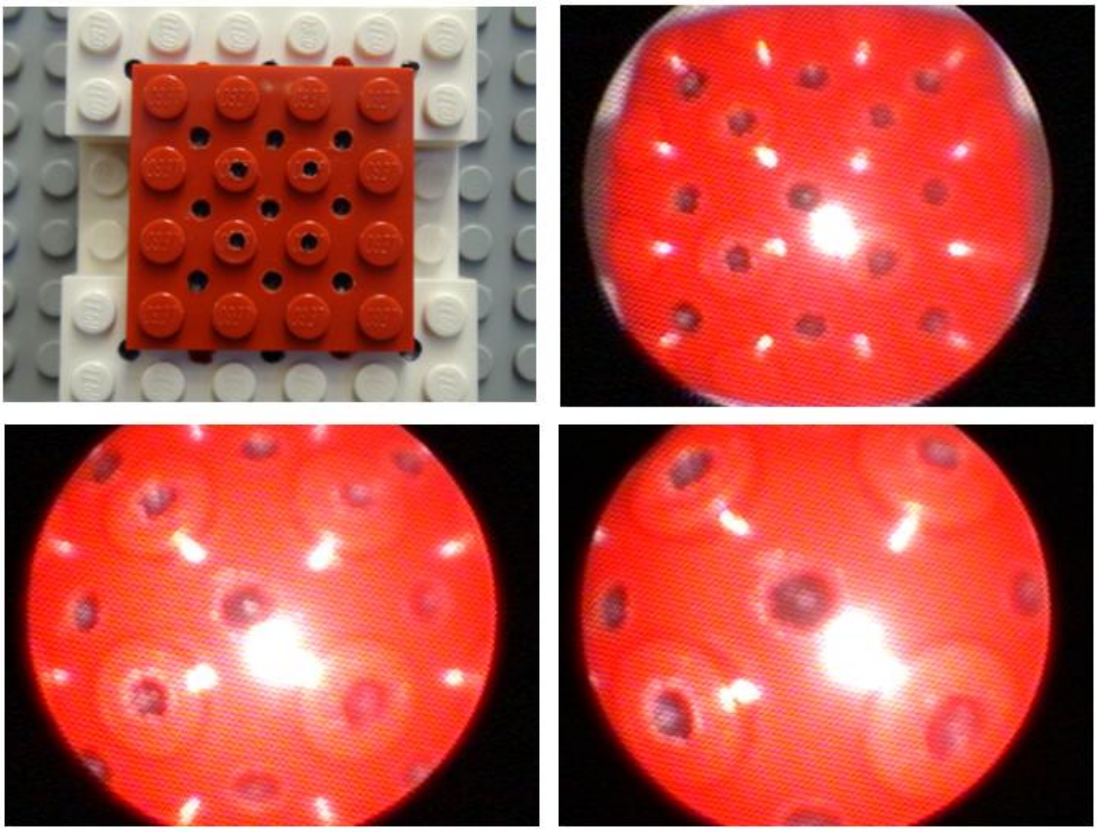

Figure 10. Grids used for flexible endoscope calibration. The black dots are notched calibration points. The red square is approximately 32 mm wide. The upper left image is a picture of the grid, while the remaining images are the endoscopic frame captures used in calibration. The upper right image is at approximately 20 mm away from the endoscopic tip, the bottom left at 15 mm, and the bottom right at 10 mm.

Calibration error was calculated by applying the DLT to all of the 3D calibration points, computing their approximate 2D pixel location, and finding the pixel distance from each point to its corresponding manually annotated 2D calibration point. The unit of distance was then

transformed to millimeters using a measurement of the width of the central black notch to generate a mm/pixel ratio.

It should be noted that optical lens distortion correction, typically modeled as a radial distortion, was not utilized in this particular study as the minor improvement in calibration error did not justify the substantial reduction in video frame rate . Intrinsic camera parameters were calculated using Bouguet's toolbox [77], an implementation of Zhang's method [78], and incorporated into the ORION framework using the OpenCV library's camera calibration functions [79]. However, the difference in the resulting average calibration error was quite small and within the localization error of the Aurora magnetic tracking system, while integration into ORION resulted in a noticeable increase in computational complexity.

The visual element of the video augmentation consisted of two white lines intersecting at the calculated 2D point of a known 3D target point, determined by referencing the pre-operative image volume. Endoscopic video display framerate was not affected by the augmentation.

Results

We regard each of the 12 orbits as a separate interventional procedure, distinguishing between the first 6 which used the standard guidance system, and the last 6 which incorporated the additional video augmentation component. In two cases, one orbit from each of these subgroups, a surface fiducial was lost in the time between imaging and intervention. Dislodged fiducials were a result of placement on unshaved portions of the porcine head as well as deteriorated adhesives on the fiducial base. This resulted in an extremely poor registration and nullified the benefits of the image-guidance system. In these instances the surgeon took excessive time in finding the targets, using only mental knowledge of where they should be

based on referencing the pre-operative image volume. We categorize these data points to be understood outliers and thus only consider the results from 10 interventions, 5 from each subgroup.

For all 10 properly registered orbits, the surgeon correctly identified the color of the target containing diluted Magnevist. For the subgroup of 5 orbits where standard image guidance was used, it took the surgeon 24.2 minutes to find and identify the target. For the subgroup of 5 orbits where augmented guidance was used, this approximate intervention time was reduced to 3.2 minutes. The procedure times were analyzed with the Wilcoxon rank-sum test to compare two independent samples (Mann-Whitney *U* test). It was found that the enhanced endoscope demonstrated significant lower procedure times with $p < 0.02$. A comparison of the procedure times for the two groups can be seen in Figure 11.

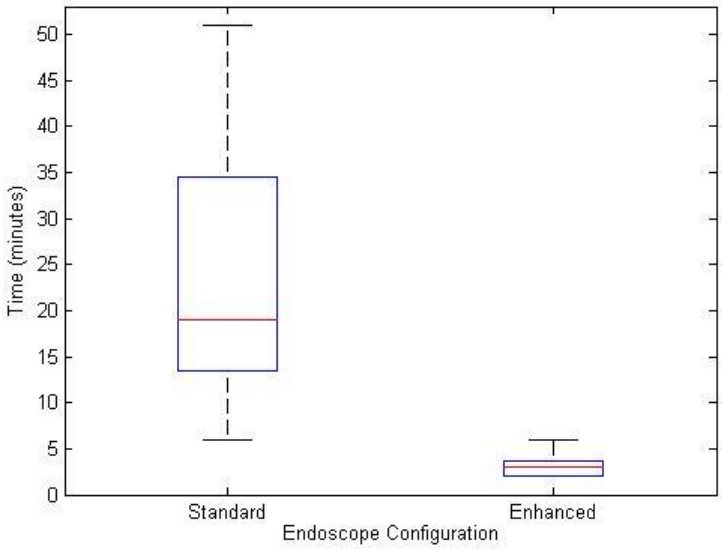

Figure 11. Transorbital procedure times in pigs, with and without enhanced endoscopy

An example of the ORION display screen during the successful identification of a target can be seen in Figure 12. The coronal, sagittal, and axial MRI planes are shown. The colored box represents the registered position of the endoscope tip in image space in real time. The bright spot in the two top images is the target. The white lines on the video image represent the 3D target location registered to 2D video space.

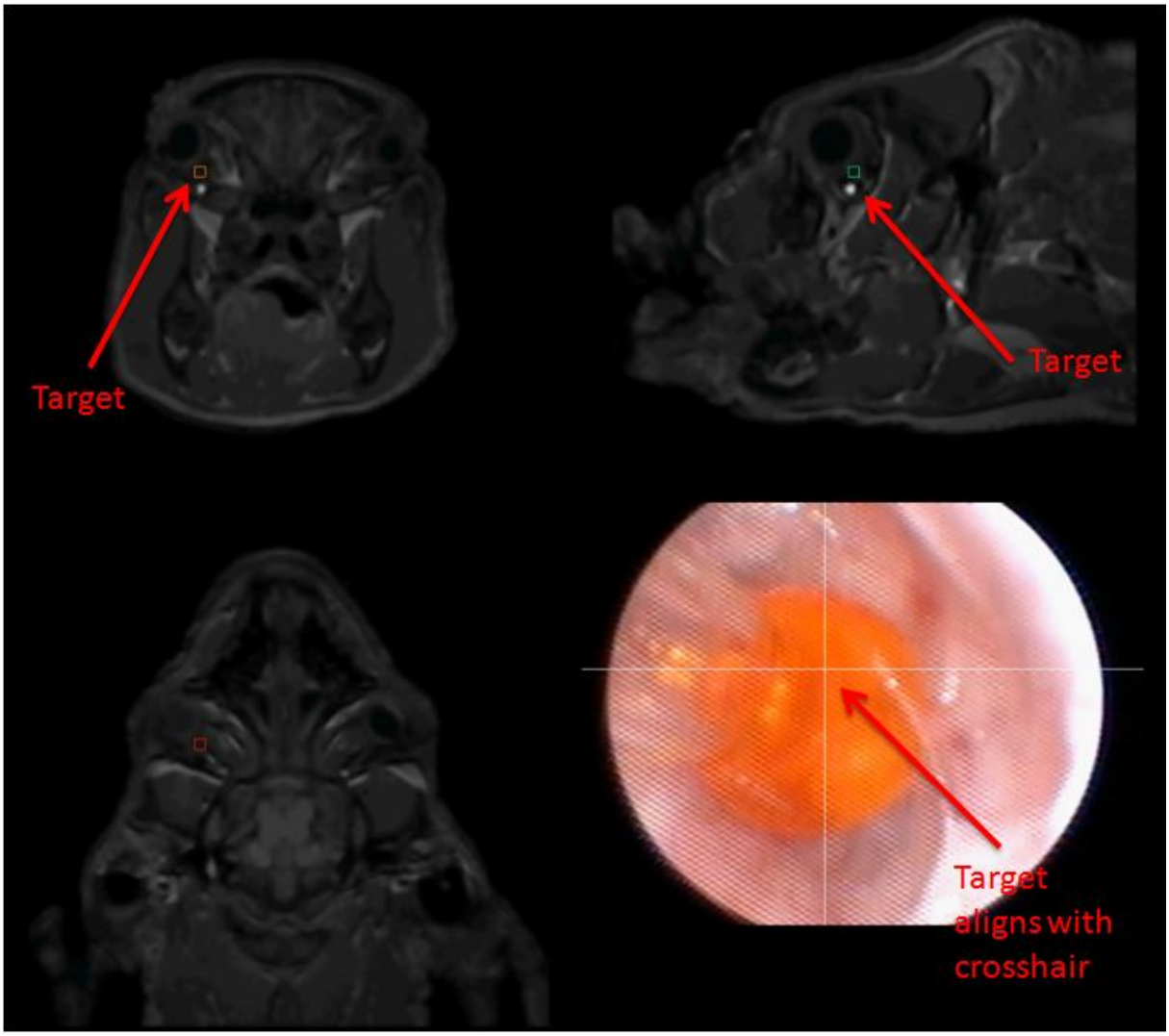

Figure 12. Screenshot of the ORION display during identification of a target with red dye and Magnevist.

The mm/pixel ratios for the calibration images were found to be 0.0260, 0.0356, and 0.0475 mm/pixel for the depths of 10, 15, and 20 mm, respectively. Using these ratios, the

average calibration error for all 31 calibration points was 1.03 mm, with 0.70 mm standard deviation. The errors with respect to the localized distance between 3D calibration points and the tracked endoscope tip are shown in Figure 13, while the errors with respect to the x- and y-coordinates of the 2D calibration points are show in Figure 14.

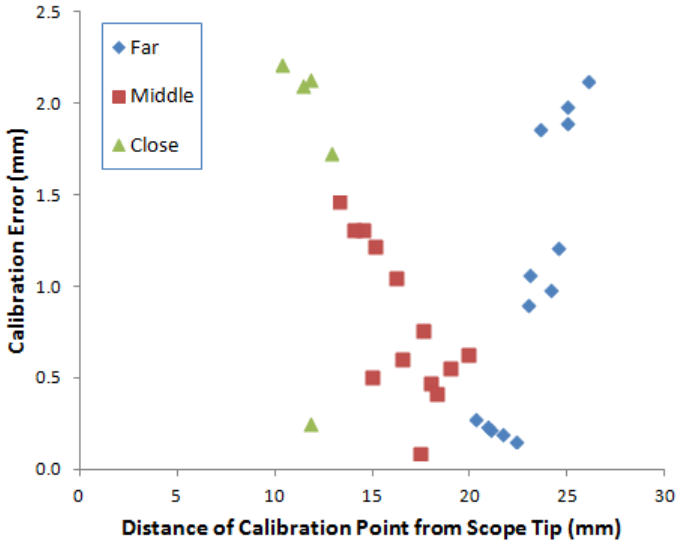

Figure 13. Calibration error (mm) with respect to the distance from 3D calibration points to the tracked endoscope tip (mm).

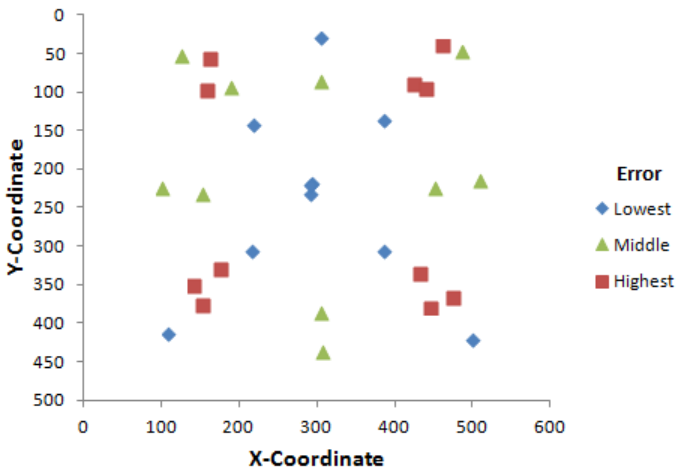

Figure 14. Calibration error distribution with respect to the x- and y-coordinate location of the 2D calibration points. The lowest errors tend to be in the center, with the higher errors farther away.

Discussion

We were able to successfully demonstrate the capability of our system to navigate to a specific region and visually identify the presence of a target with a degree of certainty. The 100% identification accuracy when the fiducials remained in place indicates that our system provides a reliable method of transorbital intervention, in both its standard and augmented forms.

Typical image-guided surgery displays consist of three orthogonal viewing planes intersecting at the point of a tracked instrument. As such, it is easiest to navigate an inserted instrument along a vector within one of these planes since the surgeon is aware of any forward tissue structures. However, an expectation of this scenario for the duration of a procedure is not practical. In these experiments, it was often the case that the targeted microsphere was not visible in any of the orthogonal image displays, requiring the surgeon to use *a priori* knowledge of the target location from inspecting the image volumes pre-operatively to conceptualize a pathway

and navigate the endoscope appropriately. While the surgeon was still able to successfully find and identify the target microsphere, it took considerable time to do so.

There was a statistically significant decrease in procedure time when enhanced endoscopic visualization was used. With the integration of a simple crosshair within the real-time video stream indicating the target location, the surgeon was immediately able to establish a sense of the trajectory and orientation upon insertion of the endoscope into the orbital space. The resulting fast intervention time minimizes trauma to the patient, fatigue of the surgeon, and risk of disorientation within the orbit and disturbing delicate anatomy.

Calibration error was lowest for points at the middle distances of the 3D sampling set, as can be seen in Figure 13. Furthermore, Figure 14 shows that error was low for points in the center of the 2D calibration images, while typically higher for points farther away from the center. However, a robust assessment of the calibration error is limited by a few procedural facts. Calibration point sampling was not uniform, as only 5 points were taken for the closest distance while 13 were taken for the other two, possibly introducing a degree of bias. Furthermore, the use of the same grid orientation at each depth resulted in significant portions of 2D space being undersampled. Finally, optical lens distortion correction was not utilized. Without rectification, inherent lens properties will result in an approximately radial image distortion, also known as a "barrel" distortion. This effect can be visually observed from the calibration images in Figure 10, and the effect on the error with regard to the distance of the calibration point from the center of the lens can be seen in Figure 14. Due to this radial distortion effect, the ratios used to translate error values from pixels to millimeters in a given calibration image are fundamentally invalid, as the number of pixels corresponding to a static physical distance is greater in the center of the image and significantly smaller near the edges. However, it is important to keep in

mind that following initial endoscope insertion using this system, the surgeon generally endeavors to maintain the target within the center of the lens and push the endoscope forward, thus keeping the augmentation within a region of low error. Even if the endoscope is not yet positioned properly, the augmented target location still provides the essential directional orientation information necessary to correct the trajectory, despite the error being in the range demonstrated by Figure 13.

The noteworthy improvement in procedure time when using video augmentation is particularly encouraging in light of these suboptimal calibration conditions. This demonstrates the value of the additional trajectory and orientation information provided to the surgeon.

Conclusions

Image-guided procedures are at least four dimensional with three spatial components and one temporal component. Pre-procedural tomograms such as CT or MR can provide high-contrast, high spatial dynamic range information on the structure of the subject or patient. However, this imaging data cannot reflect peri-procedural changes in the structure and thus there is a temporal mismatch between the data regarding the position of the interventional tools and the structural information. Intra-procedural imaging such as endoscopy can only provide two spatial dimensions of information often confounded by range-based distortions, yet it is perceptibly real-time and reflects the present state of the subject. Since neither data set is wholly adequate to address the challenges presented by transorbital therapy delivery, we have developed this system which uses the advantage of one method to augment the other in order to more closely approximate the therapeutic needs.

The reported series of porcine interventional procedures successfully demonstrated the capabilities of the image-guided endoscopic system to navigate to a targeted location within the orbital space. Incorporation of a video augmentation module to provide a real-time visual indication of 3D target position proved to substantially decrease intervention time, despite suboptimal calibration method. This result has significant ramifications for orbital pathology treatment in general and glaucoma therapy specifically, with repeatable retrobulbar drug delivery becoming a more feasible option.

A robust registration between 3D and 2D space allows for further improvements in endoscopic visualization, such as overlaying segmented orbital structures or pre-operatively planned pathways onto the video for additional orientation and trajectory awareness. Future studies should investigate improving on the calibration routine with optimal point sampling and implementation of optical lens distortion without significantly sacrificing system performance.

Acknowledgments

The authors would like to thank Amy Nunnally, Jamie Yates, and Phil Williams for their assistance with surgery, and Seth Smith with the Vanderbilt University Institute of Imaging Science for providing appropriate MR image sequences.

CHAPTER III

IMAGE GUIDED TRANSORBITAL PROCEDURES WITH ENDOSCOPIC VIDEO AUGMENTATION

The work described in this chapter is in review as a research article to the International Journal of Medical Physics Research and Practice (Med Phys).

Abstract

Surgical interventions to the orbital space behind the eyeball are limited to highly invasive procedures due to the confined nature of the region along with the presence of several intricate soft tissue structures. A minimally invasive approach to orbital surgery would enable several therapeutic options, particularly new treatment protocols for optic neuropathies such as glaucoma. We have developed an image-guided system for the purpose of navigating a thin flexible endoscope to a specified target region behind the eyeball. Navigation within the orbit is particularly challenging despite its small volume, as the presence of fat tissue occludes the endoscopic visual field while the surgeon must constantly be aware of optic nerve position. This research investigates the impact of endoscopic video augmentation to targeted image-guided navigation in a series of anthropomorphic phantom experiments. A group of 16 surgeons performed a target identification task within the orbits of 4 skull phantoms. The task consisted of identifying the correct target, indicated by the augmented video and the pre-operative imaging frames, out of four possibilities. For each skull, one orbital intervention was performed with video augmentation, while the other was done with the standard image-guidance technique, in

random order. We measured a target identification accuracy of 95.3% and 85.9% for the augmented and standard cases, respectively, with statistically significant improvement in procedure time ($Z = -2.044$, $p = 0.041$) and intra-operator mean procedure time ($Z = 2.456$, $p = 0.014$) when augmentation was used. Improvements in both target identification accuracy and interventional procedure time suggest that endoscopic video augmentation provides valuable additional orientation and trajectory information in an image-guided procedure. Utilization of video augmentation in transorbital interventions could further minimize complication risk and enhance surgeon comfort and confidence in the procedure.

Introduction

Image-guidance, namely the use of tracked instruments and medical imaging to guide a procedure, has become a popular option in several surgical applications due to reduced tissue trauma to the patient, lower risk of infection, and faster recovery time. In additional to these benefits of a minimally invasive approach, image-guided procedures are capable of navigating to certain anatomical regions that are otherwise impractical to reach with a traditional open paradigm. The soft tissues region behind the eyeball, known as the retrobulbar space, is one such region, with access limited by the bony confines of the orbit and the anterior presence of the globe. Furthermore, the critical importance of the optic nerve and the extraocular muscles to patient well-being necessitates a high degree of delicacy in any intervention.

There are several medically relevant motivations to pursue access to the retrobulbar space, including optic sheath fenestration, tumor biopsy, and foreign object removal. At present, these procedures require cutting through the orbital bones to provide open access to the target or compromising the globe or other soft tissue, so alternative minimally-invasive approaches are

desirable. Furthermore, the development of a safe, minimally-invasive transorbital image-guidance system would allow for therapeutic techniques that are presently not feasible, such as direct drug treatment of optic nerve.

Current pharmacological therapies for the treatment of chronic optic neuropathies such as glaucoma are often inadequate due to their inability to directly affect the optic nerve and prevent neuron death, spurring interest in neuroprotective strategies [16, 24]. While drugs that target the neurons have been developed, existing methods of administration are not capable of delivering an effective dose of medication along the entire length of the nerve. Eye drops are quite limited due to poor penetration to the back of the eye, with only very small quantities of the active drug being taken up by the optic disc. Intravitreal injections are somewhat more effective but come with risks of retinal detachment, infection, and intraocular hemorrhage. Both techniques are only capable of delivering drugs to the optic disc, while recent research has suggested that the primary site of glaucomatous optic neuropathy is in the axons [24].

Minimally-invasive surgeries often include the use of endoscopy for visualization of the target region. Such procedures are not common in ophthalmology [80], with most existing implementations featuring sinonasal approaches for orbital wall repairs [81] and decompression [82, 83]. Balakrishnan and Moe [71] describe over 100 transorbital endoscopic surgeries using a variety of non-sinonasal approaches, including lateral retrocanthal, lower transconjunctival, and precaruncular, and demonstrate that there is no statistically significant difference in treatment success rate when compared to the transnasal approach. They also report no complications or resulting vision loss due to the use of endoscopy and highlight the benefits and versatility of endoscopic visualization in the orbital region. However, the majority of their cases were targeted

at orbital wall fracture repairs and not the interior retrobulbar space, and utilized rigid endoscopes.

Mawn *et al*. performed optic nerve fenestration on a series of porcine animal models with a thin flexible endoscope and a free electron laser [61], finding that although this procedure was feasible, it was particularly tedious and time-consuming due to the difficulties in distinguishing tissue types within the retrobulbar space. The optic nerve and surrounding orbital fat are both white in color with smooth texture, so navigating the endoscope to the nerve without damaging it due to reckless endoscope movement was a considerable obstacle. This scenario makes a case for the use of image-guidance. Atuegwu *et al.* developed an image-guided endoscopic navigation system catered to the specific needs of reaching the retrobulbar space, improving visualization and orientation for the surgeon and ideally enabling feasible interventions targeting the optic nerve [62]. This system employs magnetic tracking in order to localize the tip of a thin flexible endoscope, which is then registered to a pre-operative image volume, allowing the surgeon to visualize the simultaneous positions of orbital structures and the inserted instrument.

Previous work by Ingram *et al.* has investigated the performance of this system in skull phantom models, comparing target identification accuracy and procedure time with image guidance to stand-alone endoscopy [72]. While accuracy was 84.6% with the navigation system compared to 78.6% with only endoscopy, trends in procedure time were inconclusive due to limited number of interventions. Ingram *et al.* suggest more trials per subject to account for learning.

While image-guided endoscopy provides critical spatial awareness with respect to the working environment, it is still limited to three orthogonal viewing planes intersecting the tracked scope. If the target region is not within these planes, maintaining correct orientation

during navigation can be a challenge. Sielhorst *et al.* highlight the desire to provide regular anatomical context in endoscopic video due to the constant flux in point of view, specifically with integration and overlay of pre- or intra-operatively obtained three-dimensional structural information [68]. Endoscopic video augmentation, a form of augmented reality, requires a registration between the two-dimensional space of the video stream and the three-dimensional space of the pre- or intra-operative image volume. The 2D/3D mapping allows given anatomical feature locations, segmented or marked in the image volume, to be overlaid in real time onto endoscopic video. There have been a diverse group of endoscopic guidance systems designed around this concept, with implementations for neurosurgery [84], sinus surgery [75], pituitary surgery [74], skull base surgery [76], and hepatic surgery [69].

The additional guidance component provided by endoscopic augmentation is particularly useful in surgical situations where the endoscopic video field and the path to the target is severely visually occluded, a scenario existing in transorbital procedures due to the presence of fat tissue surrounding orbital soft tissue structures. Any intervention targeting the optic nerve must traverse through this fat, and is further complicated by the similarity in color of the two tissue types as described previously. As such, it was of interest to test the transorbital image guidance system in a live animal model to determine its capabilities under the conditions of a more realistic operating environment. DeLisi *et al.* prepared a series of anaesthetized pigs by inserting two small spherical targets into the retrobulbar space of each orbit and utilizing the image guidance system to navigate to and identify them, measuring identification accuracy and procedure time [85]. The experiment was performed in three pigs using image guided endoscopy and three pigs using an additional simple implementation of video augmentation. While the surgeon was able to correctly identify the target in all cases, the intervention times were

drastically different, taking approximately 3 minutes with augmentation and 20 minutes without it. These results, while limited in scope and restricted to one surgeon, indicate that video augmentation could have a positive effect in transorbital endoscopic applications.

The research described in this paper explores the value of video augmentation in transorbital image guided endoscopic surgery. We utilize a more comprehensive implementation of augmentation than that found in DeLisi *et al.* [85], while incorporating more trials across a group of volunteer surgeon operators as suggested by Ingram *et al.* [72]. We hypothesize that the incorporation of this additional visualization element will demonstrate measurably superior results when compared to the standard system, particularly in terms of procedure time.

Methods

System components

The endoscopic system consists of a Karl Storz Telecam NTSC camera system attached to a Karl Storz 11264BBU1 flexible hysteroscope. The hysteroscope was chosen for orbital application due to its small 3.5 mm tip diameter and 1.3 mm working channel. Spatial localization is provided by the Northern Digital Aurora electromagnetic tracking system using a thin 6 degrees of freedom (DOF) sensor that is inserted down the endoscope's working channel. The Aurora planar field generator is mounted on an adjustable articulated arm to facilitate the positioning of the target within the ideal working volume described by Atuegwu *et al.* [42]. The sensor was adhered to the tip of the scope to prevent rotation. In addition, its length was secured by a plastic clasp at the entry end in order to ensure that it remained in the same relative spatial relationship with the endoscope. The endoscope with the sensor protruding (prior to being fixed within the working channel) can be seen in Figure 15, with the tip shown in Figure 16.

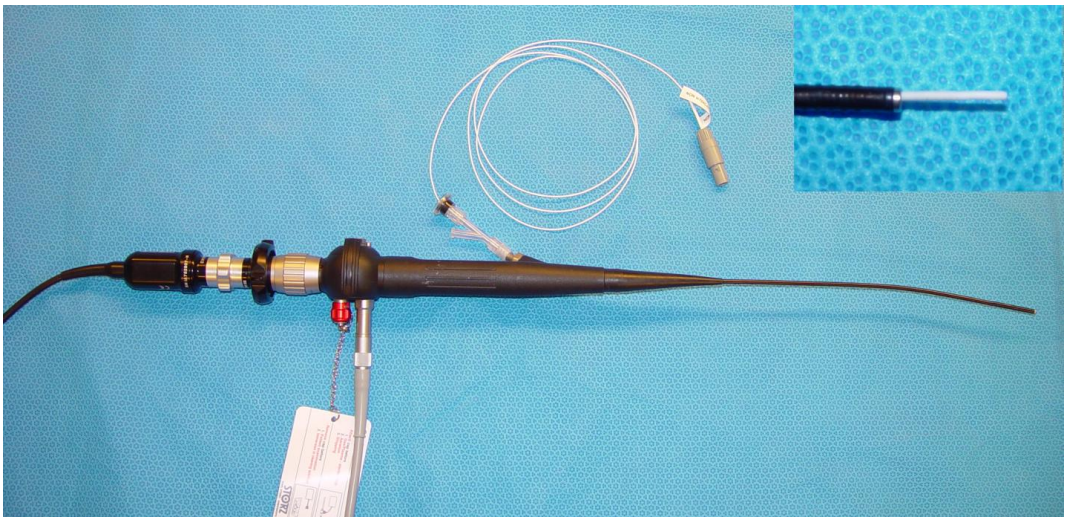

Figure 15. Flexible endoscope with inserted magnetic tracker. The inset in the upper right corner shows the sensor slightly protruding from the working channel of the endoscope.

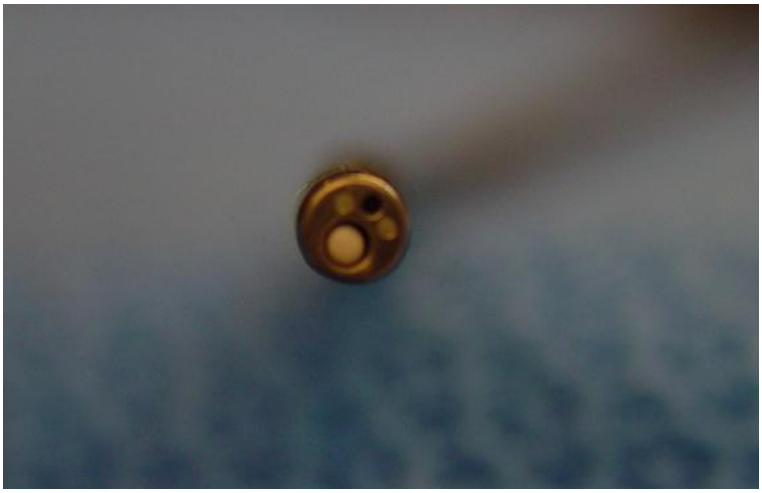

Figure 16. Endoscope tip with tracker inserted.

The endoscope was also attached to a Karl Storz 615 Xenon light source and a carbon dioxide insufflation pump to augment visualization *in vivo*. Video processing and display was performed by an Intel Core2 Duo machine running Windows 7 and equipped with a Euresys Piccolo frame grabber card.

The ORION software system [63] was used to facilitate image guidance. ORION is a flexible image-guided surgery software framework that allows various task-oriented modules to run simultaneously in accordance to the needs of the specific scenario, with four available windows for visual user interface. The transorbital surgery configuration consists of three pre-operative image volume display windows arranged in orthogonal planes (sagittal, coronal, and transverse). A localization routine provides an initial opportunity to gather fiducial points while also constantly updating the system with the position of the 6 DOF sensor. Image-to-physical space registration is performed using the fiducial point set and an implementation of Horn's method [86], with the registered location of the tracked endoscope tip being displayed in all three image planes. A separate module updates the fourth window with the endoscopic video stream and performs the augmentation computations.

3D/2D mapping

Augmented reality video systems fundamentally require a registration of 3D information to the 2D image plane. This registration was accomplished using the Direct Linear Transform (DLT) method [70], a mapping operation that provides the ability to accurately correlate points from the three-dimensional physical space of an operating room to pixels in the two-dimensional image space of the endoscopic video stream. The DLT is represented by the following equation:

$$\begin{bmatrix} w \cdot u \\ w \cdot v \\ w \end{bmatrix} = \begin{bmatrix} a_{11} & a_{12} & a_{13} & a_{14} \\ a_{21} & a_{22} & a_{23} & a_{24} \\ a_{31} & a_{32} & a_{33} & a_{34} \end{bmatrix} \begin{bmatrix} x \\ y \\ z \\ 1 \end{bmatrix} \quad (1)$$

where (x, y, z) is the three-dimensional point in physical space, (u, v) is the resulting point in two-dimensional space, *w* is a scaling factor, and *A* is the homogeneous transformation matrix (HTM). The equation uses homogeneous coordinates since it deals with projective space calculations, therefore the HTM has 11 independent elements and a_{34} is set equal to 1. The other parameters in the HTM represent the 11 degrees of freedom involved in the transformation from 3D space to 2D space, namely three translations, three rotations, source-to-image distance, the intersection point of the imaging plane and optical axis, and scaling factors in the *u* and *v* directions.

An HTM for a projection from 3D physical space into a particular 2D image space must be calculated using a known set of corresponding points, specifically:

$$(x, y, z)_n \rightarrow (u, v)_n$$

where *n* is the size of the set of points. Expanding equation (1) yields an expression for *w*:

$$w = a_{31} \cdot x + a_{32} \cdot y + a_{33} \cdot z + 1 \tag{2}$$

Substituting for *w*, *u* and *v* can be expressed as:

$$u = a_{11} \cdot x + a_{12} \cdot y + a_{13} \cdot z + a_{14} - a_{31} \cdot x \cdot u - a_{32} \cdot y \cdot u - a_{33} \cdot z \cdot u \tag{3}$$

$$v = a_{21} \cdot x + a_{22} \cdot y + a_{23} \cdot z + a_{24} - a_{31} \cdot x \cdot v - a_{32} \cdot y \cdot v - a_{33} \cdot z \cdot v \tag{4}$$

Expanding equations (3) and (4) for a set of corresponding points in 2D and 3D of size *n* results in:

$$\begin{bmatrix} u_1 \\ v_1 \\ u_2 \\ v_2 \\ \vdots \\ u_n \\ v_n \end{bmatrix} = \begin{bmatrix} x_1 & y_1 & z_1 & 1 & 0 & 0 & 0 & 0 & -x_1 \cdot u_1 & -y_1 \cdot u_1 & -z_1 \cdot u_1 \\ 0 & 0 & 0 & 0 & x_1 & y_1 & z_1 & 1 & -x_1 \cdot v_1 & -y_1 \cdot v_1 & -z_1 \cdot v_1 \\ x_2 & y_2 & z_2 & 1 & 0 & 0 & 0 & 0 & -x_2 \cdot u_2 & -y_2 \cdot u_2 & -z_2 \cdot u_2 \\ 0 & 0 & 0 & 0 & x_2 & y_2 & z_2 & 1 & -x_2 \cdot v_2 & -y_2 \cdot v_2 & -z_2 \cdot v_2 \\ \vdots & \vdots & \vdots & \vdots & \vdots & \vdots & \vdots & \vdots & \vdots & \vdots & \vdots \\ x_n & y_n & z_n & 1 & 0 & 0 & 0 & 0 & -x_n \cdot u_n & -y_n \cdot u_n & -z_n \cdot u_n \\ 0 & 0 & 0 & 0 & x_n & y_n & z_n & 1 & -x_n \cdot v_n & -y_n \cdot v_n & -z_n \cdot v_n \end{bmatrix} \begin{bmatrix} a_{11} \\ a_{12} \\ a_{13} \\ a_{14} \\ a_{21} \\ a_{22} \\ a_{23} \\ a_{24} \\ a_{31} \\ a_{32} \\ a_{33} \end{bmatrix} \quad (5)$$

Calibration consists of gathering set of corresponding point coordinates in both 2D and 3D space, populating equation (2) with the values, and solving for the vector *a* using the pseudo-inverse of the 11xN matrix. The vector *a* is then reconstituted as the HTM.

For any 3D point (x, y, z), w can be solved with equation (2), and the resulting mapped point in 2D space (u, v) is determined with equations (3) and (4). This 3D point can be the location of tracked tools in physical space or the position of targets or segmented structures from a pre-operative medical image volume, assuming an accurate registration from image space to physical space. In this application of video augmentation, we are interested overlaying the position of a known target in a pre-operative CT scan onto the endoscopic video in real-time in order to enhance guidance and improve spatial awareness in a visually occluded environment.

Lens distortion correction

Lens distortion is a known feature of endoscopic images. The approximately radial effect can appreciably compromise user perception of depth, size, and structure. With practice and experience, human operators may be able to adapt to the distortion in order to perform their given medical tasks, whether it be minimally-invasive interventions or exploratory diagnosis. However, the effect has particularly relevant impact in the context of computer vision,

specifically for video augmentation capabilities, as error is introduced if the camera model is assumed to be undistorted [87].

Improvements in endoscope optics on the manufacturer's end can lessen the degree of radial distortion but not fully correct it. As such, it is necessary to rectify the images in software prior to them being displayed. The process of intrinsic camera calibration involves generating a model of the distortion and subsequently using it to warp the camera output. The models are often developed using calibration images of checkerboard or grid patterns with known sizes and dimensions. One of the most popular means of camera calibration is Bouguet's toolbox for Matlab [77], which utilizes methods developed by Zhang [78] and Heikkil and Silven [88] within a straightforward user interface for comprehensive camera parameter calculation and optimization. Several other solutions have been developed for intrinsic camera calibration, with emphasis on automatic techniques [89] and minimizing calibration images [90]. These solutions offer advantages when camera calibration represents a major workflow bottleneck, which is particularly relevant in clinical systems where ease-of-use and time efficiency have considerable financial repercussions. However, most require high quality calibration images to converge. The small scale of the orbit and its internal soft tissue structures, along with the need to navigate around the eye ball, require any transorbital interventional endoscope to be both flexible and have a small diameter. The Karl Storz 11264BBU1 endoscope used in this experiment produces relatively low resolution images, and thus the more sophisticated correction techniques were not appropriate.

A series of 18 images of a black and white checkboard pattern with known dimensions were taken at various angles and distances from the endoscope tip. Bouguet's toolbox was used to find the corners of each square in the checkerboard images, often with manual corrections, and

subsequently generate the intrinsic camera parameters, namely the focal length, principal point, and image distortion coefficients. These parameters were implemented with OpenCV functions [79] to rectify each new image frame from the endoscope as they are displayed by the ORION module. Figure 17 shows a distorted and corrected calibration image.

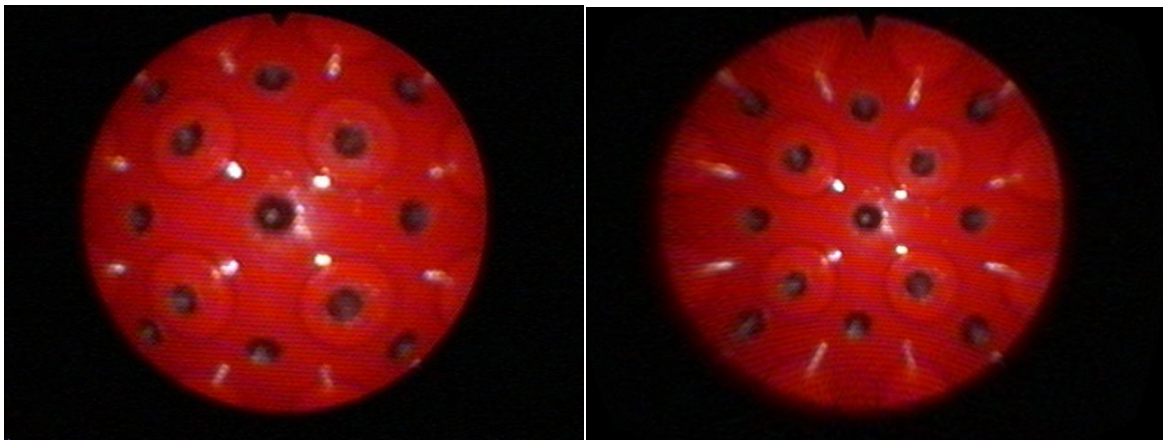

Figure 17. Distorted (left) and corrected (right) calibration image.

Calibration procedure

It is desirable to represent a large portion of the conical projection volume in the range of this transformation since structures of interest may be out of direct line of sight of the camera due to the presence of intermediary objects. As such, calibration of the HTM using equation (5) was performed with a set of 3D points $(x,y,z)_n$ that sampled a volumetric region of interest roughly the size of a human orbit at various depths, with corresponding 2D points $(u,v)_n$ to characterize the endoscopic video output. The 2D calibration points were collected from endoscopic video images that had already undergone lens distortion correction as described in the previous section.

For calibration, the base and tip of the endoscope were fixed on an immobile stand to ensure a constant position of the magnetically tracked sensor within the tip. A phantom

containing 13 points in an approximate alternating-row grid arrangement was then placed in front of the endoscope tip. The Aurora field generator was positioned such that the endoscope tip and the phantom were within its optimal working volume. Each point of the phantom consisted of a colored indentation such that they could be easily localized in physical space using the Aurora pen probe without it slipping, and be easily annotated in image space due to the color difference from the background.

Starting with a phantom distance of approximately 1 cm from the endoscope tip, an endoscope image of the phantom points was taken and their 3D positions were collected using the Aurora probe. The phantom was then moved back from the tip by approximately 1 cm, and the procedure was repeated. The phantom was replaced with a larger version after the approximate 3 cm distance mark to maintain sampling of the edges of the endoscope image. A total of 91 calibration points were collected, at 7 different phantom distances from the endoscope tip.

The 3D coordinates of each calibration point were transformed with respect to the position of the fixed magnetic sensor within the tip, such that the tip was considered to be the origin. This allows the HTM to remain valid throughout endoscope movement and rotation, so long as the transformed 3D point of interest is converted to the tracked tip's coordinate system. The 2D calibration point coordinates were annotated manually. The resulting set of points was used to populate equation (5) and calculate the HTM.

The integrity of the calibration was tested by running every 3D calibration point through the determined HTM and comparing the distance between the calculated 2D point and the actual 2D calibration point. This distance was designated as the calibration error. A mm/pixel ratio was calculated for each phantom position using the width of the central colored indentation in

millimeters and the width of the same indentation in pixels for the endoscope image of that given position. Using these ratios, the average distance calibration error across the set of 91 points was found to be 0.395 mm.

Phantom preparation

Performance validation of transorbital interventional systems is particularly challenging due to the intricate, small-scale anatomy of the target region. Any model of the orbit to be used for surgical testing must adhere to a few basic principles. First, the proportions of the region must be similar to human anatomy. Second, the spatial obstacles present when accessing the retrobulbar space must be maintained. Lastly, the visual field of the endoscope must be occluded. We have previously developed a phantom to conform to these restrictions [72], and a modified version is presented below.

Four skull phantoms were built for the purpose of this experiment. Each consisted of a different commercially available plastic skull model. A total of 10 radiographic skin fiducial markers were placed on each skull, with care taken to surround each orbit. The interior of each orbit was thinly padded to ensure that the contents would not spill out of the various fissures and openings present in the modeled bone. Four small, differently colored stellate balls were attached to the orbital wall deep within the retrobulbar space, one of which was previously soaked in a barium solution in order to appear bright on a CT scan. The presence or absence of barium was indistinguishable upon visual inspection. The barium ball was designated as the target, while the others were to serve as distracters. The color of the target ball for each orbit was recorded by the investigator. Figure 18 shows an example orbit with the attached balls.

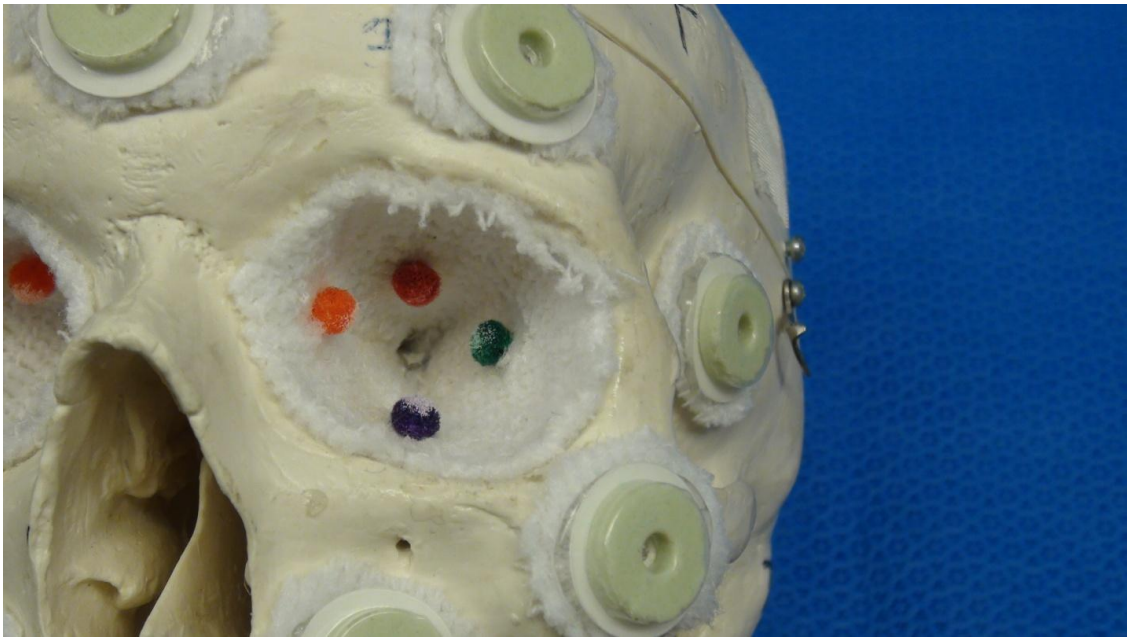

Figure 18. Phantom orbit with attached colored stellate balls.

Realistically proportioned silicone rubber spheres were attached to nylon cords and fixed within the optic canal, simulating the human eyeballs and optic nerves and presenting the physician with spatial obstacles. The remaining intraorbital space was then filled with white polystyrene foam beads. These small beads would mimic fat tissue upon insertion of the endoscope by separating with a light application of force, but still occluding the visual environment to the operator. A complete skull phantom can be seen in Figure 19. The skulls were securely mounted with an angled stand such that when the base of the mount was clamped to a table, the phantom was positioned to mimic a supine patient. Computed tomography (CT) scans were taken of each skull phantom, and the locations of the fiducial markers and the barium-soaked stellate balls were manually annotated in the image volume and recorded for use by the guidance system.

Figure 19. Complete skull phantom.

Experiment protocol

A given skull phantom was securely clamped to an immobile table with the Aurora field generator positioned near the crown of the head such that both orbits were within its optimal detection volume. The 10 fiducial markers surrounding the orbits were spatially localized with the Aurora pen probe and registered to their previously manually annotated image-space counterparts using Horn's method [86]. Figure 20 shows a skull phantom in an appropriate experimental configuration.

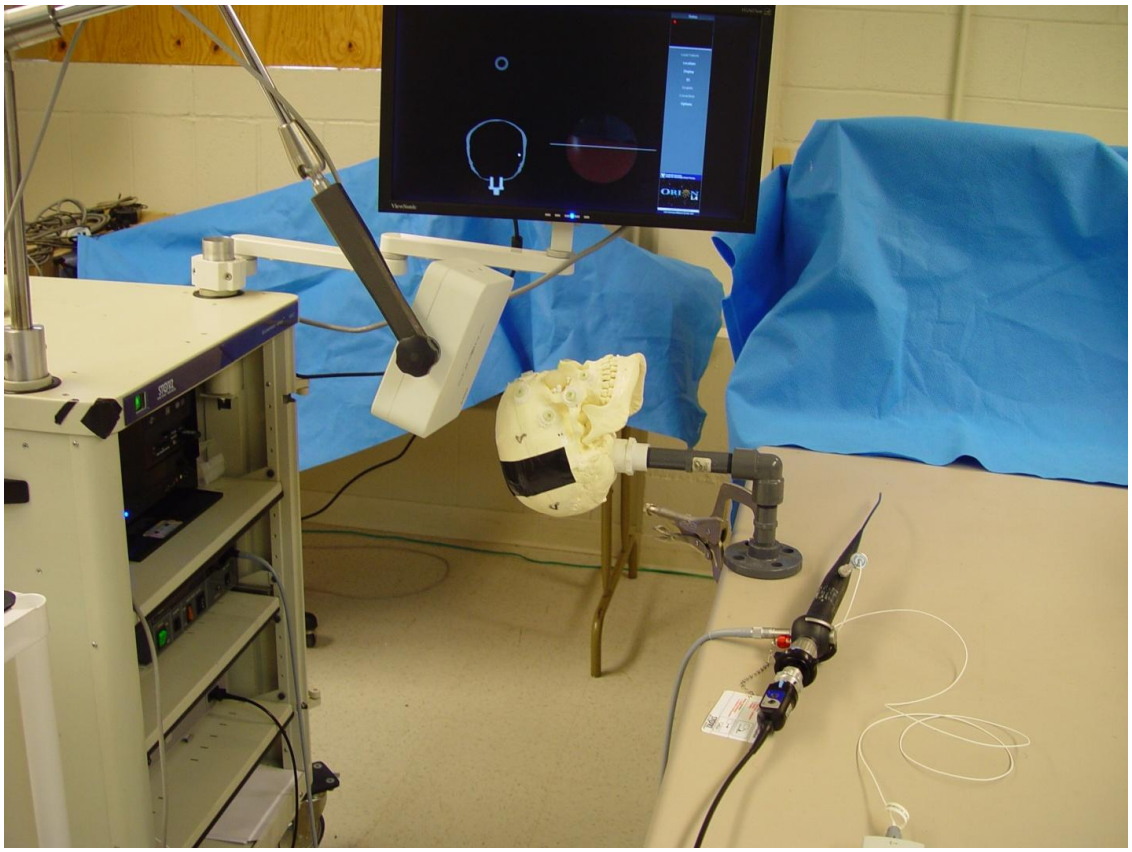

Figure 20. Skull phantom in experimental configuration.

A total of 16 surgeons volunteered their time to assist in this experiment. This group included attendings, fellows, and residents from the surgical departments of ophthalmology, otolaryngology, gastroenterology, gynecology, and urology. Most had substantial experience with minimally-invasive surgery and endoscopy.

While the skull phantom was being registered and the appropriate ORION displays were being set up, the surgeon would reference the pre-operative CT scans of the phantom, note the relative locations of the target stellate balls, and formulate a navigation plan. After these preparation tasks were completed, the surgeon would take position next to the skull phantom, indicate readiness, insert the endoscope, and then perform the navigation task. A timer was started upon surgeon indication of readiness and ended upon declaration of target identity. The

recorded metrics for each orbit was target identification accuracy (whether or not the surgeon correctly identified the barium-soaked ball by color) and procedure time. An orbital procedure was halted and declared to be an inaccurate identification if the surgeon had not declared a target by the 2 minute mark.

An example ORION display screenshot for an accurate target identification can be seen in Figure 21. Note that the video augmentation points to the position of the target ball, which is verified by the appearance of the target in the orthogonal image planes. Figure 22 demonstrates the discovery of a non-target colored ball. The augmentation clearly indicates that the real target is elsewhere, while the bright spot in the CT scan is not present.

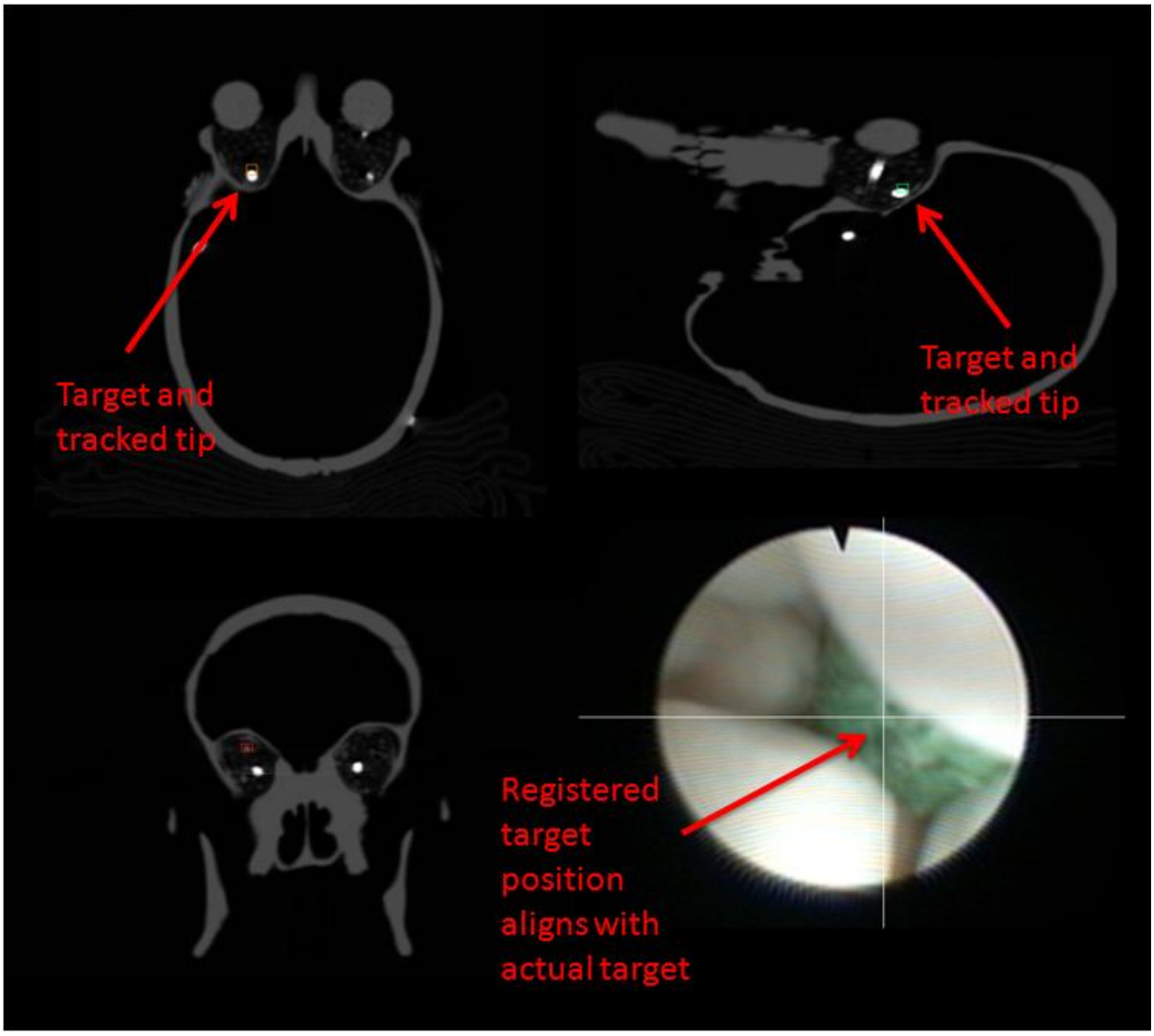

Figure 21. Correct target identification with video augmentation. The radio-opaque ball can be seen in the sagittal and transverse slices as the round bright spot. The small boxes in the CT images represent the registered position of the endoscope tip. The intersected lines on the endoscopic video frame indicate the location of the target.

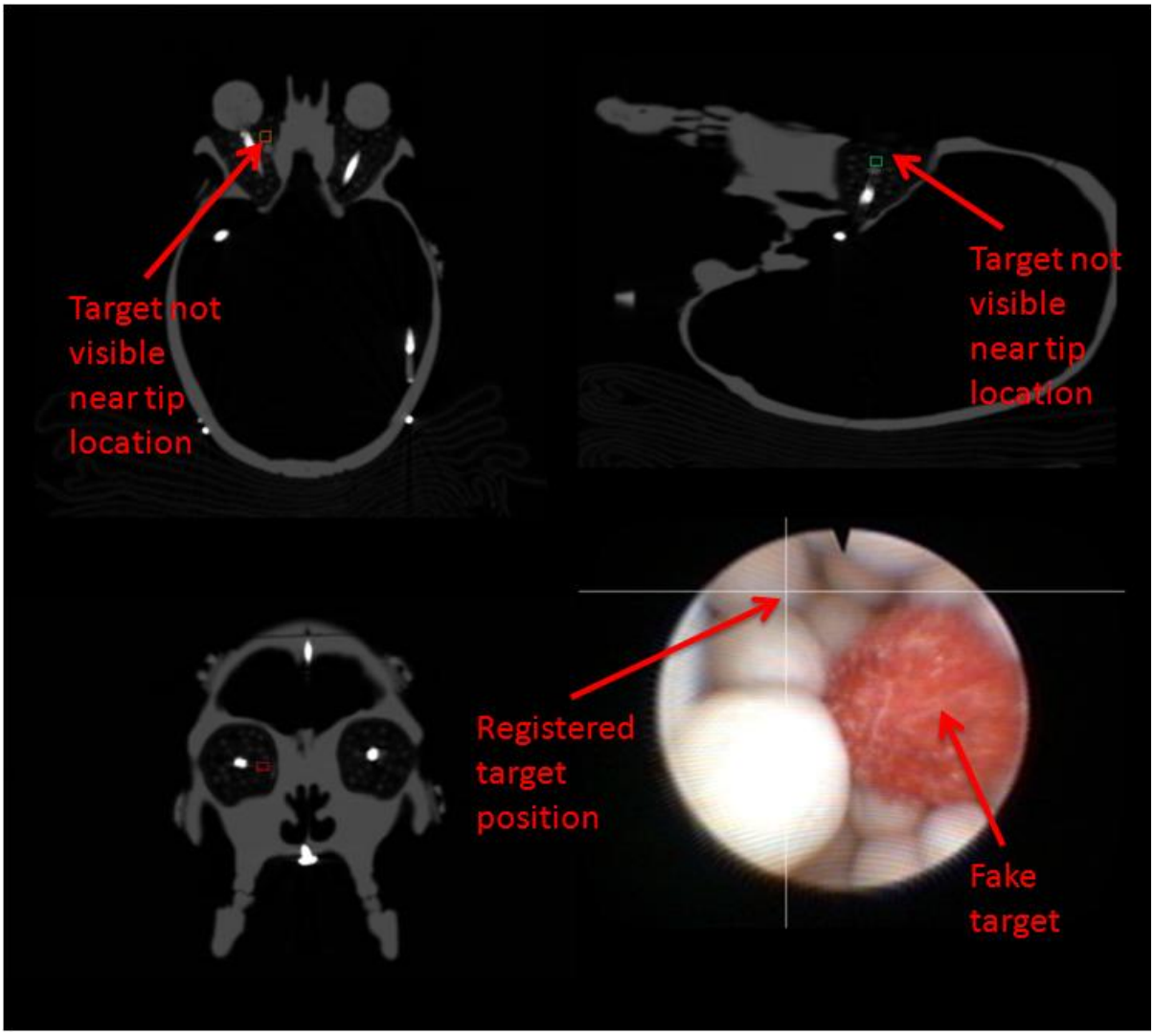

Figure 22. Incorrect target identification with video augmentation. The intersecting lines in the endoscopic video frame indicate that this colored ball is not the target, while there is no radio-opaque object near the registered endoscope tip on the CT images.

For each skull, one orbital procedure was performed with video augmentation while the other was performed without it, in random order. Augmentation was implemented as a simple pair of lines overlaying the video feed and intersecting at the 2D target location as determined by the HTM. The presence or absence of this display component was the only difference between augmented and un-augmented procedures. Upon completion of both orbital procedures in the

first skull, the process was repeated for the three additional skulls. The entire experiment took approximately 30 minutes to complete for each surgeon.

Results

With 16 surgeons performing 8 orbital interventions each, there were a total of 128 data points, 64 using the augmented video and 64 using the basic guidance system. The barium-soaked stellate ball target was correctly identified with 95.3% accuracy using augmented video and 85.9% accuracy without it. This represents an augmented miss rate of approximately 1/3 of the un-augmented miss rate. It could be expected that the first skull phantom tested would skew the data somewhat due to surgeon unfamiliarity with the procedure. However, if the data from the first skull phantom is removed, the augmented and un-augmented accuracies demonstrate little change, with values of 95.8% and 85.4%, respectively.

Only procedure times from phantom experiments where the target was successfully identified were considered for analysis. The average procedure times for the augmented and un-augmented interventions were 18.3 and 23.9 seconds, respectively, with standard deviations of 11.3 and 15.4. As this data set was not normally distributed, a two independent sample Wilcoxon rank-sum test (Mann-Whitney *U* test) was performed to determine the effect of augmentation on procedure time tendencies. The results indicated that the two groups were significantly different (Z = -2.044, p = 0.041), with augmentation tending to result in faster procedure times (p = 0.020). The procedure times for both cases can be seen in Figure 23.

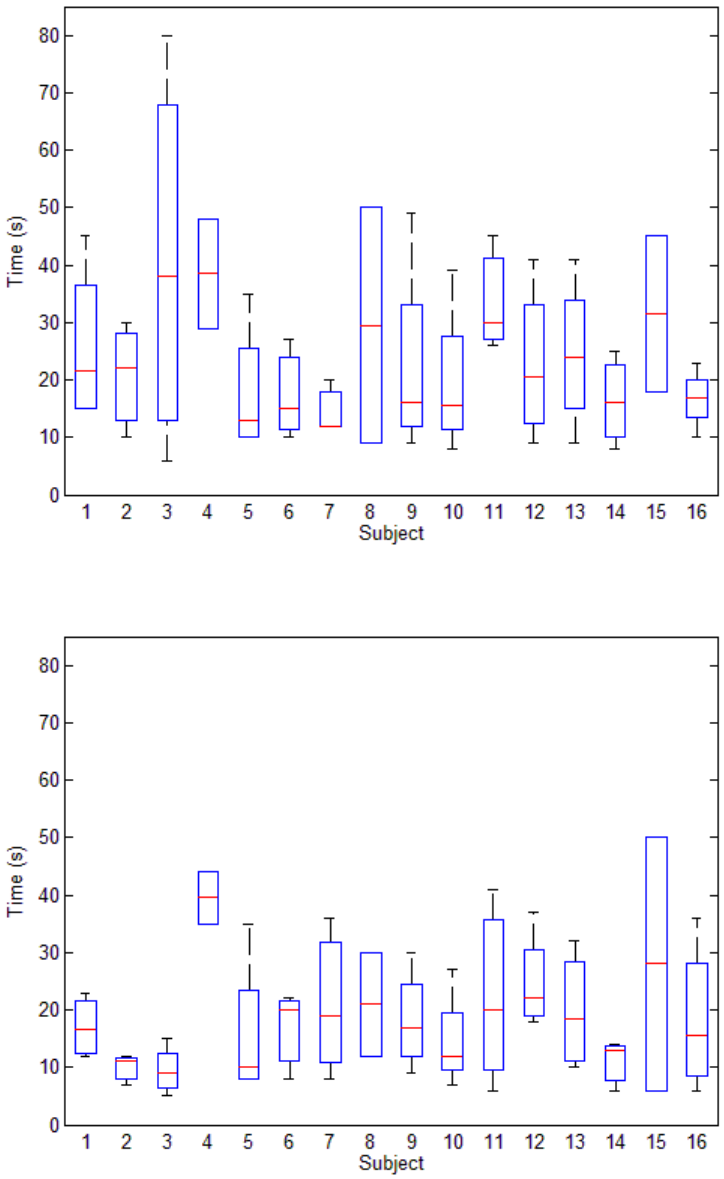

Figure 23. Procedure times without (top) and with (bottom) video augmentation. The times with video augmentation are typically shorter and with smaller deviations than their un-augmented counterparts.

To account for inter-operator variability, mean augmented and un-augmented procedure time was computed for each surgeon. These means can be seen in Figure 24. The resulting population of 32 means satisfied the chi-square goodness-of-fit test for a normal distribution and was thus analyzed with a two-sided paired sample *t*-test. The test indicated a significant

difference in procedure time between the augmented (mean = 19.2) and standard (mean = 24.5) guidance system (T = -2.526, p = 0.023). If the data is not considered normal, the two paired sample Wilcoxon signed-rank test also indicated significant difference between the two groups (Z = 2.456, p = 0.014).

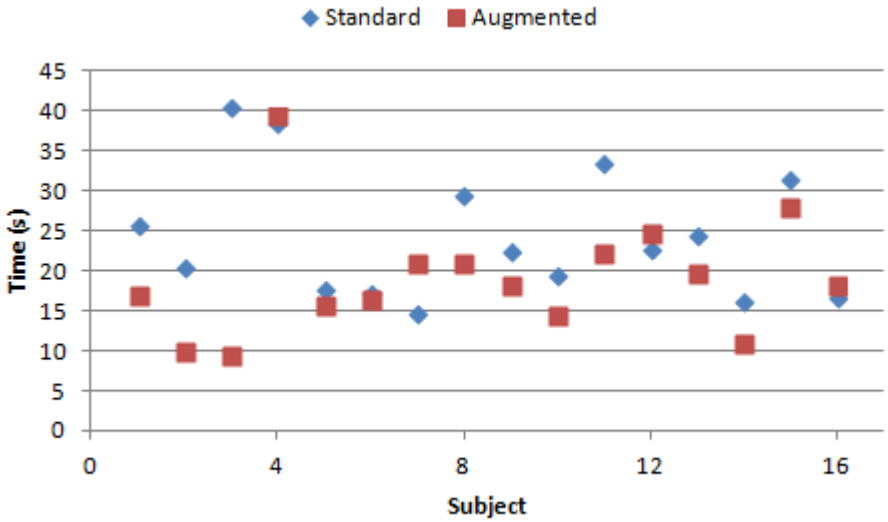

Figure 24. Intra-surgeon mean times. The mean augmented time for each surgeon tends to be lower than their un-augmented time.

Discussion

It is important to be aware of the characteristics of orbital surgery when making any judgment about the system performance. The orbit is a very small space, and thus finding an interior object without direct visualization should theoretically not take a large amount of time. However, the risk of causing severe impairment to a human patient is quite real if a mistake is made, necessitating a high degree of caution and steadiness for any transorbital intervention in a live subject. This scenario is extremely difficult to replicate in anthropomorphic phantom model experiments. While surgeons were encouraged to proceed as if they were operating on a live subject, it was clear to the investigator that this was not always the case, particularly if the target

was not found after the first insertion of the endoscope. Since the phantom is fundamentally immune to harm, it is inevitable that the primary goal of the operator is to find the target, as opposed to avoiding imagined negative effects to the patient.

This effect is further exacerbated by the limited realism in phantom construction. While measures were taken to provide substitute materials for the optic nerve, eye ball, and fat tissue, the extraocular muscles were not modeled due to their particularly complex arrangement. As such, the orbit and optic nerve were substantially more mobile than would be allowed in human case, as the attached muscles would hold them in place more securely. The absence of muscles also eliminated a noteworthy structural obstacle in transorbital surgery; while endoscope impact with the muscles is not as critical as reckless optic nerve contact, they take up a considerable volume of orbital space and navigation must be planned accordingly. Furthermore, the polystyrene beads used to model fat would occasionally pack together and inhibit endoscope movement. This was particularly evident in the augmented cases, where the surgeon would attempt to drive the scope straight forward as indicated by the intersecting target lines, but would be unable to move a polystyrene bead out of the way. In these cases, the guidance system and augmentation clearly indicated that the target was directly beyond the bead, but visual confirmation was impossible and another route had to be taken. Finally, the targets were embedded on the walls deep within the orbit and not suspended in the interior retrobulbar space, as this would be particularly difficult to implement without them substantially moving position and rending the pre-operative imaging scan useless.

Despite the inability of the phantom to encompass all of the anatomical intricacies of the human orbit, it still provided a realistically proportioned working space, modeled the primary obstacle of navigating around the eye ball, and exhibited the characteristic endoscopic visual

occlusion of fat tissue. While each surgeon performed the task with different degrees of delicacy, they were consistent in their approach for all trials, as the investigator did not instruct them to change behavior after the initial explanation of the experiment.

In light of these experimental limitations, we are encouraged by the results. The implementation of video augmentation had a clearly positive impact on transorbital procedures performed in skull phantoms. The measured results quantitatively indicate that video augmentation improves the accuracy of target identification, while also decreasing the procedure time for successful navigations. This outcome has important clinical value. Considering the delicate nature of the optic nerve, any therapeutic intervention must be precisely guided and controlled, minimizing harm to the surrounding tissue while successfully completing the given task. These expectations are reliant on a highly accurate targeted navigation.

When considering the difference in navigation times in terms of raw seconds, the improvement from standard to augmented may not seem particularly impactful, with a mean difference of 5.6 seconds. However, faster procedure times with statistically significant consistency are indicative of a superior sense of surgeon orientation within the operational space, as well as a higher degree of comfort with the tools and task. Given the aforementioned limitations of the skull phantoms, particularly the obstructive effect of the polystyrene beads, it is not unreasonable to expect a greater time difference under more realistic conditions.

While the implementation of video augmentation in this experiment was limited to a simple indication of the direction to a target, the mapping of 3D space to 2D space allows for the incorporation of much more sophisticated visualization displays. Such possibilities include non-linear pre-operatively planned surgical paths and overlaid soft tissue structures, using 3D points generated from existing orbital soft tissue image segmentation algorithms [67, 66]. So long as

care is taken to avoid overwhelming the display with extraneous visual information by constantly obtaining surgeon feedback, this technology could considerably simplify retrobulbar access and enable safe, repetitive therapeutic interventions.

Conclusions

The delicate anatomy of the orbital space requires any intervention to be precise and clearly directed, with minimal superfluous motion to avoid inflicting damage to the patient. While standard image guidance provides critical information regarding instrument location and surrounding anatomy, the typical interface of three orthogonal image planes leaves an awareness gap in terms of orientation and trajectory, particularly when the endoscopic viewing field is occluded by blood or tissue. This additional information can be provided with video augmentation. In this series of anthropomorphic phantom experiments, we have demonstrated that both target identification accuracy and interventional procedure time are improved when image-guidance is used in conjunction with video augmentation.

Acknowledgments

We would like to thank the various physicians who volunteered their time for this experiment, Dahl Irvine and the Vanderbilt CT technicians for their help with imaging, and Tom Pheiffer, Yifei Wu, and Rebekah Conley for their assistance with calibrations. This work was supported in part by the Research to Prevent Blindness Physician Scientist Award, the Unrestricted Grant from Research to Prevent Blindness to the Vanderbilt Eye Institute, and the National Institutes of Health under Grant R21 RR025806

CHAPTER IV

CHARACTERIZATION OF OPTIC NERVE IMPACTS DURING TRANSORBITAL ENDOSCOPIC INTERVENTIONS

The work described in this chapter is being prepared for submission as a research article to the Journal of Medical Devices.

Abstract

Image-guided transorbital endoscopy has the potential for application in a variety of existing surgical objectives while enabling new avenues of optic nerve therapy. An important goal in transorbital interventions is to minimize the possibility of inflicting injury upon the optic nerve. A system has been developed that is capable of navigating to targets in the orbital space, and it is desirable to characterize the interactions between the endoscope and the optic nerve in both quantitative and qualitative terms. In this research, a phantom model of the orbit and optic nerve is developed, with the capacity to measure imparted force on the taut optic nerve along its primary axis due to an endoscopic intervention. Additionally, a proximity detection visualization scheme is developed to constantly supply the operator with an indication of the distance relationship between the endoscope and the optic nerve. Procedures were performed on the phantom by two surgeons, with each trial grouped according to surgeon experience with the system, use of the proximity detection scheme, and anatomical location of the target. It was found that surgeon experience and target location with regard to orbital depth were significant factors in measured force applied over the course of the procedure. Existing literature was used

to determine force and strain injury thresholds, which were not violated during experimental procedures. Direct tests of the biomechanical properties of the intraorbital optic nerve in the human adult are necessary for more definitive statements regarding injury thresholds. The results are encouraging when considering that experiments did not account for intraorbital optic nerve slack and the protective properties of orbital fat, indicating even smaller imparted forces *in vivo*.

Introduction

Transorbital surgery refers to interventions in the region behind the eyeball, or the retrobulbar space. There are several purposes for transorbital interventions, such as tumor biopsy, orbital wall repair, optic nerve decompression, optic nerve fenestration, and foreign object removal. In order to complete these procedures, the surgeon must be able to perform highly precise movements within a relatively small volume, while maintaining awareness of critical interior soft tissue structures to avoid unnecessary damage. Transorbital surgery can be highly invasive, requiring substantial trauma to the surrounding exterior tissue and bone in order to facilitate these requirements and provide the surgeon with an adequate working space.

The limitations of retrobulbar access have also inhibited the development of repeatable therapeutic procedures in the region, such as optic nerve drug therapy. Glaucoma is the most common cause of permanent vision loss in developed countries [1], yet current treatments can only slow the progression of the disease at best [9]. These methods are typically aimed at reducing intraocular pressure, and are administered in the form of topical eyedrops or intravitreal injections. However, research over the last decade has determined that the primary cause of glaucoma is neurodegeneration, which is not entirely halted with the reduction of intraocular pressure [16]. Several experts in the field [23, 25, 26] have deemed neuroprotective drug agents

as a promising therapy to stop optic nerve degeneration. These drugs have had considerable positive effects when deployed in various animal models, but this success has not yet translated to the clinic [24].

Several studies have investigated the use of neuroprotective drugs in human trials for the treatment of optic neuropathies [30, 31, 33]. A principle reason that neuroprotection has not become a standard therapeutic solution is the difficulty in delivering an effective pharmacological dose to the nerve tissue [24]. As most existing neuroprotective agents are toxic in high quantities, they must be administered locally, as opposed to systematically, with limited concentrations. Unfortunately, the most common form of local application for optical drugs, topical eye drops, have poor penetrative capacity, and only a very small effective dose of the drug actually reaches the optic nerve [12, 13].

Neuroprotective therapy has the potential to halt the progression of glaucoma and other optic neuropathies provided repetitive administration, which, given the poor effectiveness of existing delivery techniques, would suggest a minimally-invasive intervention. Minimally-invasive surgery is not common in ophthalmology [80], typically being limited to orbital wall repairs [81] and decompressions [82, 83] utilizing rigid endoscopes and a sinonasal access approach. While the sinonasal route is understandable in these cases, it is still too invasive for repetitive drug delivery. Balakrishnan and Moe [71] utilize several non-sinonasal approaches for minimally-invasive orbital surgery, such as the lateral retrocanthal, lower transconjunctival, and precaruncular, and report no significant difference in success rate when compared to the standard transnasal route. However, all of these cases utilize relatively large rigid endoscopes and are often confined to the orbital wall region, as opposed to the interior retrobulbar space.

Mawn *et al.* performed minimally-invasive retrobulbar surgery in the porcine orbit for the purpose of optic nerve sheath fenestration, using a thin flexible endoscope and free electron laser [61]. They reported successful procedures and determined that the technique had promise, but emphasized the difficulty in maintaining orientation and distinguishing tissue types within the region as the optic nerve and the surrounding fat have similar colors and textures. These difficulties translated to exceptionally long procedure times. Atuegwu *et al*. advanced the technique of transorbital endoscopic surgery by incorporating image-guidance using magnetic tracking and registration with pre-operative image volumes, enabling the operator to visualize orbital tissue structures with respect to the real-time position of the endoscope [62]. This system has been expanded by DeLisi *et al*. to include additional endoscopic enhancements using video augmentation, while also validating navigation performance in animal and phantom models [85, 91].

While these studies investigate the capabilities of image-guided transorbital endoscopy in terms of navigation and target identification, they do not explore the effect of such intervention on the surrounding tissue in quantifiable terms. Any proposed therapeutic process must not damage the patient's vision. The most likely cause of vision loss as a result of transorbital intervention is the infliction of traumatic injury upon the optic nerve axons, such as from a high energy collision with the endoscope or prolonged increased nerve tension, due to endoscope contact or elevated intraorbital pressure from the presence of the endoscope in the orbit.

Determination of possible injury to the intraorbital optic nerve during a transorbital procedure requires measurement of the disturbance forces involved, knowledge of optic nerve tissue biomechanical properties, and determination of a threshold for injury. Unfortunately, there are very limited studies with the primary aim of characterizing human optic nerve axon

mechanics or fragility in the orbital space. Several studies have investigated the impact of intraocular pressure due to glaucoma on the optic nerve and generated optic nerve biomechanical models [92, 93], but these studies primarily focus on the optic nerve head, and not the intraorbital axons. These two segments have substantially different structures and may not have identical elastic properties.

Gennarelli *et al*. developed a model of traumatic axonal injury by controlled elongation of the optic nerves of guinea pigs [94]. Elongation was performed by securing the globe in a sling and pulling it back along the primary axis of the optic nerve. The applied forces were set such that 5 mm of elongation was achieved over 20 ms, with a preload force of approximately 0.343 N and a maximum force of approximately 1.568 N. It was determined that elongation over this range was linearly elastic, with the nerve returning to its original length after force application. The nerves were then excised and analyzed with electron microscopy to determine the degree of axonal damage, using morphological changes and glucose utilization as metrics.

Bain and Meaney use a similar force-application system as Gennarelli *et al*. to injure the optic nerves of guinea pigs, but focus on the induced Lagrangian strains in an effect to determine tissue-level thresholds for axonal damage [95]. They utilize neurofilament immunohistochemical staining to quantify morphological injury, and changes in visual evoked potentials to assess functional injury, finding a bit fit strain threshold criterion to be 0.21 and 0.18, respectively.

The objective of this research is to investigate the effect of transorbital endoscopic interventions on the optic nerve in quantitative terms, particularly instances of endoscope collisions with the nerve and an assessment of the forces applied to the nerve as a result. Furthermore, an additional visualization scheme for maintaining awareness of optic nerve proximity to the endoscope tip was developed and included in the image-guided system.

An orbital phantom capable of detecting the instances and magnitudes of optic nerve contact was developed for this study. The image-guided endoscopic system was then utilized to perform a diverse set of interventional procedures on this phantom, with the resulting data being used to draw conclusions about system performance.

Methods

System specifications

The principle interventional component of the transorbital image-guided surgery system is a thin flexible endoscope, capable of navigating around the globe, between the extraocular muscle structures, and through the ocular fat tissue with minimal resistance. In order to enable image guidance, the tip of the instrument must be localized in three dimensions of physical space and registered to image space. Since the tip of a flexible endoscope can move independent of its base, the system utilizes the Aurora magnetic localization system, with the tracked probe being inserted through the working channel of the endoscope and fixed at its distal end. So long as the surgical region of interest is within the Aurora field generator's optimal working volume, the endoscope tip can be tracked without line-of-sight restrictions. The particular endoscope used in this experiment was a Karl Storz 11264BBU1 hysteroscope, as it was the thinnest endoscope available that featured a working channel wide enough to fit an Aurora 6 DOF (degrees of freedom) probe.

The Aurora field generator was mounted on an articulated arm for optimal positioning near the surgical region. A Karl Storz 615 Xenon light generator was used to enhance endoscopic visualization. The computer monitor was mounted on a swinging boom for positioning according to the surgeon's preference.

Image-guidance was facilitated by the ORION platform [63]. ORION is a flexible software framework with a modular design such that each critical component of image-guidance, such as localization, registration, and display, can be designed and integrated separately. The software allows each component to share critical information while providing a basic graphical user interface with four viewing windows. For the transorbital guidance system, the Aurora magnetic localization subroutine provided the real-time position of the endoscope tip, while registration was enabled with an implementation of Horn's unit quaternion method [86]. Orthogonal medical image planes were displayed in three of the ORION windows, while the fourth contained the endoscope video output. Endoscope lens distortion correction was implemented in ORION using OpenCV [79] with camera calibration parameters generated from Bouguet's toolbox [77].

Simulating the human orbit

The first priority of any therapeutic transorbital procedure is to maintain the current degree of visual ability in that given eye. In order for any such interventions to become a reality, it must be confirmed that they are not prone to inflict unnecessary trauma on the optic nerve during the course of surgery. This is a challenging task, as the metrics for demonstrating optic nerve trauma infliction to the point of permanent visual impairment are very impractical to obtain. There are several animal models used in ophthalmological pathology studies, though only dogs and pigs have optic nerve sizes of the same order of magnitude as humans. Ideally, survivable animal studies could be performed to gauge transorbital surgery effects, but high financial cost and ethical concerns provide significant obstacles to this approach. Furthermore, vision capabilities in humans are measured by a series of interactive tests, requiring responses

from the subject for a detailed assessment. This degree of feedback cannot be expected in an animal model. As such, we must use a secondary metric to indicate vision loss, preferably one that can be measured in a non-living anatomical model, or phantom. This can be expressed quantitatively in terms of the frequency and intensity of optic nerve impact during an endoscopic procedure.

The purpose of this study was to simulate the surgical task of optic nerve access and measure all collision events during the course of the experiment. As such, the phantom model should exhibit a series of features to ensure a degree of realism. The surgical region of interest should be within expected human parameters. Average adult human orbital volume is 30 mL, with optic nerve thickness of 3.5 mm [96]. Endoscopic access should be constrained to a single entry point to model a single incision pathway. The endoscope should be required to traverse through an opaque substance with the same color intensity as the optic nerve substitute to reflect the relationship between the orbital fat tissue and the optic nerve. Finally, the optic nerve substitute must be sensitive to physical impacts by the endoscope.

Phantom design

In previous studies [72, 91], we have utilized anthropomorphic skull phantoms in exploring the capabilities of the transorbital image-guidance system to navigate to targets in the retrobulbar space. These phantoms provided a realistically proportioned working environment while mimicking the soft and hard tissues of the orbit, giving the surgeon various obstacles to direct optic nerve access. However, is was impractical to adapt these phantoms for this study. Implementation of collision detection requires the use of a force sensor attached to the optic nerve substitute, where all of the tension in the substitute runs through the sensor. In the skull

phantoms, the optic nerve substitute was anchored to the eyeball substitute on one end and the optic canal on the other, with no suitable point for attachment of the sensor.

We developed a new phantom for the purpose of this research. Since we planned to use CT imaging for image-guidance, all materials used in the surgical region were chosen to minimize beam scattering. A roughly conical volume of approximately 30 mL was excised from a solid plastic cylinder. This shape and volume were chosen to model the dimensions of a typical adult human orbit [96]. A thin hole was drilled through the plastic at the base of the conical volume to serve as the optic canal. The plastic cylinder was fastened to a wooden frame using plastic screws, with the center of the frame being empty to allow access to the optic canal. This frame was in turn affixed to a wooden base with plastic bolts. This configuration was utilized to allow for the attachment and detachment of an optic nerve substitute by simply unfastening the bolts. The orientation of the plastic cylinder was such that the orbital volume was similar to that of a human in the supine position, which is the expected position for orbital surgery. A total of 13 multimodal surface fiducial markers were attached onto and around the plastic cylinder to enable point-based registration.

The optic nerve substitute was a thin nylon cord with thickness of 3.5 mm, similar to that of a typical human adult. The cord was inserted through the plastic optic canal and knotted at one end to serve as an anchoring mechanism under tension. A raised platform was constructed around the orbit model to stabilize the other end of the cord. The platform featured a Transducer Techniques LSP-1 load cell, rigidly positioned directly above the center of the orbit model. In experimental configuration, the cord is tautly attached to the load cell with a known pre-load force. Contact with the endoscope imparts a strain on the cord, which is measured as a vertical force by the load cell. A basic representation of the phantom can be seen in Figure 25.

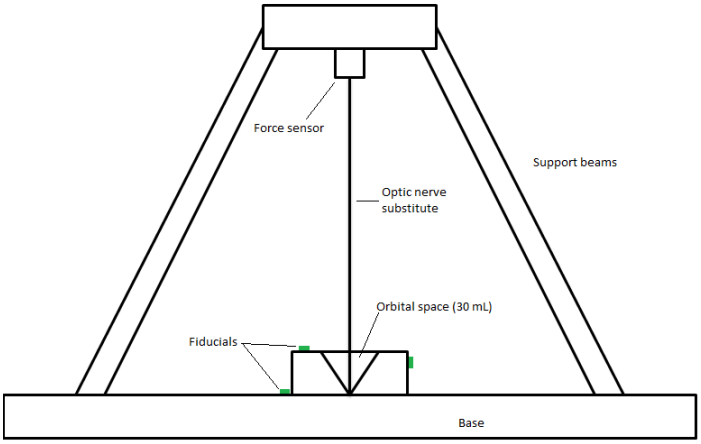

Figure 25. Orbital phantom with optic nerve force detection.

A total of 12 small colored dots were marked on the intraorbital section of the optic nerve substitute to represent targets. Three targets were placed on each of the four different sides of the nerve representing the coronal anatomical locations corresponding to a patient in the supine position with their right orbit closest to the surgeon. The coronal locations were designated lateral (closest to the side of the head), medial (closest to the nose), superior (closest to the brow ridge and top of the head), and inferior (closest to the cheek). The three targets in each set were marked at different orbital depths, namely anterior (closest to the eyeball), posterior (closest to the optic canal), and mid (in between the anterior and posterior). The targets were small enough to only be identifiable when the endoscope was directly pointed towards them in close proximity. The targets and their corresponding locations can be seen in Figure 26.

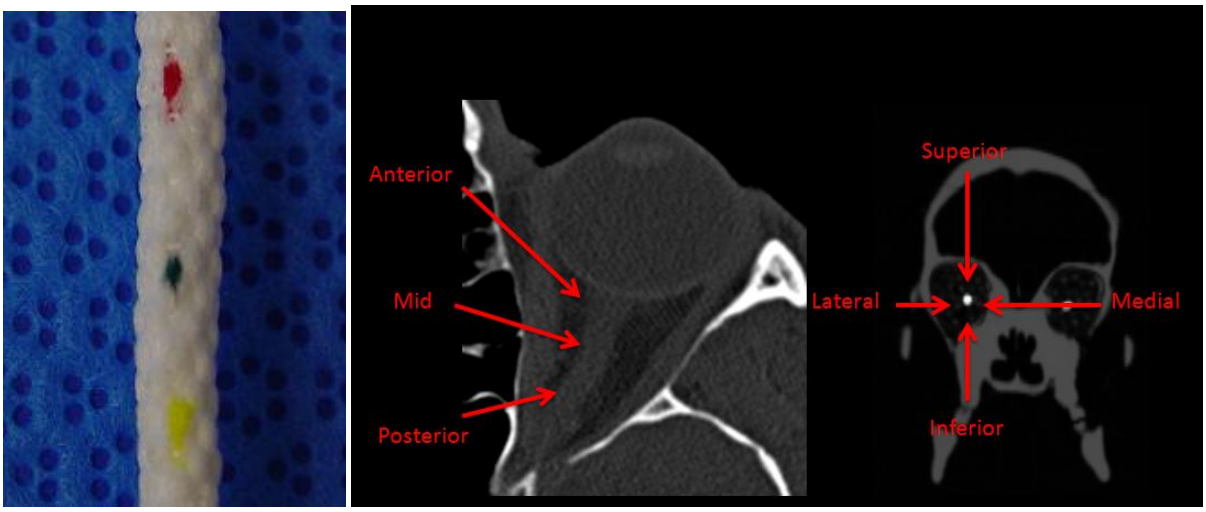

Figure 26. Orbital targets and locations. Targets marked on optic nerve substitute (left), intraorbital optic nerve segment locations (mid), and coronal anatomical locations (right)

Intraorbital fat was particularly difficult to simulate due to its distinct properties. The fat fills most of the orbital space that is not taken up by the optic nerve, muscles, or eyeball. It completely surrounds the retrobulbar portion of the optic nerve, is of a similar color to the nerve, and is the medium through which the endoscope traverses when targeting the nerve. It parts easily with light gas insufflation, tends to clump together, and does not typically stick to the lens of the endoscope. Various continuous substitute materials were experimented with and none matched these features adequately, with the most common issue being the tendency to stick to the endoscope lens, making visualization impossible. Small white polystyrene beads were chosen as a fat substitute, as they provided the necessary long range visual occlusion in the orbit but allowed for the clear short range endoscope imaging that would exist in fat under gas insufflation.

The orbital space of the model was filled with polystyrene beads and then sealed with thin plastic film, with a hole in the middle allowing for the passage of the optic nerve. A further four holes were added as incision points on the lateral, medial, superior, and inferior sides for orbital endoscopic insertion. The film served both to keep the polystyrene beads confined to the

orbital space during interventions while also simulating a realistic transorbital endoscopic surgery by restricting access to the region to a single entry port. Figure 27 is an image of the phantom with polystyrene beads filling the orbital space.

Figure 27. Orbital phantom with fat substitute

Force data acquisition

The output of the LSP-1 load cell was extremely low at the force magnitudes imparted by optic nerve collisions, and was thus connected to an Analog Devices AD620 instrumentation amplifier with a gain of 500 for initial signal amplification. The amplified signal was then sampled at 100 Hz by a National Instrument's data acquisition board and LabVIEW software. Force measurements during phantom procedures were recorded as a file with LabVIEW and subsequently processed with MathWork's MATLAB.

The load cell output was characterized by applying a series of known forces in the vertical direction, or along the primary axis of the optic nerve. In experimental configuration, the optic nerve substitute is preloaded with force to remove any slack and enable the detection of

small collision events. As such, output characterization was performed at various levels of preloaded force to determine whether or not the sensor was linearly sensitive. It was determined that the sensor was linearly sensitive over the expected preloaded force range, with a sensitivity of 0.8265 V / N.

Imaging

The phantom was imaged with high resolution CT, with pixel length and width of 0.3027 mm and voxel thickness of 0.335 mm. Only the orbital region of the phantom was imaged so as to maximize resolution in the surgical space and avoid scattering from the metal of the load cell. Prior to imaging, the optic nerve substitute was soaked in barium sulfate solution in order to appear bright in the CT scan and produce distinct region boundaries. Surface fiducial markers in the image volume were localized manually using ImageJ [97].

Segmentation of the optic nerve substitute was performed with ITK-SNAP's snake ROI tool using image edges to drive active contour evolution [98]. The resulting segmentation was saved a binary image mask for use in proximity-to-nerve calculations. This segmentation technique was suitable for the phantom due to the substantial contrast difference between barium-soaked optic nerve substitute and the surrounding space. In the case of a human subject, more advanced optic nerve segmentation methods would be necessary, such as those developed by Noble *et al*. [66] and Asman *et al*. [67].

Proximity awareness scheme

In the development of any surgical guidance system, it is important that new information is visualized without compromising the surgeon's attention from the intricacies of the

interventional task. Since the surgeon's primary visual focus during image guided surgery is on an image plane or the endoscope view, repetitively shifting focus to reference a proximity distance value could be unnecessarily distracting. With regards to optic nerve proximity, the exact distance value is not necessarily critical to know, so long as there is a constant awareness of a metric of safety.

For this research, surgeon awareness of the proximity of the endoscope to the optic nerve was implemented by three simple color-coded visual indicators. These indicators took the form of rectangular frames overlaid onto the endoscopic video, with the color of the frame indicating a discreet proximity state. A green frame indicated an endoscope-to-nerve distance equal or greater than 10 mm, a yellow frame indicated a distance between 3 and 10 mm, and a red frame indicated a distance equal or less than 3 mm. The color of these indicators could easily been seen by the surgeon using peripheral vision and allowed a constant awareness of endoscope proximity without requiring a change of primary visual focus. The endoscope-to-nerve distances were determined by generating a distance map based on potential registered endoscope tip positions with respect to a segmented optic nerve.

Distance calculation procedure

Optic nerve proximity detection fundamentally relies on a distance calculation between the current position of the distal end of the flexible endoscope and the closest point on the optic nerve. In this implementation, the current position of the endoscope was represented by the localized magnetic tracker. The optic nerve consisted of a segmented structure in a pre-operative, high resolution computed tomography (CT) scan. The proximity of the endoscope to the nerve was determined by registering the localized endoscope tip to image space and finding

the minimum distance between this point and all points consisting of the segmented optic nerve mask. Considering the number of optic nerve voxels in a high resolution CT image, this is a computationally expensive operation and not suitable for a real-time display application. Since imaging and segmentation are performed pre-operatively with no intra-operative updates, and the range of voxel locations of the registered endoscope tip is known, proximity values were calculated *a priori* and saved as a distance map with the same dimensions of the image volume.

Generation of the distance map was done in MathWorks' MATLAB. The distance map was initialized as an array with the same dimensions as the image volume. For each point in the distance map, the Euclidean distance between that point and each non-zero point in the optic nerve mask is calculated:

$$d = \sqrt{\left(v_x\left(x_{map} - x_{mask}\right)\right)^2 + \left(v_y\left(y_{map} - y_{mask}\right)\right)^2 + \left(v_z\left(z_{map} - z_{mask}\right)\right)^2}$$

where d is the distance, v are the voxel dimensions in millimeters, $(x,y,z)_{map}$ are the coordinates of the distance map point being determined, and $(x,y,z)_{mask}$ are the coordinates of the current member point of the optic nerve mask. The distance d is recorded in the distance map at the specified coordinates, and it is replaced is a subsequently calculated d for that point is smaller. The resulting array contains the metric distance between every 3D point in the phantom's orbital region and the closest point on the optic nerve substitute. To conserve memory, the distance map was saved as an array of 8-bit unsigned integers. At each update step in the ORION display, the current position of the endoscope is registered to image space and its proximity value is looked up in the distance map. This simple operation allows the image-guidance system to run in real

time without any computationally relevant additional update tasks, requiring only the memory keep the distance map loaded.

Experimental protocol

The experimental task was for a surgeon to navigate the endoscope to a specified region on the optic nerve and position the endoscope such that the corresponding target was clearly identifiable, simulating the delivery of therapy to a nerve segment. The target coronal locations were along the lateral, medial, superior, and inferior nerve sides, at anterior, posterior, and mid depths along the nerve's primary axis, for a total of 12 targets. At the start of each intervention, the surgeon was given the target's location description (lateral anterior, superior mid, etc.). The target's color was also known to the surgeon to ensure that they completed the procedure in the correct location, as navigation accuracy was not the focus of this experiment. All 12 distinct locations were targeted one in variable order, and then again for a total of 24 interventions. Display of the nerve proximity indicator was alternated through the course of the experiments, such that each distinct location trial was performed both with and without this additional visual information.

Experiments were performed by two ophthalmological surgeons, one who was well-acquainted with the image-guided transorbital endoscopy system, and one who was not. Target locations were set in the same order for each surgeon to allow for paired analysis. Sensor data acquisition was initialized upon a verbal indication of preparedness by the surgeon and terminated upon distinct visual confirmation of the target point.

Results

Screenshots of the image guidance system display can be seen in Figure 28. The left, center, and right images show screen captures when the endoscope was calculated to be more than 10 mm (green), between 3 mm and 10 mm (yellow), and less than 3 mm (red) away from the optic nerve, respectively. These locations can be visually confirmed by the registered endoscope position on the orthogonal CT imaging frames. The left and center images feature endoscope views that are occluded by the fat substitute, while the right image shows the target on the optic nerve substitute.

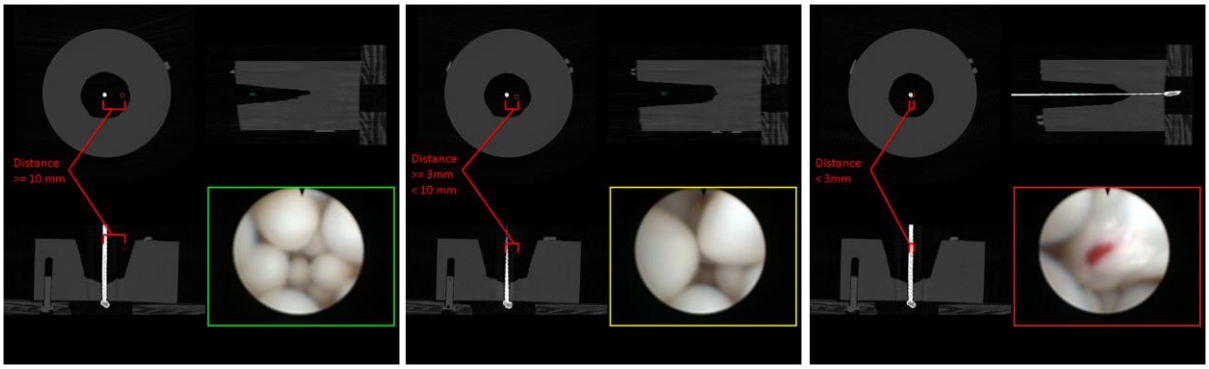

Figure 28. Image guidance system display screens for three different endoscope positions.

An example data acquisition from a single transorbital intervention can be seen in Figure 29. This data features several small deviations from the baseline voltage along with some very large ones. The small deviations are a result of the environmental vibrations inherent in the intervention as well as the movement of displaced polystyrene beads, while the large spikes are due to contact between the optic nerve substitute and the endoscope. This plot also demonstrates the value of the impulse measurement, as there is an extended duration of applied force during constant endoscope contact approximately between 1-6 seconds.

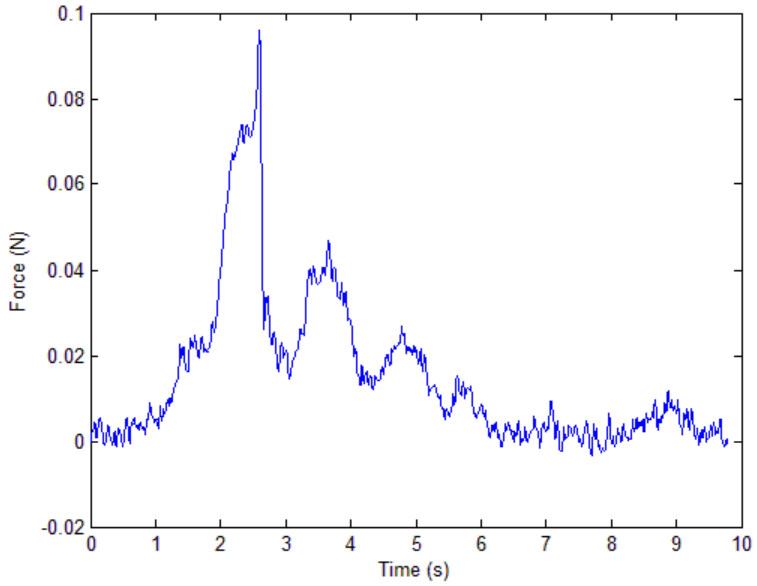

Figure 29. Example force sensor output for a transorbital endoscopic intervention.

Data for each intervention was processed to determine the following metrics: procedure time, peak force, number of collisions, and force applied over procedure time. Procedure time was simply the time-length of the data, while peak force was the maximum force applied during the intervention. A collision was defined as an instance where a net force change of 0.018 N was observed over time, as this was approximately double the range of noise. The force applied over the procedure time was determined as the integral of the data with respect to time, or the area under the force curve, and is used as a measurement of net optic nerve disturbance over the course of the intervention. This metric is in units of $N \cdot s$, and can be interpreted as the resulting impulse, or change in momentum, of the optic nerve along its primary axis.

The mean values for the metrics of time, peak force, number of collisions, and impulse are displayed in the Table 1:

Table 1. Mean force metrics.

Surgeon	Time (s)	Peak Force (N)	Collisions	Impulse (N · s)
Experienced	24.7	0.0755	2.96	0.225
Inexperienced	39.5	0.0502	4.04	0.394
Total	32.1	0.0628	3.50	0.310

There were several notable outliers when examining the metrics, corresponding to interventions where the surgeon was having considerable difficulty finding the target. As such, it is of interest to examine the median metric values as well, show in Table 2:

Table 2. Median force metrics.

Surgeon	Time (s)	Peak Force (N)	Collisions	Impulse (N · s)
Experienced	22.5	0.0385	2.00	0.087
Inexperienced	23.2	0.0426	3.00	0.140
Total	22.8	0.0408	2.00	0.110

The mean values for time, peak force, number of collisions, and impulse were compared between the experienced and inexperienced surgeon using the paired Wilcoxon signed-rank test, as the data was not normally distributed. It was found that the experienced surgeon exhibited a lower mean impulse than the inexperienced surgeon, with statistical significance at $p < 0.05$. The impulse measurements for each surgeon can be seen in Figure 30. The means for time, peak force, and number of collisions were not found to be significantly different at $p < 0.05$.

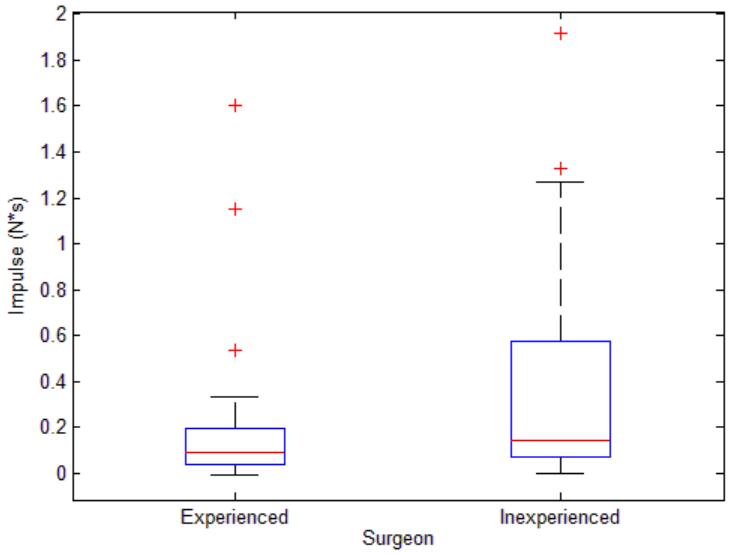

Figure 30. Boxplot showing impulse measurements for the experienced and inexperienced surgeons.

In order to investigate the effect of anatomical target location, metrics from each individual trial were labeled according to coronal location (lateral, medial, superior, inferior) and orbital depth (anterior, mid, posterior). These group means were analyzed with one-way ANOVA. It was found that impulse was significantly different with respect to orbital depth at $p < 0.02$, with mean impulse for targets in the posterior optic nerve location being substantially larger than the mid and posterior locations. This relationship can be seen in Figure 31. The remaining metric/group combinations were not found to be significantly different at $p < 0.05$.

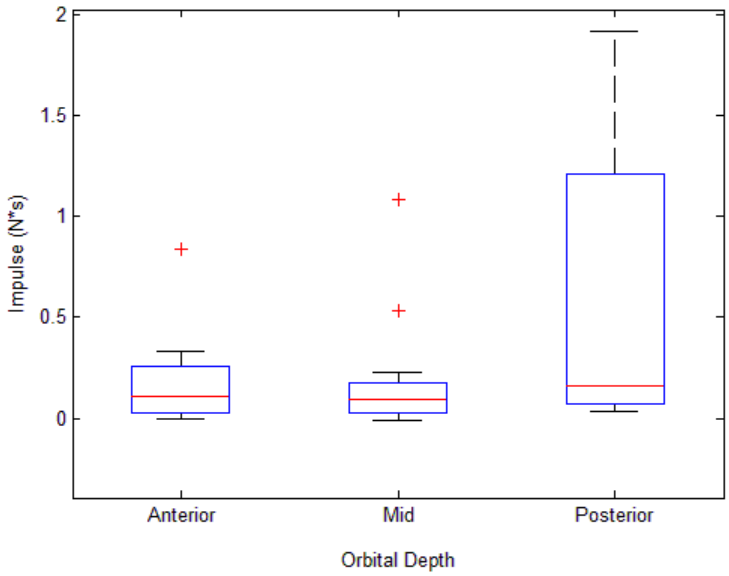

Figure 31. Boxplot showing impulse measurements for anterior, mid, and posterior target locations

The force metrics were also grouped according to the use of the proximity detection visualization element. The means for these two groups are displayed in Table 3:

Table 3. Mean force metrics with and without the use of proximity indicator.

	Time (s)	**Peak Force (N)**	**Collisions**	**Impulse (N · s)**
With indicator	32.3	0.0651	4.00	0.2995
Without indicator	31.9	0.0605	3.00	0.3202

The paired Wilcoxon signed-rank test indicated no significant difference between these two groups, for all metrics.

Discussion

The orbital phantom demonstrated sufficient force sensitivity to detect optic nerve collision events due to endoscopic intervention, as well as disturbance of the optic nerve

following a collision during persistent contact with the endoscope. The measurement of impulse was used a method to quantify the degree of this persistent contact and make an assessment of the total trauma imparted to the optic nerve during an intervention.

The significant difference in impulse between the experienced and inexperienced surgeon was expected, as the experienced surgeon was more familiar with the intricacies of endoscope orientation and took greater care when the endoscope was in close proximity to the nerve. The result indicates the value of practice and exposure to complicated navigation systems such as this. Utilization of the force detection phantom can be valuable as a training tool going forward, with operators attempting to perform procedures while minimizing observable metrics such as impulse.

The impulse measurement was also valuable in assessing the net optic nerve trauma inflicted with respect to the anatomical location of the target segment. One-way ANOVA did not find that coronal location (lateral, medial, superior, inferior) was a significant factor in applied force over the course of the procedure. The surgeons were typically able to adjust their method of handling the endoscope for each of these approach angles such that a sense of orientation was preserved. However, the depth of the target location along the optic nerve's primary axis was found to be a statistically significant factor in applied force, with the posterior location demonstrating a larger mean value when compared to the anterior and mid locations. This distinction is important, as it implies that the optimal target region for interventional therapy, such as drug delivery, is near the anterior and mid segments. Qualitatively, it was observed that when targeting the posterior region, the surgeon would often attempt to find the optic nerve first and then navigate the endoscope down along it, as opposed to planning a direct route from the entry point to the target point. It can be understood why this method would be prone to higher

impulse, as the continued presence of the endoscope in close proximity to the nerve would result in more cases of prolonged contact. Implementation of video augmentation as described by DeLisi *et al*. [91] has the potential to address this issue, as it enables a clear indicator of target location without relying on using the optic nerve as a visual landmark.

These experiments demonstrated no significant difference in measurable force metrics when the additional visual indication of optic nerve proximity was employed. A possible explanation for this result is that the proximity indicator was essentially redundant information. The position of the endoscope tip was already registered to the three orthogonal image planes and displayed in real-time, and already providing an indication of the spatial relationship between the tip and the optic nerve. This relationship was particularly clear in this experiment since the phantom was imaged in an ideal position, with the coronal location of the optic nerve changing very little and the full length of the nerve often appearing in the sagittal plane or transverse plane at initial endoscope entry, depending on anatomical target location. As the endoscope's proximity to the nerve was already sufficiently accounted for in these views, the additional visualization element of the colored frames was unnecessary. However, both surgeons indicated that proximity indicator made them more comfortable with the procedure and would prefer its inclusion if they using the system on a human subject.

The magnitudes of observed force can be used to indicate the physiological impact of transorbital endoscopic intervention on a human subject. However, determination of a possible damage threshold is dependent upon the mechanical properties of the optic nerve as described by previous studies [92, 93, 94, 95]. Unfortunately, there is no clear consensus. Bain and Meaney establish thresholds based on observed Lagrangian strain using guinea pig optic nerves, and postulate that the results are reflective of mammalians in general [95]. The average adult human

values for optic nerve intraorbital length and thickness are 25 mm and 3.5 mm, respectively [96]. Using these values, Bain and Meaney's optimal strain threshold of 0.21 translates to a change in optic nerve length of approximately 5 mm along the primary axis. A force threshold can be determined from this displacement if a value for the Young's modulus of the human optic nerve is known, using the equation:

$$F = \frac{E * A_0 * \Delta L}{L_0}$$

where L_0 is the initial length of the average adult human optic nerve, ΔL is the change in length due to an applied force and determined by a strain criteria, A_0 is the cross-sectional area of the average adult human optic nerve, E is the Young's modulus of the human optic nerve, and F is the force necessary to reach the strain criteria.

Sigal *et al*. has extensively modeled the optic nerve head to determine the relationships between intraocular pressure and physiological tissue damage, and employs a Young's modulus of 0.03 MPa for optic nerve tissue [92]. Using this modulus and accounting for their 0.0196 N of preload force [95], Bain and Meaney's strain criteria translates to a force threshold of 0.07732 N for optic nerve injury. Bellezza *et al*. use a Young's modulus of 0.055 MPa for axonal tissue [93], resulting in a force threshold of 0.12542 N for axonal injury using Bain and Meaney's strain criteria. Gennarelli *et al*. are more concerned with inflicting general injury than finding a specific threshold, but did determine that at a load force of 0.29420 N, the internal nerve structures became fully taut and susceptible to traumatic damage [94]. If Bain and Meaney's strain threshold is assumed to be equivalent with Gennarelli's force threshold, Gennarelli's observed Young's modulus of the optic nerve is 0.15 MPa.

When considering the output of the orbital phantom's force sensor with respect to proposed biological thresholds, it is necessary to scale the measured force values by the ratio of

the elastic moduli of the optic nerve substitute and the human optic nerve. As the optic nerve substitute has a higher elastic modulus (1.5 MPa) then the reported values for the human optic nerve, the sensor essentially behaves as a force amplifier, given that the observed strains are not drastically different for a collision event. This is a reasonable condition due to the method of slow endoscope insertion. In these experiments, surgeon tactile response to an anomaly, namely nerve contact, is dependent on the stiffness difference between the nerve substitute and the orbital fat substitute, a ratio that is higher than the difference in stiffness between the nerve substitute and a real human optic nerve under similar preload conditions. As such, the degree of nerve deflection dude to endoscope contact will be minimal, and the difference in strain between the phantom and reality will be more proportional to their differences in length. The maximum observed forces, scaled down with respect to the elastic moduli associated with the previously discussed possible damage thresholds can be seen in Figure 32.

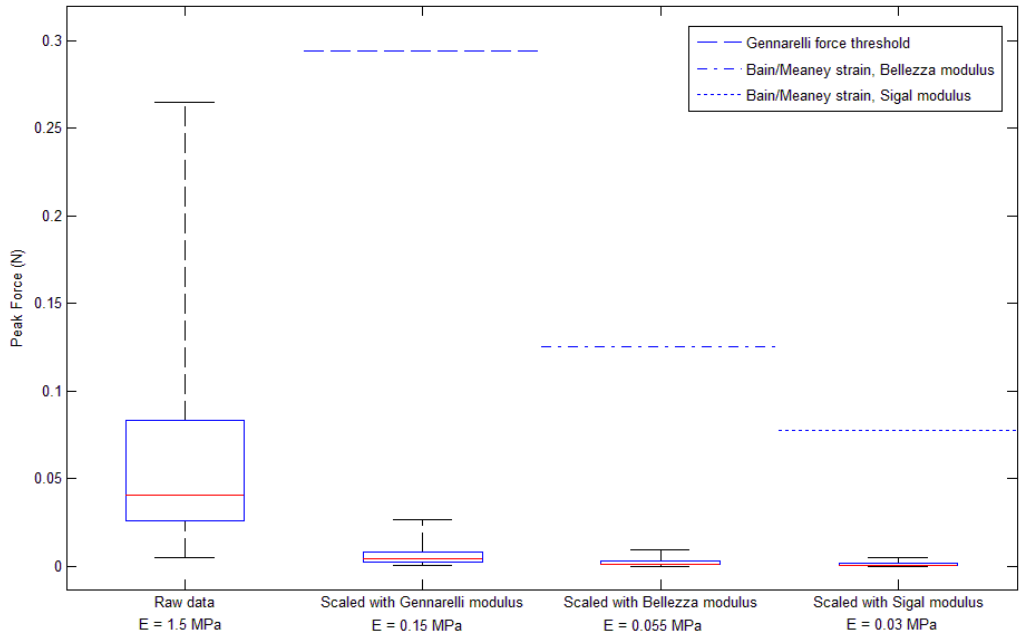

Figure 32. Boxplot of maximum force observed over all trials with reference to possible damage thresholds.

The maximum observed forces are well below the calculated possible damage thresholds for each proposed elastic modulus of the optic nerve, indicating minimal risk of injury.

At the other extreme, the phantom could be considered to be a strain suppressor if observed force is considered to demonstrate minimally difference with a realistic optic nerve collision event. Under these conditions, the observed strain experienced by the optic nerve substitute is scaled up with respect to the ratio of the phantom and human optic nerve elastic moduli. However, in this case, the moduli reported by Bellezza *et al*. [94] and Sigal *et al*. [93] are rendered inappropriate, as they pertain to isolated human axonal tissue and not the bundled arrangement of axons present in the optic nerve. Both the human optic nerve and the optic nerve substitute consist of bundled fibers, with applied strain manifesting substantially as unwinding and straightening of the internal structure. As such, modeling the tissue as isolated axons would generate unrealistically high strains under the observed endoscopic forces. However, the elastic modulus determined from unifying Gennarelli's force threshold [95] and Bain and Meaney's strain threshold [96] is more appropriate, as these experiments were performed using the entire optic nerve of live animals and thus more accurately represent the internal structure of the optic nerve. The scaled maximum strain values with respect to the Bain and Meaney strain threshold for damage can be seen in Figure 33.

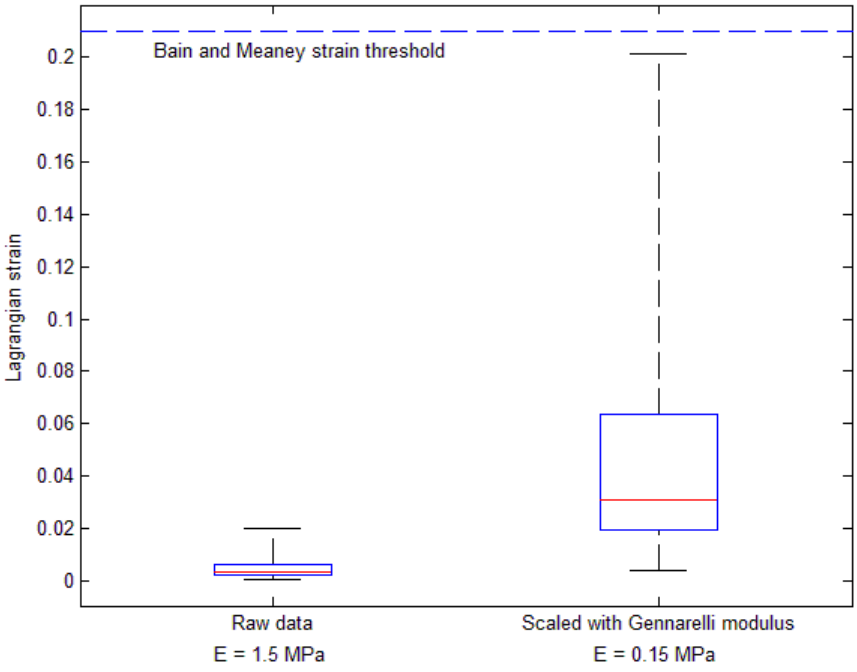

Figure 33. Boxplot of maximum strain observed over all trials with reference to possible damage threshold.

This figure demonstrates that while observed strains in the phantom will likely translate to higher strains *in vivo*, they are still under the damage threshold established by Bain and Meaney.

The implication of these results is that while transorbital procedures can produce optic nerve disturbances, the measured forces are below the possible damage thresholds established in the literature. The scaled data shown in Figure 32 and Figure 33 demonstrates that this is the case under the full range of possible phantom data interpretation, namely if the phantom is considered to be a pure force amplifier or a strain suppressor, with reality likely falling in between. More reliable statements could be made regarding injury force thresholds if biomechanical tissue properties of the human intraorbital optic nerve were available.

When considering applied force as a method of assessing optic nerve injury, it is also important to note that these experiments were performed with a taut optic nerve substitute. The

aforementioned injury thresholds were also generated with the optic nerve under fully taut conditions [94, 95]. The average healthy adult human has approximately 6 mm of slack optic nerve tissue within each orbit, which effectively compensates for many traumatic injury events [96]. Therefore, in order to induce a strain-based injury due to stretching of the optic nerve along its primary axis, an endoscope impact would have to first displace the nerve into a taut state and then pass an injury threshold. This displacement is a function of the shear modulus of the optic nerve and the surrounding intraorbital tissues. As such, it can be implied that the endoscope impacts characterized by this investigation may be even less potentially damaging when comparing the force metrics to injury thresholds. However, it can also be said that transorbital interventions may carry a higher risk of complications to patients who exhibit less intraorbital optic nerve slack, whether naturally or due to a pathological condition such as thyroid eye disease.

A limitation of the phantom model in measuring induced optic nerve forces involves the imperfect mechanical characteristics of the orbital fat substitute. This experiment measured the forces experienced by the optic nerve along its primary axis due to collisions with the endoscope, with the assumption being that these collisions would stretch the nerve and increase tension. In a human or animal model, contact between the endoscope and the nerve would be partially insulated by the orbital fat, absorbing some of the imparted energy and resulting in less tension in the nerve. The polystyrene beads were useful in providing visual occlusion while parting easily under endoscopic navigation, but exhibited these protective qualities due to a difference in effective shear modulus when compared to orbital fat tissue.

In order to examine the effect of the intraorbital fat, the polystyrene beads were replaced with porcine fat tissue, with temperature and fluid saturation levels similar to an *in vivo* scenario,

for a total of 6 experiments performed by the experienced surgeon. The resulting mean time, maximum force, number of collisions, and impulse were 25.4 s, 0.0122 N, 0.33, and 0.0683 N · s, respectively. These values are substantially lower than those reported in Table 1, with the means for maximum force and impulse being significantly different from their counterparts with $p < 0.05$ when the corresponding individual trials were analyzed with the paired Wilcoxon sign-rank test. This implies that the imparted force on the optic nerve due to transorbital endoscopic interventions is lower than the previous data suggests, which becomes particularly relevant when comparing the maximum force values to the three established injury thresholds. However, it should be noted that the mechanical characteristics of the porcine fat tissue rapidly changed with time as it cooled down and was exposed to air, with noticeable change in consistency what could have somewhat exaggerated the protective effects of intraorbital fat. The volatility and time-consuming nature of handling the porcine fat tissue were the major reasons why it was not used for the primary experiments.

Conclusions

Transorbital image guided surgery has the potential to introduce new forms of therapy to the optic nerve. Any interventional procedure to the optic nerve must attempt to minimize unnecessary tissue trauma that may result in vision loss. This research has investigated the effect of transorbital interventions on the optic nerve using a phantom model with force detection capability, specifically measuring procedure time, maximum force applied, number of endoscope collisions with the nerve, and impulse.

The capability of measuring forces in a physiologically pertinent range in a phantom model is valuable in characterizing the quality of a procedure for training purposes and

investigating the usefulness of possible guidance enhancements. The significant difference between applied impulse between an experienced and inexperienced surgeon highlight the need for training with the system, while the lack of strong correlation between the use of additional endoscope/nerve proximity visualization implies that this spatial relationship is already sufficiently accounted for in the existing system or that the implementation of the visualization was simply ineffective. Furthermore, the significantly higher impulse values measured for posterior target locations when compared to anterior and mid target locations could provide valuable information for procedure planning.

Definitive determination of optic nerve injury as a result of transorbital procedures was limited due to the lack of consensus with regard to human optic nerve tissue mechanics. However, optic nerve tissue models from multiple studies were used to produce different force and strain thresholds for injury, with the phantom experiments demonstrating no threshold violations. As a clear force threshold for injury would be quite useful for system evaluation and training purposes, a more complete biomechanical characterization of the intraorbital segment of the optic nerve is desirable. A future contribution on this topic would be valuable not only to this research, but to the cited investigations regarding diffuse axonal injury and intraocular pressure-related tissue damage. Even if the existing optic nerve tissue models are correct, the observed forces and possibility of optic nerve injury are likely to be substantially smaller *in-vivo* due to the protective qualities of intraorbital fat and presence of optic nerve slack. As a result of these realities, this investigation provides an encouraging characterization of the transorbital endoscopic image-guidance system with respect to patient safety.

Acknowledgments

The authors would like to thank Zach Meszoely for his assistance in constructing the phantom, the Vanderbilt University Medical Center CT staff for their help in obtaining CT scans of the phantom, and the surgeons who volunteered their time to test the image-guidance system. This work was supported in part by the Research to Prevent Blindness Physician Scientist Award, the Unrestricted Grant from Research to Prevent Blindness to the Vanderbilt Eye Institute, and the National Institutes of Health under Grant R21 RR025806.

CHAPTER V

CONCLUSIONS AND FUTURE WORK

Research Summary and Contributions

Open angle glaucoma is a widespread optic neuropathy that is the most common cause of blindness in developed nations. Current glaucoma treatment is suboptimal because it does not treat the disease at the fundamental retinal ganglion cell level. Neuroprotective agents such as brimonidine are being developed that theoretically can halt the progression of glaucoma by restricting retinal ganglion cell apoptosis and thus preserving neural function. Topical neuroprotective medication is inadequate due to extremely limited effective dose to the retinal cell bodies in the posterior globe and minimal drug propagation past the optic disk to the axons. Therapeutic efficacy can be increased by directly applying the neuroprotective agent to the optic nerve on a regular basis. The difficult anatomical location of the optic nerve within the retrobulbar space and requirement for therapeutic repeatability necessitates the development of a sophisticated drug delivery system.

An image-guided flexible endoscope is capable of navigating to the retrobulbar space and depositing a drug payload directly to the optic nerve, as well as other intraorbital therapeutic tasks. The system utilizes high resolution pre-operative CT images, magnetic localization, and point-based rigid registration to facilitate guidance. This research has developed enhancements in guidance and visualization for the system, while validating its capabilities and performance in animal and phantom models.

Chapter II described a series of pig experiments utilizing the system for target localization in the orbit, measuring identification accuracy and procedure time. A model for performing targeted transorbital interventions in pigs was developed using microspherical bulbs filled with contrast agent. These *in-vivo* experiments demonstrated the capabilities of the image-guided system to navigate to a specified location within the orbit and make a definitive target identification, under real physiological conditions. This study also served as an initial investigation into the value of enhancing endoscopic navigation by overlaying target location obtained from pre-operative imaging using 3D/2D registration. The cases performed with the enhanced endoscope exhibited significantly shorter procedure times when compared to the cases performed with standard settings. This work demonstrated that task-oriented image guided transorbital endoscopy was possible in live tissue despite the anatomical challenges, while also making an initial effort to improve procedure quality by incorporating video augmentation.

Chapter III expanded upon this effort in a series of orbital phantom experiments. Enhanced endoscopy in the form of augmented video was fully implemented into the image-guidance system using a more rigorous calibration and camera lens distortion correction. The effect of augmented video in practice was explored across a wide range of surgeons in a series of phantom model experiments. These skull phantoms were constructed with various soft tissue substitutes and contained multiple targets within each orbit, with the correct target appearing bright on the pre-operative imaging volume. Surgeons were required to navigate to the target and identify it by color, with trials alternating the use of video augmentation. Procedure times were significantly lower when using video augmentation, while accuracy was also observed to increase. The results of this controlled study demonstrated that procedure quality, as represented

by procedure time, was significantly improved upon by using video augmentation. This work makes a clear case for the inclusion of video augmentation in transorbital endoscopy.

Chapter IV assesses the concern of procedure safety by characterizing the physical forces experienced by the optic nerve during an endoscopic intervention. A phantom was developed to measure force along the primary axis of an optic nerve substitute during an interventional task in the orbit. The resulting data sets consisted of procedure time, maximum force, number of collisions, and impulse. These were analyzed with respect to surgeon experience, anatomical target location, and use or lack of use of additional endoscope/nerve proximity visualization, while the maximum forces were also compared to a series of possible injury thresholds generated using biomechanical optic nerve properties found in the literature. It was found that impulse was dependent on surgeon experience and anatomical target location, with observations being significantly larger in the cases of surgeon inexperience and the posterior nerve region. These results have practical value when training surgeons to utilize the system and when planning transorbital intervention routes. Possible injury rate quantification was difficult due to conflicting models of intraorbital optic nerve biomechanics, yet the measured forces and strains did not violate damage thresholds determined from the literature. Furthermore, this study did not take into account the protective qualities of intraorbital fat and the presence of intraorbital optic nerve slack, which would substantially reduce the degree of applied strain on the nerve due to an impact event with the endoscope during a procedure. The resulting worst-case scenario nerve injury rates indicate that transorbital endoscopy is reasonably safe when taking into account realistic conditions.

These investigations have strongly advocated the inclusion of video augmentation into image-guided transorbital endoscopy. Shorter procedure times and improved target identification

accuracy are indicators of an improved minimally-invasive quality, which in turn translates to superior patient outcomes. Furthemore, an optimistic assessment of the safety of transorbital endoscopic interventions is justified in light of the observed forces and the limitations of the phantom model. These contributions have advanced the case for application of image guided transorbital endoscopy to humans.

Future Work

There remains a need to fully assess the system's capabilities with regard to its initial purpose in treating glaucoma, namely by characterizing complete therapeutic drug delivery in live animal cases. These studies would involve navigating the endoscope to the optic nerve of an animal, delivered a quantity of nanoparticle-encapsulated neuroprotective drugs, allowing time for drug uptake into the optic nerve, and testing the excised nerve for drug concentration following animal sacrifice. The results would indicate the rate of drug uptake by the optic nerve unique to this combined delivery system and allow for comparison with existing techniques. Preparation for these studies are currently in advanced stages, with initial experiments expected to begin imminently.

This research has also highlighted the lack of available information regarding the biomechanical properties of the intraorbital segment of the human optic nerve. Knowledge of these properties would useful for understanding possible injuries to the nerve due to endoscopic intervention, while also contributing to other fields such as the study of diffuse axonal injury and traumatic optic neuropathy. Biomechanical characterization of the optic nerve could be performed using tissue obtained from enucleations or warm cadavers. Furthermore,

comprehensive computer models of orbital soft tissue, such as described by Cirovic *et al*. [99], could also be used to determine the physiological effect of transorbital endoscopy.

APPENDIX

Biography

Michael P. DeLisi received the B.S. degree in electrical engineering from the Cooper Union, New York City, New York, in 2006 and the M. S. degree in biomedical engineering from Vanderbilt University, Nashville, Tennessee, in 2010. He completed the Ph.D. degree in biomedical engineering from Vanderbilt University, Nashville, Tennessee, in 2014.

From 2006 to 2008, he was a Teaching Assistant, providing instruction primarily in biomedical instrumentation. Since 2008, he has been a Research Assistant at Vanderbilt University, Nashville, Tennessee. His research interest includes image-guided surgery, endoscopy, technology-guide therapy in ophthalmology, and medical systems validation.

Mr. DeLisi's awards and honors include the Graduate Student Teaching Award from Vanderbilt University in 2008, the Scientist in the Classroom Partnership Program Fellowship in 2012, and the SPIE Medical Imaging Poster Award in 2013.

REFERENCES

[1] S. Resnikoff, D. Pascoloni, D. Etaya'ale, I. Kocu, R. Pararajasegaram, G. P. Pokharel and S. P. Mariotti, "Global Data on Visual Impairment in the Year 2002," *Bulletin of the World Health Organization,* vol. 82, pp. 844-851, 2004.

[2] G. Forbes, D. G. Gehring, C. A. Gorman, M. D. Brennan and I. T. Jackson, "Volume measurements of normal orbital structures by computed tomographic analysis," *American Journal of Roentgenology,* vol. 145, pp. 149-154, 1985.

[3] J. L. Wilkinson, Neuroanatomy for Medical Students, Oxford: Butterworth-Heinemann, 1998.

[4] N. Osborne, G. Chidlow, C. J. Layton, J. P. M. Wood, R. J. Casson and J. Melena, "Optic Nerve and Neuroprotection Strategies," *Eye,* vol. 18, pp. 1075-1084, 3004.

[5] F. B. Walsh, W. F. Hoyt, N. R. Miller, N. J. Newman, V. Biousse and J. B. Kerrison, Walsh & Hoyt's Clinical Neuro-Ophthalmology, Lippincott Williams & Wilkins, 2005.

[6] J. J. Kanski, Clinical Ophthalmology, Oxford: Butterworth-Heinemann, 1994.

[7] H. A. Quigley and A. T. Broman, "The Number of People with Glaucoma Worldwide in 2010 and 2020," *British Journal of Ophthalmology,* vol. 90, pp. 262-267, 2006.

[8] Y. H. Kwon, J. H. Fingert, M. H. Kuehn and W. L. M. Alward, "Primary Open-Angle Glaucoma," *New England Journal of Medicine,* vol. 360, pp. 1113-1124, 2009.

[9] A. Heijl, M. C. Leske, B. Bengtsson, L. Hyman, B. Bengtsson and M. Hussein, "Reduction of Intraocular Pressure and Glaucoma Progression: Results from the Early Manifest Glaucoma Trial," *Archives of Ophthalmology,* vol. 120, no. 10, pp. 1268-1279, 2002.

[10] J. C. Tsai, C. A. McClure, S. E. Ramos, D. G. Schlundt and J. W. Pichert, "Compliance Barriers in Glaucoma: A Systemic Classification," *Journal of Glaucoma,* vol. 12, no. 5, pp. 393-398, 2003.

[11] B. L. Nordstrom, D. S. Friedman, E. Mozaffari, H. A. Quigley and A. M. Walker, "Persistence and Adherence with Topical Glaucoma Therapy," *American Journal of Ophthalmology,* vol. 140, no. 4, pp. 598.e1-598.e11, 2005.

[12] D. H. Geroski and H. F. Edelhauser, "Drug Delivery for Posterior Segment Eye Disease," *Investigative Ophthalmology and Visual Science,* vol. 41, no. 5, pp. 961-964, 2000.

[13] G. Velez and S. M. Whitcup, "New Developments in Sustained Release Drug Delivery for the Treatment of Intraocular Disease," *British Journal of Ophthalmology,* vol. 83, no. 11, pp. 1225-1229, 1999.

[14] K. M. Sampat and S. J. Garg, "Complications of Intravitreal Injections," *Current Opinion in Ophthalmology,* vol. 21, no. 3, pp. 178-183, 2010.

[15] M. E. Myles, D. M. Neumann and J. M. Hill, "Recent Progress in Ocular Drug Delivery for Posterior Segment Disease: Emphasis on Transscleral Iontophoresis," *Advanced Drug Delivery Reviews,* vol. 57, no. 14, pp. 2063-2079, 2005.

[16] S. J. McKinnon, L. D. Goldberg, P. Peeples, J. G. Walt and T. J. Bramley, "Current Management of Glaucoma and the Need for Complete Therapy," *American Journal of Managed Care,* vol. 14, pp. S20-S27, 2008.

[17] J. Flammer and M. Mozaffarieh, "What is the Present Pathogenetic Concept of Glaucomatous Optic Neuropathy?," *Survey of Ophthalmology,* vol. 52, no. 6, pp. S162-S173, 2007.

[18] H. Resch, G. Garhofer, G. Fuchsjäger-Mayrl, A. Hommer and L. Schmetterer, "Endothelial Dysfunction in Glaucoma," *Acta Ophthalmologica,* vol. 87, no. 1, pp. 4-12, 2009.

[19] J. P. Vrabec and L. A. Levin, "The Neurobiology of Cell Death in Glaucoma," *Eye,* vol. 21, pp. S11-S14, 2007.

[20] M. Mozaffarieh, M. C. Grieshaber and J. Flammer, "Oxygen and Blood Flow: Players in the Pathogenesis of Glaucoma," *Molecular Vision,* vol. 14, pp. 224-233, 2008.

[21] A. J. Weber, C. D. Harman and S. Viswanathan, "Effects of Optic Nerve Injury, Glaucoma, and Neuroprotection on the Survival, Structure, and Function of Ganglion Cells in the Mammalian Retina," *Journal of Physiology,* vol. 586, pp. 4293-4400, 2008.

[22] A. T. E. Hartwick, "Beyond Intraocular Pressure: Neuroprotective Strategies for Future Glaucoma Therapy," *Optometry & Visual Science,* vol. 78, no. 2, pp. 85-94, 2001.

[23] L. A. Levin, "Retinal Ganglion Cells and Neuroprotection for Glaucoma," *Survey of Ophthalmology,* vol. 48, no. 2, pp. S21-S24, 2003.

[24] L. A. Levin and P. Peeples, "History of Neuroprotection and Rationale as a Therapy for Glaucoma," *American Journal of Managed Care,* vol. 14, pp. S11-S14, 2008.

[25] A.-C. Bessero and P. Clarke, "Neuroprotection for Optic Nerve Disorders," *Current Opinion in Ophthalmology,* vol. 23, no. 1, pp. 10-15, 2010.

[26] H. V. Danesh-Meyer, "Neuroprotection in Glaucoma: Recent and Future Directions," *Current Opinion in Ophthalmology,* vol. 22, no. 2, pp. 78-86, 2011.

[27] Allergan, Inc, "Allergan Reports Fourth Quarter Operating Results [press release]," 30 January 2008. [Online]. Available: agn360.client.shareholder.com/releasedetail.cfm?ReleaseID=290764. [Accessed 1

November 2011].

[28] M. Saylor, L. K. McLoon, A. R. Harrison and M. S. Lee, "Experimental and Clinical Evidence for Brimonidine as an Optic Nerve and Retinal Neuroprotective Agent: An Evidence-Based Review," *Archives of Ophthalmology,* vol. 127, no. 4, pp. 402-406, 2009.

[29] W. Lambert, L. Ruiz, S. Crish, L. Wheeler and D. Calkins, "Brimonidine Prevents Axonal and Somatic Degeneration of Retinal Ganglion Cell Neurons," *Molecular Neurodegeneration,* vol. 6, p. 4, 2011.

[30] H. E. Fazzone, M. J. Kupersmith and J. Leibmann, "Does Topical Brimonidine Tartrate Help NAION?," *British Journal of Ophthalmology,* vol. 87, pp. 1193-1194, 2003.

[31] B. Wilhelm, H. Ludtke and H. Wilhelm, "Efficacy and Tolerability of 0.2% Brimonidine Tartrate for the Treatment of Acute Non-Arteritic Anterior Ischemic Optic Neuropathy (NAION): A 3-Month, Double-Masked, Randomised, Placebo-Controlled Trial," *Graefe's Archive for Clinical and Experimental Ophthalmology,* vol. 244, no. 5, pp. 551-558, 2006.

[32] N. J. Newman, V. Biousse, R. David, M. T. Bhatti, S. R. Hamilton, B. K. Farris, R. L. Lesser, S. A. Newman, R. E. Turbin, K. Chen and R. P. Keaney, "Prophylaxis for Second Eye Involvement in Leber Hereditary Optic Neuropathy: An Open-Labeled, Nonrandomized Multicenter Trial of Topical Brimonidine Purite," *American Journal of Ophthalmology,* vol. 140, pp. 407-415, 2005.

[33] T. Krupin, J. M. Liebmann, D. S. Greenfield, R. Ritch and S. Gardiner, "A Randomized Trial of Brimonidine Versus Timolol in Preserving Visual Function: Results from the Low-Pressure Glaucoma Treatment Study," *American Journal of Ophthalmology,* vol. 151, pp. 671-681, 2011.

[34] F. B. Kalapesi, M. A. Hill and M. T. Coroneo, "Neuroprotective Agent Brimonidine: A Toxicity Study (Abstract)," *Investigative Ophthalmology & Visual Science,* 2003.

[35] S. J. Fudemberg, C. Batiste and L. J. Katz, "Efficacy, Safety, and Current Applications of Brimonidine," *Expert Opinion on Drug Safety,* vol. 7, no. 6, pp. 795-799, 2008.

[36] A. E. van der Ende, E. J. Kravitz and E. Harth, "Approach to Formation of Multifunctional Polyester Particles in Controlled Nanoscopic Dimensions," *Journal of American Chemical Society,* vol. 130, no. 27, pp. 8706-8713, 2008.

[37] K. Grove, J. Dobish, E. Harth, M.-C. Ingram, R. L. Galloway and L. A. Mawn, "Trans-Meningial Drug Delivery to the Optic Nerve Ganglion Cell Axons Using a Nanoparticle Drug Delivery System," *Experimental Eye Research,* vol. 118, pp. 42-45, 2014.

[38] J. Rootman, B. Stewart and R. A. Goldberg, Orbital Surgery: A Conceptual Approach, Philadelphia: Raven Publishers, 1995.

[39] R. W. Pelton and B. Patel, "Superomedial Lid Crease Approach to the Medial Intraconal Space: A New Technique for Access to the Optic Nerve and Central Space," *Ophthalmic Plastic and Reconstructive Surgery,* vol. 17, no. 4, pp. 241-253, 2001.

[40] M. Karaki, R. Kobayashi and N. Mori, "Removal of an Orbital Apex Hemangioma Using an Endoscopic Transethmoidal Approach: Technical Note," *Neurosurgery,* vol. 59, no. 1, pp. ONS-E159-ONS-E160, 2006.

[41] T. Peters and K. Cleary, Image Guided Interventions, New York: Springer, 2008.

[42] N. C. Atuegwu and R. L. Galloway, "Volumetric Characterization of the Aurora Magnetic Tracker System for Image-Guided Transorbital Endoscopic Procedures," *Physics in Medicine and Biology,* vol. 53, no. 16, pp. 4355-4368, 2008.

[43] J. B. A. Maintz and M. A. Viergever, "A Survey of Medical Image Registration," *Medical Image Analysis,* vol. 2, no. 1, pp. 1-36, 1998.

[44] C. R. Maurer, J. M. Fitzpatrick, M. Y. Wang, R. L. Galloway, R. J. Maciunas and G. S. Allen, "Registration of Head Volume Images Using Implantable Fiducial Markers," *IEEE Transactions on Medical Imaging,* vol. 16, no. 4, pp. 447-462, 1997.

[45] G. H. Barnett, D. W. Miller and J. Weisenberger, "Frameless Stereotaxy with Scalp-Applied Fiducial Markers for Brain Biopsy Procedures: Experience in 218 Cases," *Journal of Neurosurgery,* vol. 91, pp. 569-576, 1999.

[46] J. M. Fitzpatrick, J. B. West and C. R. Maurer, "Predicting Error in Rigid-Body Point-Based Registration," *IEEE Transactions on Medical Imaging,* vol. 17, no. 5, pp. 694-702, 1998.

[47] R. L. Galloway, "The Process and Development of Image-Guided Procedures," *Annual Review of Biomedical Engineering,* vol. 3, pp. 83-108, 2001.

[48] E. Abel, W. Xi and P. White, "Methods for Removing Glare in Digital Endoscope Images," *Surgical Endoscopy,* vol. 25, no. 12, pp. 3898-3905, 2011.

[49] A. Gottlieb, J. Sprung, X.-M. Zheng and M. Gagner, "Massive Subcutaneous Emphysema and Severe Hypercarbia in a Patient During Endoscopic Transcervical Parathyroidectomy Using Carbon Dioxide Insufflation," *Anesthesia and Analgesia,* vol. 84, no. 5, pp. 1154-1156, 1997.

[50] R. L. Marshall, P. J. R. Jebson, I. T. Davie and D. B. Scott, "Circulatory Effects of Carbon Dioxide Insufflation of the Peritoneal Cavity for Laparoscopy," *British Journal of Anaesthesia,* vol. 44, no. 7, pp. 680-684, 1972.

[51] P. Yau, D. I. Watson, T. Lafullarde and G. G. Jamieson, "Experimental Study of the Effect

of Embolism of Different Laparoscopy Insufflation Gases," *Journal of Laparoendoscopic and Advanced Surgical Techniques,* vol. 10, no. 4, pp. 211-216, 2000.

[52] R. J. Shah, J. H. Shen and K. M. Joos, "Endoscopic Free Electron Laser Technique Development for Minimally Invasive Optic Nerve Sheath Fenestration," *Lasers in Surgery and Medicine,* vol. 36, pp. 589-596, 2007.

[53] M. J. Mack, "Minimally Invasive and Robotic Surgery," *Journal of the American Medical Association,* vol. 285, no. 5, pp. 568-572, 2001.

[54] O. Ukimura, "Image-Guided Surgery in Minimally Invasive Urology," *Current Opinion in Urology,* vol. 20, no. 2, pp. 136-140, 2010.

[55] T. G. John, J. D. Greig, J. L. Crosbie, W. F. Miles and O. J. Garden, "Superior Staging of Liver Tumors with Laparoscopy and Laparoscopic Ultrasound," *Annals of Surgery,* vol. 220, no. 6, pp. 711-719, 1994.

[56] M. Hünerbein, B. Rau and P. M. Schlag, "Laparoscopy and Laparoscopic Ultrasound for Staging of Upper Gastrointestinal Tumours," *European Journal of Surgical Oncology,* vol. 21, no. 1, pp. 50-55, 1995.

[57] A. Cuschieri, J. Bracken and L. Boni, "Initial Experience with Laparoscopic Ultrasound-Guided Radiofrequency Thermal Ablation of Hepatic Tumours," *Endoscopy,* vol. 31, no. 4, pp. 318-321, 1999.

[58] D. B. Kynor, E. M. Friets, D. A. Knaus and J. Bieszczad, "Tissue Localization Using Endoscopic Laser Projection for Image-Guided Sugery," *Proceedings of the SPIE Medical Imaging,* vol. 5744, 2005.

[59] T. P. Rauth, P. Q. Bao, R. L. Galloway, J. Bieszczad, E. M. Friets, D. A. Knaus, D. B.

Kynor and A. J. Herline, "Laparoscopic Surface Scanning and Subsurface Targeting: Implications for Image-Guided Laparoscopic Liver Surgery," *Surgery,* vol. 142, no. 2, pp. 207-214, 2007.

[60] N. V. Vasilyev, P. M. Novotny, J. F. Martinez, H. Loyola, I. S. Salgo, R. D. Howe and P. J. del Nido, "Stereoscopic Vision Display Technology in Real-Time Three-Dimensional Echocardiography-Guided Intracardiac Beating-Heart Surgery," *Journal of Thoracic and Cardiovascular Surgery,* vol. 135, no. 6, pp. 1334-1341, 2008.

[61] L. A. Mawn, J.-H. Shen, D. R. Jordan and K. M. Joos, "Development of an Orbital Endoscope for Use with the Free Electron Laser," *Ophthalmic Plastic and Reconstructive Surgery,* vol. 20, no. 2, pp. 150-157, 2004.

[62] N. C. Atuegwu, L. A. Mawn and R. L. Galloway, "Transorbital Endoscopic Image Guidance," *Proceedings of the 29th Annual IEEE Engineering in Medicine and Biology Society Conference,* pp. 4663-4666, 2007.

[63] J. D. Stefansic, W. A. Bass, S. L. Hartmann, R. A. Beasley, T. K. Sinha, D. M. Cash, A. J. Herline and R. L. Galloway, "Design and Implementation of a PC-Based Image-Guided Surgical System," *Computer Methods and Programs in Biomedicine,* vol. 69, no. 3, pp. 211-224, 2002.

[64] N. C. Atuegwu and R. L. Galloway, "Sensitivity Analysis of Fiducial Placement on Transorbital Target Registration Error," *International Journal of Computer Assisted Radiology and Surgery,* vol. 2, no. 6, pp. 397-404, 2008.

[65] N. I. Regensburg, P. H. B. Kok, F. W. Zonneveld, L. Baldeschi, P. Saeed, W. M. Wiersinga and M. P. Mourits, "A New and Validated CT-Based Method for the Calculation of Orbital

Soft Tissue Volumes," *Investigative Ophthalmology and Visual Science,* vol. 49, no. 5, pp. 1758-1762, 2008.

[66] J. H. Noble and B. M. Dawant, "Automatic Segmentation of the Optic Nerves and Chiasm in CT and MR Using the Atlas-Navigated Optimal Medial Axis and Deformable-Model Algorithm," in *SPIE*, 2009.

[67] A. J. Asman, M. P. DeLisi, L. A. Mawn, R. L. Galloway and B. A. Landman, "Robust Non-Local Multi-Atlas Segmentation of the Optic Nerve," in *SPIE Medical Imaging*, Orlando, 2013.

[68] T. Sielhorst, M. Feuerstein and N. Navab, "Advanced Medical Displays: A Literature Review of Augmented Reality," *Journal of Display Technology,* vol. 4, no. 4, pp. 451-467, 2008.

[69] J. D. Stefansic, A. J. Herline, Y. Shyr, W. C. Chapman, J. M. Fitzpatrick, B. M. Dawant and R. L. Galloway, "Registration of Physical Space to Laparoscopic Image Space for Use in Minimally Invasive Hepatic Surgery," *IEEE Transactions on Medical Imaging,* vol. 19, no. 10, pp. 1012-1023, 2000.

[70] Y. I. Adbel-Aziz and H. M. Karara, "Direct Linear Transformation from Comparator Coordinates into Object Space Coordinates in Close Range Photogrammetry," *Proceedings of the Symposium on Close Range Photogrammetry,* pp. 2-28, 1971.

[71] K. Balakrishnan and K. S. Moe, "Applications and Outcomes of Orbital and Transorbital Endoscopic Surgery," *Otolaryngology--Head and Neck Surgery,* vol. 144, no. 5, pp. 815-820, 2011.

[72] M.-C. Ingram, N. Atuegwu, L. A. Mawn and R. L. Galloway, "Transorbital Therapy

Delivery - Phantom Testing," in *SPIE,* 2011.

[73] W. Freysinger, A. Gunkel and W. Thumfart, "Image-Guided Endoscopic ENT Surgery," *Eur. Archives of Otorhinolaryngology,* vol. 254, no. 7, pp. 343-346, 1997.

[74] T. Kawamata, H. Iseki, T. Shibasaki and T. Hori, "Endoscopic Augmented Reality Navigation System for Endonasal Transsphenoidal Surgery to Treat Pituitary Tumors: Technical Note," *Neurosurgery,* vol. 50, no. 6, pp. 1393-1397, 2002.

[75] R. Lapeer, M. S. Chen, G. Gonzalez, A. Linney and G. Alusi, "Image-Enhanced Surgical Navigation for Endoscopic Sinus Surgery: Evaluating Calibration, Registration, and Tracking," *International Journal of Medical Robotics and Computer Assisted Surgery*, vol. 4, no. 1, pp. 32-45, 2008.

[76] W. P. Liu, D. J. Mirota, A. Uneria, Y. Otake, G. Hager, D. D. Reh, M. Ishii, G. L. Gallia and J. H. Siewerdsen, "A Clinical Pilot Study of a Modular Video-CT Augmentation System for Image-Guided Skull Base Surgery," *Proceedings of the SPIE Medical Imaging,* vol. 8316, 2012.

[77] J.-Y. Bouguet, "Camera Caliberation Toolbox for Matlab," [Online]. Available: http://www.vision.caltech.edu/bouguetj/calib_doc/index.html.

[78] Z. Zhang, "Flexible Camera Calibration by Viewing a Plane from Unknown Orientations," *Proceedings of the 7th IEEE International Conference on Computer Vision,* pp. 666-673, 1999.

[79] OpenCV, "OpenCV, Open Source Computer Vision Library," [Online]. Available: http://opencv.willowgarage.com/wiki. [Accessed 2013].

[80] V. C. Prabhakaran and D. Selva, "Orbital Endoscopic Surgery," *Indian Journal of*

Ophthalmology, vol. 56, pp. 5-8, 2008.

[81] A. M. Pham and E. B. Strong, "Endoscopic Management of Facial Fratures," *Current Opinion in Otolaryngology & Head and Neck Surgery,* vol. 14, pp. 234-241, 2006.

[82] J. L. Kasperbauer and L. Hinkley, "Endoscopic Orbital Decompression for Graves' Ophthalmopathy," *American Journal of Rhinology,* vol. 19, pp. 603-606, 2005.

[83] R. B. Kuppersmith, E. Alford, J. R. Patrinely, A. G. Lee, R. B. Parke and J. B. Holds, "Combined Transconjunctival/Intranasal Endoscopic Approach to the Optic Canal in Traumatic Optic Neuropathy," *Laryngoscope,* vol. 107, pp. 311-315, 1997.

[84] R. Shahidi, M. R. Bax, C. R. Maurer, J. A. Johnson, E. P. Wilkinson, B. Wang, J. B. West, M. J. Citardi, K. H. Manwaring and R. Khadem, "Implementation, Calibration, and Accuracy Testing of an Image-Enhanced Endoscopy System," *IEEE Transactions in Medical Imaging,* vol. 21, pp. 1524-1535, 2002.

[85] M. P. DeLisi, L. A. Mawn and R. L. Galloway, "Transorbital Target Localization in the Porcine Model," *Proceedings of the SPIE Medical Imaging,* vol. 8671, 2013.

[86] B. K. P. Horn, "Closed-Form Solution of Absolute Orientation Using Unit Quaternions," *Journal of the Optical Society of America A,* vol. 4, pp. 629-642, 1987.

[87] R. Khadem, M. R. Bax, J. A. Johnson, E. P. Wilkinson and R. Shahidi, "Endoscope Calibration and Accuracy Testing for 3D/2D Image Registration," *Medical Imaging Computing and Computer-Assisted Intervention (MICCAI),* pp. 1361-1392, 2001.

[88] J. Heikkilä and O. Silvén, "A Four-step Camera Calibration Procedure with Implicit Image Correction," *Proceedings of the IEEE Conference on Computer Vision and Pattern Recognition,* pp. 1106-1112, 1997.

[89] C. Wengert, M. Reeff, P. Cattin and G. Szekely, "Fully Automatic Endoscope Calibration for Intraoperative Use," *Bildverarbeitung für die Medizin* , pp. 419-423, 2006.

[90] R. Melo, J. P. Barreto and G. Falcao, "A New Solution for Camera Calibration and Real-Time Image Distortion Correction in Medical Endoscopy - Initial Technical Evaluation," *IEEE Transactions in Biomedical Engineering*, vol. 59, pp. 634-644, 2012.

[91] M. P. DeLisi, L. A. Mawn and R. L. Galloway, "Image-Guided Transorbital Procedures with Endoscopic Video Augmentation (in submission)," *Medical Physics*, 2014.

[92] I. A. Sigal, J. G. Flanagan and C. R. Ethier, "Factors Influencing Optic Nerve Head Biomechanics," *Investigative Ophthalmology & Visual Science*, vol. 46, no. 11, pp. 4189-4199, 2005.

[93] A. J. Bellezza, R. T. Hart and C. F. Burgoyne, "The Optic Nerve Head as a Biomechanical Structure: Initial Finite Element Modeling," *Investigative Ophthalmology & Visual Science*, vol. 41, no. 10, pp. 2991-3000, 2000.

[94] T. A. Gennarelli, L. E. Thibault, R. Tipperman, G. Tomei, R. Sergot, M. Brown, W. L. Maxwell, D. I. Graham, J. H. Adams, A. Irvine, L. M. Gennarelli, A. C. Duhaime, R. Boock and J. Greenberg, "Axonal Injury in the Optic Nerve: A Model Simulating Diffuse Axonal Injury in the Brain," *Journal of Neurosurgery*, vol. 71, pp. 244-253, 1989.

[95] A. C. Bain and D. F. Meaney, "Tissue-Level Thresholds for Axonal Damage in an Experimental Model of Central Nervous System White Matter Injury," *Journal of Biomechanical Engineering*, vol. 122, pp. 615-622, 2000.

[96] E. H. Black, F. A. Nesi, G. J. Gladstone, C. J. Calvano and M. R. Levine, Smith and Nesi's Ophthalmic Plastic and Reconstructive Surgery, Springer, 2012.

[97] M. D. Abramoff, P. J. Magalhaes and S. J. Ram, "Image Processing with ImageJ," *Biophotonics International,* vol. 11, no. 7, pp. 36-42, 2004.

[98] P. A. Yushkevich, J. Piven, H. C. Hazlett, R. G. Smith, S. Ho, J. C. Gee and G. Gerig, "User-Guided 3D Active Contour Segmentation of Anatomical Structures: Significantly Improved Efficiency and Reliability," *Neuroimage,* vol. 31, no. 3, pp. 1116-1128, 2006.

[99] S. Cirovic, R. M. Bhola, D. R. Hose, I. C. Howard, P. V. Lawford, J. E. Marr and M. A. Parsons, "Computer Modelling Study of the Mechanism of Optic Nerve Injury in Blunt Trauma," *British Journal of Ophthalmology,* vol. 90, no. 6, pp. 778-783, 2006.